

Modeling of Energy and Heat Storage Fixed-Bed Reactors Using Discrete-Element Method

by

Yi Ran Lu

A thesis submitted in partial fulfillment of the requirements for the degree of

Master of Science

in

Chemical Engineering

Department of Chemical and Materials Engineering

University of Alberta

© Yi Ran Lu, 2018

Abstract

This work is devoted to the modelling of heat storage device and energy storage reactors based on Fixed bed geometry. The interparticle discrete-element-method model is developed and used in this work. The model accounts for the interparticle heat exchange directly, which is most useful in a fixed bed where heat transfer between particles is significant. The DEM model can be coupled with one-dimensional or two-dimensional fluid flow and reaction or phase change intraparticle models. The model is used to prove two energy storage solution concepts numerically. The first concept is a new type of fixed-bed reactor for steam-methane reforming (SMR). The reactor consists of two sorts of spherical particles: electrically conductive particles and non-conductive catalyst particles. The main feature of this reactor is the application of electric resistance heating using the electrically conductive particles which heat the non-conductive catalyst particles and reacting gas inside the reactor. Steady-state particle temperatures are calculated based on the developed hybrid model with 3D discrete solid heat transfer and 1D fluid heat and momentum transfer. The modes of heat transfers include conduction between particles, forced convection and radiation. The catalyst size is selected to be 0.4 of radii of the conductive particles, based on the maximum radius at octahedral sites of closed packing. Analysis of simulations based on the electrical current and 3D temperature distribution revealed the optimal volume fraction of catalysts is determined to be between 0.27 and 0.30. The second concept is a heat storage device using encapsulated phase change material (PCM). The PCM considered in this work is paraffin with a melting temperature of 28 °C, which stores heat in the capsules as the PCM melts in a hot environment, and releases when the ambient temperature is cooled down. An intraparticle submodel for the heat rate is described in this work during melting and solidification. The equation for the heat transfer coefficient at the solid-liquid interface is found using direct numerical simulation and validated against published experimental data. A new method of increasing heat transfer is proposed that aluminum particles are mixed in with PCM capsules. The aluminum particles reduce overall charging/discharging time of the heat storage device and make the system more responsive. Numerical simulations using the hybrid model shows that the increase in heat transfer is achieved at the expense of volume efficiency. To reduce the charging/discharging time by 10%, the heat capacity per volume is reduced by 20%.

Preface

This thesis is completed under the supervision of Dr. P. Nikrityuk. The basis of the second chapter of the thesis is a paper submitted to Applied Energy (APEN-D-18-02358) before the defense, co-authored with Dr. P. Nikrityuk. The submitted paper is currently under its 1st revision. The author of the thesis is responsible for conducting of the simulations and programming of the scripts. The author's work constitutes approximately 65% of this paper.

*Take the risk of thinking for yourself, much more happiness, truth, beauty, and wisdom will come to you
that way.*

– Christopher Hitchens

Acknowledgements

This research is conducted under the supervision of Dr. Petr Nikrityuk. I would like to thank his brilliant ideas, tireless support and encouragement of creative thinking.

Contents

1	Introduction	1
1.1	Background	1
1.2	Literature Review	2
1.2.1	Steam-Methane Reforming	2
1.2.2	Heat Transfer in Fixed Bed	2
1.2.3	CFD simulation	3
1.2.4	Discrete Element Method	4
1.3	Objective	4
2	Numerical Studies of Electrically heated Steam-Methane Reformer	6
2.1	Introduction	6
2.2	Problem Formulation	7
2.3	Model Formulation	8
2.3.1	Heat Transfer Model	8
2.3.2	Electrical Current	10
2.4	Particle-Resolved Model	11
2.5	Validations	12
2.5.1	DEM Validation	12
2.5.2	Validation of the Heat Transfer Model	12
2.6	Results	13
2.7	Conclusions	15
2.8	FIGURES	15
3	Phase Change inside a Spherical Capsule	34
3.1	Introduction	34
3.2	CFD Numerical Formulation	36
3.2.1	Transport Properties	36
3.2.2	Governing Equations	37
3.2.3	Boundary conditions and Initial condition	38
3.2.4	Computational Methods	39
3.2.5	Results and Discussion	39
3.2.6	Figures	41
3.3	Semi-Empirical Model Formulation	45
3.3.1	Melting	47
3.3.2	Internal convection	48
3.3.3	Solidification	48
3.3.4	Results and Discussion	50
3.3.5	Figures	50
4	Numerical Studies of Fixed-bed Thermal Energy Storage System Using Encapsulated Phase Change Material	54
4.1	Introduction	54
4.2	Numerical Model Formulation	56
4.2.1	Heat Balance for the charging cycle	57
4.2.2	Heat Balance for the discharging cycle	59
4.2.3	Computational Methods	60
4.3	Simulation Setup	62
4.4	Results	63
4.5	Figures	67

5 Conclusion	87
5.1 Future Work	87

List of Tables

2.1	Comparison of shape factors obtained from simple approximation versus numerical simulation	12
2.2	Operating conditions for the CFD validation	13
2.3	Transport properties used in the CFD validation	13
2.4	Results of simulations	14
3.1	Transport properties of liquid paraffin	37
3.2	Numerical setup and validation	39
3.3	Final numerical setup used for full simulation	41
4.1	List of operating parameters using in simulations	56
4.2	Simulation setup for charging and discharging cycles of fixed-bed heat storage unit, Set 1	63
4.3	Simulation setup for charging and discharging cycles of fixed-bed heat storage unit, Set 2	63
4.4	Vacancy sites in closed packing with ratios of sites, radii, and volumes	65

List of Figures

2.1	Principal scheme of the energy to chemicals (E2C) concept.	16
2.2	Principal scheme of conventional SMR-reactor.	17
2.3	Principal scheme of a standard reformer	18
2.4	Principal scheme of a bed (a) and DEM-simulated fixed bed filled with conducting and catalyst particles, 1cm and 0.4cm in diameter respectively	19
2.5	Schemes explaining calculation of T_g along reactor height (a) and electrical current distribution inside the reactor (b).	20
2.6	Flow-chart diagram of computational algorithm used to calculate the temperature distribution in the endothermic fixed bed heated by DC discharge.	21
2.7	Validation of the DEM software used in this work against experimental data [1] for different ratios between tube diameter and particle diameter: a) radial void fraction distribution for $\frac{D}{d_p} = 5.96$; b) generated packing for $\frac{D}{d_p} = 5.96$; c) radial void fraction distribution for $\frac{D}{d_p} = 7.99$; d) generated packing for $\frac{D}{d_p} = 7.99$	22
2.8	Scheme of setup and the numerical grid used for the modeling of electrical field distribution.	23
2.9	Spatial distribution of the nondimensional electric field potential ϕ^* (a), stream lines of the electrical current density (b) and the absolute values of the nondimensional <i>electrical field intensity</i> magnitude $\ E^*\ = \sqrt{\left(\frac{\partial\phi^*}{\partial r^*}\right)^2 + \left(\frac{\partial\phi^*}{\partial z^*}\right)^2}$ (c). Here, the radius of the contact area is $0.05r_p$	24
2.10	Temperature profile of electrically heated particles under convection and radiation.	25
2.11	Change of the temperature difference inside a particle in relation to the electrical current going through the particle. The radius of the contact area r_c plays a governing role in ΔT	26
2.12	Temperature of particles predicted using our model (a), 3-D CFD simulation (b) and (c) wall (gas) temperature	27
2.13	Axial profiles of the gas temperature predicted using our model and CFD based model	28
2.14	Path of the electrical current (colored by the particle temperature) predicted numerically for different values of the volume fraction of catalyst particles: a) $\varepsilon_{cat} = 0.06$; b) $\varepsilon_{cat} = 0.16$; c) $\varepsilon_{cat} = 0.20$; d) $\varepsilon_{cat} = 0.24$; e) $\varepsilon_{cat} = 0.40$;	29
2.15	Particles temperature predicted numerically for different values of the volume fraction of catalyst particles: a) $\varepsilon_{cat} = 0.06$; b) $\varepsilon_{cat} = 0.16$; c) $\varepsilon_{cat} = 0.20$; d) $\varepsilon_{cat} = 0.24$; e) $\varepsilon_{cat} = 0.40$;	30
2.16	Total surface area of catalyst particles which temperature exceeding 950 K calculated for different values of ε_{cat}	31
2.17	Particles temperature predicted numerically for different values of the volume fraction of catalyst particles and gas flow rate: a) $\dot{m} = 10 \cdot \dot{m}_0$, $\varepsilon_{cat} = 0.16$; b) $\dot{m} = 10 \cdot \dot{m}_0$, $\varepsilon_{cat} = 0.24$; c) $\dot{m} = 10 \cdot \dot{m}_0$, $\varepsilon_{cat} = 0.30$; d) $\dot{m} = 100 \cdot \dot{m}_0$, $\varepsilon_{cat} = 0.16$; e) $\dot{m} = 100 \cdot \dot{m}_0$, $\varepsilon_{cat} = 0.24$; f) $\dot{m} = 100 \cdot \dot{m}_0$, $\varepsilon_{cat} = 0.30$. Here $\dot{m}_0 = 0.05$ kg/s.	32
2.18	Axial profile of particles temperature predicted for $\varepsilon_{cat} = 0.3$ and different flow rates: a) $\dot{m}_0 = 0.05$ kg/s; b) $\dot{m} = 10 \cdot \dot{m}_0$; c) $\dot{m} = 100 \cdot \dot{m}_0$	33
3.1	Grid study by the comparison of liquid fraction over time using refined mesh versus experimental results published in [2] [3]	40
3.2	Melting: liquid fraction contour from CFD	42
3.3	Melting: temperature contour from CFD	43
3.4	Melting: stream velocity contour from CFD	44
3.5	Melting: liquid fracton contour from CFD	45
3.6	Solidification: liquid fracton contour from CFD	46
3.7	Principal scheme of a sphere freezing	49
3.8	Comparison of liquid fraction for melting with CFD and Tan's experimental [2] results	51
3.9	Comparison of liquid fraction for solidification with empirical and CFD results	52

3.10	Change of solidification and melting time due to different ΔT at $d=0.1m$ and different d for $\Delta T = 10K$	53
4.1	Heat Storage in Fixed Bed Computation Scheme Flowchart	61
4.2	Matrix distribution for $\varepsilon_{Al} = 0.27$ with nonzero terms shown as dots	62
4.3	3D visualization of PCM with 60% Al particles by average temperature during the charging cycle at (a)0min, (b)1min, (c)2min, (d)5min, (e)10min, (f)15min, (g)20min, (h)30min, (i)40min	68
4.4	3D visualization of PCM with 33% Al particles by average temperature during the charging cycle at (a)0min, (b)1min, (c)2min, (d)5min, (e)10min, (f)15min, (g)20min, (h)30min, (i)40min	69
4.5	3D visualization of PCM without Al particles by average temperature during the charging cycle at (a)0min, (b)1min, (c)2min, (d)5min, (e)10min, (f)15min, (g)20min, (h)30min, (i)40min, (j)50min	70
4.6	3D visualization of PCM with 60% Al particles by average temperature during the discharging cycle at (a)0min, (b)1min, (c)2min, (d)5min, (e)10min, (f)15min, (g)20min, (h)30min, (i)40min, (j)50min	71
4.7	3D visualization of PCM with 33% Al particles by average temperature during the discharging cycle at (a)0min, (b)1min, (c)2min, (d)5min, (e)10min, (f)15min, (g)20min, (h)30min, (i)40min, (j)50min	72
4.8	3D visualization of PCM without Al particles by average temperature during the discharging cycle at (a)0min, (b)1min, (c)2min, (d)5min, (e)10min, (f)15min, (g)20min, (h)30min, (i)40min, (j)50min	73
4.9	Water Temperature Profile for the charging cycle (a)0-10 min, (b)10-40min	74
4.10	Total energy absorption over time during the charging cycle	75
4.11	Average (a) PCM particle and (b) Al particle temperature over time during the charging cycle for equal size of heat storage unit	76
4.12	Average solid volume fraction for equal size of heat storage unit	77
4.13	Latent and sensible heat stored comparison for equal amount of PCM particles and different volume fractions of Al particles	78
4.14	Latent heat stored comparison for equal amount of PCM particles and different volume fractions of Al particles	79
4.15	Time required for latent heat storage to reach saturation	80
4.16	Average solid volume fraction during charge for equal number of PCM and different volume fractions of Al particles	81
4.17	Average PCM particle temperature during charge for equal number of PCM particles and different volume fractions of Al particles	82
4.18	Time required for latent heat storage to reach saturation	83
4.19	Average solid volume fraction during discharge for equal number of PCM and different volume fractions of Al particles	84
4.20	Average PCM particle temperature during discharge for equal number of PCM particles and different volume fractions of Al particles	85
4.21	Average Al particle temperature during (a) charge and (b) discharge for equal number of PCM particles and different volume fractions of Al particles	86

List of Symbols

Chapter 1&2

D	particle diameter	m
Re	Reynolds number	
ΔH_r	enthalpy of reaction	kJ/mol
ρ_g	gas density	kJ/mol
u_z	velocity in the z (axial) direction	m/s
P	pressure	Pa
R_g	specific gas constant	J kg ⁻¹ K ⁻¹
T_g	gas temperature	K
h_{pg}	particle-gas convective heat transfer coefficient	W/m ² K
A_p	particle surface area	m ²
T_p	particle (solid) temperature	K
A_b	bed diameter	m
\dot{V}	volume flowrate	K
\dot{m}	mass flowrate	K
u_s	superficial velocity	m/s
R_{th}	interparticle thermal resistance	K/W
ε_{void}	void fraction	
ε	emissivity	
k	solid thermal conductivity	W/mK
Q_{cond}	conductive heat rate	W
$f(S)$	shape factor	
L	equivalent length	m
r_b	radius of the bed	m
r_p	radius of the particle	m
r_c	inter particle contact radius	m
κ	electrical conductivity	S/m
R_{layer}	estimated layer electrical resistance	ohm
$R_{overall}$	estimated total electrical resistance	ohm
N_p	number of particles in a layer	Ohm
\vec{j}	current density	A/m ²
σ	electrical resistivity	ohm/m
$L_{j,min}$	number of particles in minimum conduction	
ϕ	electrical field potential	V
ε_{cat}	catalyst volume fraction	
I_{tot}	total current	A
U	Overall voltage	V

Chapter 3&4

ρ	density	kg/m ³
ρ_o	density at 20 °C	kg/m ³
c_p	constant pressure specific heat capacity	J/kgK
k_s	solid thermal conductivity of PCM	W/mK
k_l	liquid thermal conductivity of PCM	W/mK
μ	dynamic viscosity	Pa s
α_v	volumetric expansion coefficient	
β, β_T	linear expansion coefficient	
L, L_m^f	latent heat of melting	J
ΔT	temperature difference	K
$T_{solidus}$	solidus temperature	K
$T_{liquidus}$	liquidus temperature	K
g	gravitational acceleration	m/s ²
ϕ_l	liquid fraction	
ϕ_s	solid fraction	
\mathbf{u}	velocity	m/s
Nu	Nusselt number	
K_p	permeability constant	
K_u	phase damping constant	
c_p	specific thermal capacity	J/kg K
Fo	Fourier number	
Ste	Stefan number	
Pr	Prandtl number	
Re	Reynolds number	
Ra	Rayleigh number	
r_p	radius of the particle	m
r_o	outer radius of the melting/solidifying PCM	m
r_i	inner radius of the melting/solidifying PCM	m
T_s	particle surface temperature	K
T_m	melting temperature of the PCM	K
T_w	temperature of the HTF (water)	K
ϕ	void fraction	
ϵ	effectiveness	
ϵ_{pcm}	PCM volume fraction	
ϵ_{Al}	aluminum volume fraction	
ϵ	void fraction	
\vec{E}_{st}	heat storage rate	W
\dot{V}	volumetric flowrate	m ³ /s
r_{pcm}	radius of PCM particle	m
r_{Al}	radius of Al particle	m

Chapter 1

Introduction

1.1 Background

Modern civilizations have depended on the consumption of fossil fuels for energy since the industrial revolution. Fossil fuels have provided cheap and convenient supply to fulfill our energy needs, which stimulated fast growth and development in the last hundreds of years. However, the combustion of fossil fuels has also had significant impact on the climate, resulting in a warming influence that greatly exceeds natural processes. Fossil fuels are also limited in natural reserves. Although advances in recovery technology have improved the quantity of production, more efficient technology to store and use energy sources is constantly required for sustaining the growth of the economy and integrity of the ecosystem.

Fortunately, renewable energy has made huge progresses in recent years in terms of affordability, availability and reliability. The overall maturation of the technology has materialized into spiky growth of renewable energy industries. Renewable energy is produced from energy sources directly from nature such as wind or solar. Therefore it has more unpredictability than conventional sources. Production does not start and stop easily at the operation's command. A power plant is usually used to compensate the mismatch between supply and demand in a grid system where renewable energy only makes up a small proportion. However, when renewable energy accounts for the majority of energy produced, the adjustment in a traditional power plant is no longer sufficient. When renewable energy exceeds the entire consumption, excess energy is not only wasted, but also demanding proper release. In fact, an oversupply of power from wind and solar can potentially damage the grid. In Germany, the supply-based pricing once pushed the net price of electricity into the negatives to encourage usage during off-peak hours.

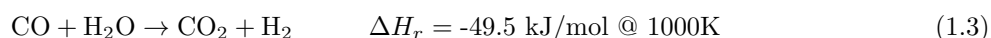
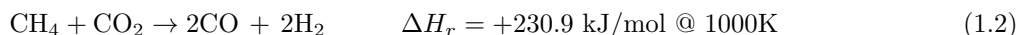
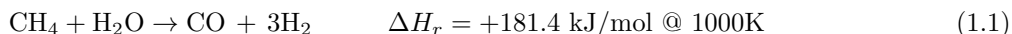
The particle bed is used for transport between solid and fluid phases. Since the momentum transport does not occur between solid particle and gas in a fixed bed, heat and mass transport are two phenomena important to the study of fixed beds. The main advantages of fixed bed system are its simplicity and low cost. Fixed bed has a wide range of applications. Fixed beds can be used as catalytic reactors where the fluid is adsorbed onto the surface of the particles to undergo chemical reaction. Fixed beds can also be used for physical processes such as separation and heat storage. Mass transport is the rate limiting factor for separation, where the adsorption separate a species from the feed fluid. With mass transport, there is always energy transport that changes the temperature of the fixed bed. Adsorption is always an exothermic process, which raises the temperature of the fixed bed. The adsorption capacity and rate are affected by the temperature of the solid particles [4]. The released heat must be adequately managed to maintain the efficiency of adsorption and desorption. Chemical reactions can be exothermic or endothermic with often greater heat supply or removal demands than the physical processes. Therefore whether the purpose of the process is mass separation, heat storage or catalysis, the heat transfer is always a phenomenon that needs to be understood. The study of heat transfer enables new designs and innovative solutions to the existing problems.

1.2 Literature Review

1.2.1 Steam-Methane Reforming

Steam-methane reforming (SMR) is the production of H₂ and CO using steam and methane in natural gas. The discovery of reforming came in 1780, before natural gas was when Felice Fontana passed water vapor over heated coal to produce a combustible gas. In the 19th century, the gasified coal gradually became widely used for lighting purposes. SMR became prevalent with large use of natural gas instead of coal gas. Because the product gas was a mixture of H₂, CO and CO₂, which is widely used in the 20th century and today for petroleum synthesis, it gained the name syngas.

Steam-methane reforming is a very endothermic process. There are three main reversible reactions occurring in the SMR reactor shown in Eqn. 1.1-1.3



The main disadvantage of steam-methane reforming is its high process temperature, which happens typically at 650-1000 °C. Conventionally, the exit stream gas temperature is typically over 800 °C. One of the reasons to have high gas temperature is to maintain high conversion rate at chemical equilibrium. Because the reactions are reversible, the equilibrium will shift backwards if the gas temperature is reduced in the catalytic region. For hydrogen to be used in fuel cell and chemical processing, the hydrogen needs to be purified through amine scrubbing or pressure swing adsorption [5]. The removal of hydrocarbon is a more difficult process than CO₂. Therefore high conversion rate is highly influential to the effectiveness of subsequent separation processes [6]. The other reason is because heat is supplied to reactor through the walls. The gas must have higher temperature than the catalyst particles to supply the heat of reaction in the endothermic reactions. Finding a way to lower the temperature of the process has financial and ecological advantages.

One of the problems with low reaction temperature is that coking occurs on the surface of the catalysts, reducing the catalytic effectiveness. Angeli et al. [7] discovered that for low temperature reactions, ethane and propane, which naturally occur in natural gas, are responsible for most of the carbon deposition on the catalysts. Methane can be prepared from natural gas by passing through a layer of active carbon [8]. Halabi et al. [9] found that the interface between active metal and support material, as methane is adsorbed by the active metal and steam is adsorbed by the support, and the surface reaction at the interface is the rate determining step of steam-methane reaction. Hufton et al. [10] proposed the concept of using in-situ removal of CO₂ by sorption to shift equilibrium and improve the purity of hydrogen. The sorption method used solid particles to adsorb CO₂. The capture of CO₂ resulted in more H₂ production from water-gas shift in Eqn. 1.3 at lower temperature. The concept mixed catalyst particles and sorbent particles in a fixed bed. S.Z.Abbas et al. [11] modelled the sorption-enhanced SMR using a 1-D heterogeneous mathematical model, and estimated that H₂ was up to 85%. However, the conversion rate of CH₄ was found to be only 65% due to the reduced temperature, making it unsuitable for high-purity hydrogen production.

1.2.2 Heat Transfer in Fixed Bed

Despite the prevalent use of fixed beds in various industrial processes, the heat transfer in fixed bed is still unclear in many areas. Until recently, the most popular approach to model a fixed bed reactor is to treat the fixed bed as a homogenous porous media [12, 13]. Classic researches either use effective thermal conductivity or heat transfer coefficients to represent heat transfer, which have not been able to provide consistency with experimental data. There are three major modes of heat transfer in a fixed bed:

1. Intraparticle heat transfer,
2. Interparticle heat transfer,
3. Particle-gas heat transfer.

The intraparticle heat transfer is fully conductive. Most of the heat of reaction is released or absorbed from the outside source to the surface of the catalysts. Therefore the intraparticle conduction is insignificant. For heat storage in fixed beds, the intraparticle heat transfer is an important part. Interparticle heat transfer is mainly conduction, but surface to surface radiation also plays a role in high temperature processes [14]. Researchers found that the thermal resistance between particles are not only dependent on macroscopic conductive resistance, but also microscopic constrictive contact resistance which is affected surface roughness and surface chemistry [15, 16, 17]. Fluid flow is also shown to affect the interparticle thermal resistance [18]. Particle-gas heat transfer generally involves convection, but also radiation at high temperatures.

The modeling of fixed bed reactors depends on the nature of the industrial process. In high-temperature, energy-intensive industrial processes, heat is almost always transfer to the fixed bed indirectly, i.e. through a wall by radiation and conduction [19]. Due to the strong endothermic character of SMR and the high temperature of reaction, reaction heat needs to be supplied effectively to the surface of the catalysts mostly by radiation. the reactors are designed with small tube-to-particle diameter so that heat is effectively transferred. In pyrolysis or gasification, a direct heat transfer is used by burning fuel in the reaction chamber. For steam-methane reforming, combustion changes chemistry in the reactor and contaminate the product. Martinez et al. [20] identified the estimation of overall overall heat transfer coefficient by relating the one-dimensional homogeneous model to the two-dimensional heterogeneous model. The heterogeneous one-dimensional model, which incorporates radial heat transfer through the solid phase, calculates one-dimensional coefficients, which best represents a system without axial dispersion. In industrial reactors, axial dispersion is considered unimportant in most cases. Therefore the model was used for heat transfer in reactors [21, 22] with reasonable success.

1.2.3 CFD simulation

One of the difficulties is to obtain a complete temperature profile in the fixed bed. Kutsovsky et al. [23] along with other scholars, used magnetic resonance imaging to map out the velocity profile of a fixed bed, but the temperature data remained scarce, available only at probe locations. In recent years, the development of CFD has allowed detailed direct numerical simulation of the temperature and flow velocity distribution. especially in cases with small tube-to-particle diameter ratios [24]. The near-wall regions have higher porosity, which causes flow to be faster. The Bernoulli effect of the difference in axial velocity causes outwards radial velocity. Both momentum and heat transfer in the near wall region are significantly different from the bulk of the fixed bed. Therefore the empirical equations have very limited usability for reactors with the low tube-to-particle diameter ratios. There have been many efforts to understand the heat transfer in fixed beds using CFD numerical simulation. The early study of fixed bed using idealized structured packing. Direct numerical simulation is very useful to find temperature of hot spots in a fixed bed, which has profound influence on the behavior of reactors [25]. Logtenberg et al. [26, 27, 28] found that the contact points between particle and particle and between particle and wall have high heat transfer coefficient due to high flow around these points. Dixon et al. [29] used resolved intraparticle models to simulate steam reforming, and found while non-wall particles have symmetrical temperature and species profile as conventionally assumed, the near-wall particles behave very differently due to wall conduction and flow pattern. Taskin et al. [30] conducted CFD study of fluid flow and heat transfer in a fixed bed filled with cylinders, and found that non-spherical shaper exacerbated the temperature gradient for near-wall particles. Dixon et al. [31, 32] went on to investigate particles of different shapes and concluded boundary layer fineness is the key to accurate CFD and simulation of single particle is useful for mesh development for heat transfer in CFD. Behnam et al. [33] studied the SMR using CFD with discrete particle beds and obtained realistic results comparable to experimental data. Mansoori et al. [34] showed interparticle heat transfer is significant, but does not affect particle-gas heat transfer. CFD simulation is computationally expensive, because it resolves details of the boundary layer around a particle. Resolved particle models have rarely been used, since the additional mesh inside the solid particles often increase the cost of largely. Recently, Dixon [35] used resolved particle models with CFD to simulate a fully-scale SMR inside a fixed bed. Diffusion and reaction inside particle show that two-dimensional model with radial void fraction gives temperature profile similar to CFD results. The importance of intraparticle changes necessitates 1D diffusion model. One-dimensional model was found

to be less accurate because the large void fraction variation in the fixed bed with a small tube-to-diameter ratio. The channeling effect is also documented in other papers [36, 37]. Away from the near-wall region, 1D model can be sufficient as far as heat transfer is concerned.

1.2.4 Discrete Element Method

Discrete Element Method (DEM) is a simulation method used to model particles as discrete elements. Because of the movement of particles, DEM is able to have interactions between any of the elements. The simplification of a particle as one element enables the simulations of thousands of particles and their collective behaviour. There are two types of particle interaction frameworks, the soft-sphere and hard-sphere framework. The hard-sphere particles have instantaneous collisions whereas the soft-sphere particles have collision time. Hard-sphere model is advantageous when the system is not packed with particles in contact with each other. Soft-sphere model is more useful when the multi-particle contacts dominate the interactions. Allowing particles to overlap stabilizes the momentum balance in a packed system. Zhu et al. [38, 39] described the different theories and application of models extensively. DEM models are useful for generating random packing that retain the characteristics of real fixed beds. The technique of DEM is a recent development. Earlier works were only used to generate spherical particles. Theuerkauf et al. [40] generated random fixed bed of spherical particles using DEM. DEM was shown to have average void fraction in agreement with experimental values. Because of the simplicity of spherical particles, glued spheres were used to represent different shapes of the particles. Caulkin et al. [41] found that particle roundness has a great impact on packing structure. The edges of the shape need fine resolution to obtain acceptable accuracy. Caulkin concluded the minimum number of glued spheres used to represent the cylinder should be 79. True-shape DEM simulation used by Tangri et al. [42] also showed good agreement with experimental data, and realistic predictions packing density. True-shape particles have the ability to model rolling friction which gives different predictions than glued-sphere shapes despite the increased number of spheres.

1.3 Objective

The main objective of this work is to study novel energy storage concepts by simulation. Namely, the E2C concept of SMR fixed-bed reactor heated by DC discharge, and the heat storage concept where phase-change material (PCM) encapsulated in spherical shell is used in a fixed bed. For the E2C concept, the fixed bed reactor consists of the conductive metal particles and the non-conductive ceramic particles. Joule heating effect of metal particles in the fixed bed is expected to provide the heat of reaction. Since heat is supplied internally at the particle, the heat transfer distance is much shorter. Current distribution in the fixed bed should be evenly distributed, resulting in relatively uniform heating in the bed. There should not exist a radial temperature gradient in the fixed bed. The study is aimed to improve energy efficiency of the SMR process and lower overall energy consumption. The tube wall can be insulated since heat is no longer supplied by heating the wall. Because the fixed bed has a uniform radial temperature profile, the fixed bed can have large tube-to-particle diameter ratio. Fixed beds with large diameters also have good volume-to-area ratio, which improves thermal insulation. The particles have higher temperature than gas due to Joule heating. The direction of heat transfer is reversed in the electrically heated SMR. Heat is transported to the catalytic sites much more quickly because of the higher conductivity of solid than gas. Since the catalytic sites are maintained at higher temperature than gas, it prevents the equilibrium from shifting backwards. The solid phase heat generation should see an increase in conversion rate and a decrease in gas temperature in the exit stream. Moreover, the application of the E2C concept is expected to be especially compatible with increasing capacity of renewable energy sources. If it can take advantage of the cheap, excess supply of renewable energy during off-peak hours, it offers a feasible solution that can truly rival the conventional industrial gas-fired SMR process. The simulation of electrical heating in fixed bed. The electrical heating through spherical particles is not uniform. Direct numerical simulation was used to find the current and temperature distribution inside a single conductive particle. CFD-based simulation was used to validate the heat transfer correlation that will be used to find heat transfer coefficient. Finally, DEM simulation heating of fixed bed was done using a three-dimensional interparticle model coupled with one-dimensional

gas-particle heat transfer. The heat storage concept was studied using the same DEM model except with an intraparticle submodel. The intraparticle submodel was developed based on classic empirical or analytical equations to compute the heat transfer inside a capsule during melting and solidification. The submodel is derived based on data using CFD simulation. The CFD simulation was validated using experimental results in published literature. In addition to encapsulated PCM, the fixed bed also contains aluminum particles in an attempt to improve heat transfer and reduce response time. The numerical studies aim to investigate the influence of aluminum particle volume fraction, capsule size, fluid flow rate and temperature on the performance of the heat storage system.

Chapter 2

Numerical Studies of Electrically heated Steam-Methane Reformer

2.1 Introduction

1

The increase of renewable energy in energy production presents the challenging mismatch between the energy demand and supply renewable sources. It is necessary to store the energy during production peaks. One promising energy storage technology is the direct conversion of electrical current into chemical energy, which is called '*electricity to chemicals*' (E2C). A famous example of conversion is the electrolysis of water to produce hydrogen, where a direct electric current (DC) is used to drive the non-spontaneous chemical reaction. Alternatively, DC can be used to heat any electrically conductive material (using the Joule heating effect) to provide the heat needed for endothermic chemical reactions. Using such technology, reformers or gasifiers heated by electric currents overproduced during production peaks can be adopted to address energy storage needs. In this chapter, a new type of energy storage fixed bed reactor is proposed. A principal scheme of this concept is shown in Fig. 2.1. An option to store electrical energy into chemicals is to use the so-called steam methane reforming (SMR), which uses endothermic reactions to convert CH_4 and CO_2 plus H_2O into a syngas comprising of CO and H_2 .

Steam-methane reformers have been commonly used to produce hydrogen and other fuels [30, 43] on an industrial scale. Reforming is the process that converts a fossil fuel of greater abundance and lower cost to a fuel or chemical that is more useful. Steam-methane reforming is a highly endothermic process. Conventional reactors use an array of radiant tubes filled with catalysts and heat is supplied by the gas fire in the chamber outside the tubes. A principal scheme of a classical SMR is shown in Fig. 2.2. Reforming takes place in the radiant tubes. Heat is supplied from the outside wall tube to gas and catalyst, which results in an uneven radial temperature profile [44, 45, 46]. From Fig. 2.2 it can be seen that the nonhomogeneous distribution of temperature causes uneven reaction rate. To a good temperature at the centre of the tube, the temperature of the radiant tube often far exceeds the reaction temperature, which results in a compromised thermal efficiency of energy conversion [47] and up-scaling is a difficult task. An alternative concept was introduced by Glaser and Thodos [48], who used the Joule heating effect to heat electrically conducting spherical particles inside the cylinder. In particular, Glaser and Thodos [48] established studies of heat and momentum by measuring the temperature and pressure of gas flow through a fixed bed consisting of randomly packed metallic particles. Experiments have been conducted passing direct electrical current through the fixed bed consisting metal spheres to provide heat, which is continuously removed by the gas flow. Joule heating proved to be effective when the fixed bed consists of conductive metal particles. Therefore, the concept of electrically heated fixed-bed reactors for SMR is not a new one. However, to increase the conversion of this concept we suggest to use catalysts particles mixed with electrically conductive particles,

¹Chapter 2 is based on the manuscript *A Fixed Bed Reactor for Energy Storage into Chemicals (E2C): Proof of Concept* by Y. R. Lu, P. Nikrityuk submitted to Applied Energy J.

see Fig. 2.3. The electrically conductive particles will have internal heating and heat the nearby catalyst particles through conduction and radiation. To avoid current leakage, the wall for the fixed bed is made of a high-temperature ceramic for electric and thermal insulation.

The main objective of this chapter is to develop an interparticle model of the fixed bed reactor consisting in different sorts of particles: electrically conductive particles, which are used as heaters, and electrically non-conductive metal-on-ceramic particles a high surface area for catalysis. The model encompasses particle-particle heat transfer (conduction and radiation), particle-gas heat transfer (convection and radiation), and 1D fluid flow. The model developed and validated is used to study steady-state electric heating of gas in a fixed bed reactor. In particular, the main issue to be studied is the appropriate particle size and a volume fraction of catalysts which does not block the electrical current going through electrically conducting particles. In theory, larger catalyst particles provide good thermal conduction and a stable gas flow [49]. However, they have small area-to-volume ratios and likely to block the electrical current. On the other hand, smaller catalyst particles fit easily between conductors. A smaller size is also beneficial because it provides more surface area per volume. The optimal design will be determined by varying the particle size and volume fraction through simulation.

2.2 Problem Formulation

When used in a standard fixed bed heated by DC discharge, see Fig. 2.3a, a catalyst in the form of spherical particles must be both electrically conductive and able to catalyse endothermic chemical reactions. For example, nickel is a conductive and catalytic material, but mono-disperse *solid metallic* spheres do not provide enough surface area for catalysis. To improve the catalytic sites, small porous catalytic particles are added between large conductive particles to enhance the conversion rate, see Fig. 2.3b. The catalyst particles are heated by the conduction and direct radiation coming from electrically conducting particles heated by Joule heating. Such heating will keep catalysts particles at a higher temperature than the bulk gas. Because the electric current is well spread through many particles, the electrical heating maintains a homogeneous distribution of the temperature inside the reactor. This effect makes the design in Fig. 2.3b more favourable in comparison to a wall-heated SMR reactor characterized by a strong radial temperature gradient, e.g. see the work [35].

However, it should be noted when designing a Joule-heated reactor, the difficulty is the prediction of total electrical power needed to heat the bed using electric current passing through electrically conductive particles. The second main issue with using electrically non-conductive catalyst particles is that an excessive amount of catalyst particles will block the electrical current paths through conductive particles. *The main question to be answered is what the maximum volume fraction of catalyst can be used to guarantee that the current discharge spreads evenly through the bed.*

To study the influence of small catalyst particle on the heat transfer inside a bed heated by DC discharge, we consider a cylindrical reactor filled with electrically conducting particles (*"heaters"*) and catalyst particles (*"reactors"*), see Fig. 2.4a. A cold gas is supplied from the bottom of the reactor. Between the bottom and the top of reactor we apply electric field potential difference. Fig. 2.4b shows a packed bed of particles created using open-source software Yade [50], see section 2.5.1 for details. Two types of particles are generated in an interlaying pattern, dropped from height and allow to settle under gravity in a cylinder. The cylinder has a height of 50 cm and a cross-sectional diameter of 10 cm. Larger metal particles act as heat source from Joule heating effect while smaller porous catalyst particles can be used to catalyse endothermic reactions. While the conductive particles have radii of 0.5cm, the respective catalyst particles have radii of 0.2 cm, 0.3 cm, 0.4 cm, 0.5 cm. The other input variable is the ratio of numbers of conductor and catalyst particles. The maximum number of conducting and catalyst particles used in this work was set to $3 \cdot 10^4$.

The electrical resistance of the fixed bed can be considered as two parts: the contact resistance and bulk resistance [51]. Unlike the predictable bulk resistance, the electrical contact resistance is more complicated to determine [52]. The primary contribution to contact resistance is from the constriction of current through spot contacts [53]. However, because the contact resistance is much higher than the bulk resistance, it is also subject to a much higher Joule heating effect. The contact spots between two particles will fuse [54]

and disappear, creating a so-called 'bridging effect between two particles which increases contact area and reduces resistance. Therefore the surface roughness can be neglected and the particle contact area can be seen as a circle at a fraction of the particle radius.

2.3 Model Formulation

2.3.1 Heat Transfer Model

In this work we utilize the so-called Euler-Lagrange based model to simulate the heat transfer in a packing due to the Joule heating effect generated by DC discharge. Our model uses 1D formulation of basic conservation equations for the gas phase and 0D formulation of heat balance equations written in Lagrangian space for each particle in a packed-bed. Due to this fact, we predict 3D distribution of the solid phase temperature inside the fixed-bed. In comparison to CFD-based particle-resolved simulations, e.g. see recent review by Jurtz et al. [43], our model is computationally cheaper. However, due to 1D character of our gas-phase equations, our model can produce some inaccuracy for fixed beds with low values of tube-to-particle diameter ratios heated from the wall. This limitation is caused by neglect of wall channelling effect.

Before we proceed with the mathematical formulation of a model several assumptions are introduced:

1. the system is at a steady state
2. the catalyst particle porosity is not taken into account
3. gas flow is treated as an incompressible ideal gas
4. the properties of materials, including their electrical conductivity, thermal conductivity, specific heat capacity and the density are assumed to be constants
5. the particles have a homogeneous temperature, which is valid for $Bi < 0.1$
6. buoyancy effects are neglected
7. the reactor walls are insulated
8. the ratio between the reactor diameter and particle diameter is larger than 10, thus the influence of wall channelling on the flow hydrodynamics is neglected [49].

Taking into account these assumptions, the complete set of governing equations for heat transfer take the following form:

$$\frac{d}{dz} (\rho_g \dot{V}) = 0; \quad \rho_g = \frac{P}{R_g T_g} \quad (2.1)$$

This equation is used to calculate the flowrate along the reactor height.

$$\dot{V} = u_s \cdot A_b \quad (2.2)$$

The superficial flow velocity is found using the above equation and used to calculate Reynolds number of the system. The gas temperature increases along the z -direction due to heating from particles. Since the heat input and output of a system are always equal at steady state, the gas temperature can be discretised as a 1-D variable, and obtained using the total convective and radiative heat transfer rate in each layer, see Fig. 2.5. The heat balance for each layer of gas takes the following form:

$$\underbrace{\sum_{j=1}^{N_\Sigma} \left[h_{pg} A_{p_j} (T_{p_j} - T_g^{n+1}) + \varepsilon \sigma A_{p_j} ((T_{p,j})^4 - (T_g^{n+1})^4) \right]}_{\text{convection and radiation between gas and particles}} - (T_g^{n+1} - T_g^n) \cdot c_p \rho_g \dot{V} = 0 \quad (2.3)$$

where N_Σ is the number of all particles (electrically conducting and catalyst) in the layer between n and $n + 1$, see Fig. 2.5, $h_{pg} = \frac{Nu k_g}{d_p}$ is the convective heat transfer coefficient between gas and particles. The convective heat transfer of gas in the fixed bed is solved based on Gunn relation [55], the equations for calculating the Reynolds number and Nusselt number are as follows:

$$Nu = (7 - 10\varepsilon_{void} + 5\varepsilon_{void}^2) \left(1 + 0.7Re^{0.2}Pr^{1/3}\right) + (1.33 - 2.4\varepsilon_{void} + 1.2\varepsilon_{void}^2) \cdot Re^{0.2}Pr^{1/3} \quad (2.4)$$

The heat balance for an electrically conducting particle participating in DC discharge current takes the form:

$$\frac{\sum_{i=1}^n (T_{p,c} - T_{nbi})}{R_{th}} + h_{pg} \cdot A_p^c (T_{p,c} - T_g) + \varepsilon\sigma A_p^c (T_{p,c}^4 - T_g^4) - \dot{E}_g = 0 \quad (2.5)$$

where the term \dot{E}_g characterizes the Joule heating effect. This term is calculated using Eq. (2.17). n is the number of neighbours for the particle i .

The heat balance for a catalyst particle and an electrically conducting particle not participating in DC discharge takes the form:

$$\frac{\sum_{i=1}^n (T_{p,nc} - T_{nbi})}{R_{th}} + h_{pg} \cdot A_p^{nc} (T_{p,nc} - T_g) + \varepsilon\sigma A_p^{nc} (T_{p,nc}^4 - T_g^4) = 0 \quad (2.6)$$

where n is the number of neighbours for the particle i , superscript nc denotes electrically non-conducting particles. First term on the left-hand side of Eqs. (2.5) and (2.6) describe heat conduction between neighbour particles. Thermal conduction depends on the thermal resistance and thermal potential.

$$Q_{cond} = \frac{\sum_{i=1}^n (T_p - T_{nbi})}{R_{th}} \quad (2.7)$$

T_{nb} is the temperature of neighbour particles.

The line connecting the centres of the particles is the direction of overall heat transfer. Although the overall heat transfer is one-dimensional, the local heat transfer is not. Therefore the thermal resistance R_{th} cannot be obtained analytically. Instead the thermal resistance is found using empirical approximations. The heat rate is calculated based on Fourier's law:

$$q = -kA \frac{\Delta T}{L} = -\frac{\Delta T}{R_{th}} \quad (2.8)$$

Thermal resistance can be expressed as

$$R_{th} = \frac{L}{kA} \quad (2.9)$$

It is clear that $A \propto r_p^2$ and $L \propto r_p$ because of similarity. Therefore we can conclude $R_{th} \propto 1/r_p$. We express the thermal resistance using a non-dimensional shape factor $f(S)$.

$$R_{th} = \frac{f(S)}{r_p k} \quad (2.10)$$

The shape factor is determined by the size of the contact area between two spheres. The contact radius is nondimensionalized by dividing by the particle radius. Because contact radius between particles is much smaller than the particle radius, most of the thermal resistance lies near the contact surface between two particles. Therefore a simple approximate form of overall radius is proposed, equal to the thermal resistance of a cylinder with cross-section are identical to the contact surface and length equal to the diameter of the contact surface.

$$f(S) = \left(\frac{\pi r_c}{2r_p}\right)^{-1} \quad (2.11)$$

Heat conduction is analogous to electric conduction. Thus the shape factor can be obtained by measure the electric resistance and conductivity of the particles in identical setup. The values from the simple approximations are validated with numerical simulations using ANSYS-Fluent [56] in the following section.

Once the thermal resistance is obtained, we can apply it to the discrete element heat transfer model. The heat generation due to electrical current is added to Eq. 2.5.

To solve Eq. 2.5 for each particle, we must define whether the particle participates in current discharge, so to calculate the electrical current going through each particle. Since we assume that the conducting particles are identical in size and material, the resistance should be the same for all conducting particles. The resistance of one particle can be expressed in conductivity and shape factor. The shape factor here is analogous to that in Eq. 2.11:

$$R_p = \frac{f(S)}{\kappa} \quad (2.12)$$

The particles experiencing Joule heating are those connected to the circuit. Therefore if a conductor is not connected to both the top and bottom plates through other conducting particles, it will not be heated. Therefore, to calculate current pathways in a fixed bed, a MatLab script is written. First, conducting particles are identified on the bottom plate. The neighbouring particles to the bottom particles are found. Then the next group of neighbouring particles is found so on. The same process is carried out for the particles in contact with the top plate. If a particle is found to be connected to both the top and the bottom plate through a contacting neighbour, it is determined to have current flowing through it. Fig. 2.6 is a flow-chart diagram of the computational algorithm used to calculate the temperature distribution in the endothermic fixed bed heated by DC discharge.

2.3.2 Electrical Current

The amount of current flowing through each particle is estimated by dividing the fixed bed into layers, see Fig. 2.5b. Each layer is considered as a resistor and all layers are connected in series. The height of one layer is equal to the height of a layer of particles in random packing. Within each layer, there are N_p of particles which are connected in parallel, and the overall resistance is

$$R_{layer} = R_{th}/N_p \quad (2.13)$$

and the overall resistance of the fixed bed is

$$R_{overall} = \sum R_{layer} \quad (2.14)$$

The overall current is conserved through each layer of particles. Thus the current can be calculated using Ohm's law

$$I = \frac{U}{R_{overall}} \quad (2.15)$$

The current through one layer is spread uniformly among all particles since all particles are in parallel and have the same resistance

$$I_p = I/N_p \quad (2.16)$$

Therefore the heat generation for each particle is equal to.

$$\dot{E}_g = I_p^2 \cdot R_{th} = \frac{I^2 \cdot R_{th}}{N_p^2} \quad (2.17)$$

Finally, the algorithm to calculate electrical current distribution inside the bed takes the following form:

1. define the shortest \vec{j} pathway $L_{j,min}$,
2. split reactor into horizontal discs, where the height of each disc is $\delta = \frac{H}{L_{j,min}}$,
3. count the number of electrically conducting particles in each disc (N_p) and define the number of contacts with electrically conducting particles from above using a 90 degree angle,

4. calculate the resistance of a disc $\frac{N_p \cdot R_{single}}{N_{connectors}}$, where R_{single} is the resistance between two particles. Values of R_{single} are calculated using the particle-resolved model,
5. calculate overall resistance R_{Σ} ,
6. using the total energy $\sum E$ as an input parameter, calculate $I = \sqrt{\frac{E}{R_{sum}}}$ and $U = I \cdot R_{sum}$.

2.4 Particle-Resolved Model

Next, to evaluate the electrical resistance term used in Eq. 2.17 between conducting particles and conductive heat transfer term in Eq. 2.7 we consider a row of three spherical particles, where an electrical potential difference, $\Delta\phi$, is applied between first and last particles. Fig. 2.8a shows the scheme in flowchart of the computational domain. To unify the analysis of results we use nondimensional variables:

$$r^* = \frac{2r}{d_p}, \quad z^* = \frac{2z}{d_p}, \quad \phi^* = \frac{\phi}{\Delta\phi} \quad (2.18)$$

where $\Delta\phi$ is the electrical potential difference applied between particles, d_p is the diameter of a particle.

The resolved Energy conservation in a particle takes the following form:

$$\nabla \cdot (\rho \vec{u} h) = \nabla \cdot (\lambda \nabla T) + \underbrace{\vec{j} \cdot \vec{E}}_{\text{Joule heat}} \quad (2.19)$$

The electrical current density inside the particles can be calculated using Ohm's equation and the charge conservation equation, respectively:

$$\vec{j} = \sigma \vec{E} \quad (2.20)$$

$$\nabla \cdot \vec{j} = 0 \implies \nabla \cdot (\sigma \nabla \phi) = 0 \quad (2.21)$$

where $\vec{E} = -\nabla\phi$ is the electric field intensity.

Assuming that electrical conductivity of particles is constant and using nondimensional variables Eq. (2.21) can be rewritten as follows:

$$\nabla^2 \phi^* = 0 \quad (2.22)$$

Eq. 2.22 is solved numerically using the MHD model available in the commercial software ANSYS-Fluent [56]. Figs. 2.8b and 2.8c show the numerical grid (including its zoomed view) used in the calculations. The radius of the contact area was set to $0.1r_p$. The numerical grids used in the simulations had different number of control volumes depending on the contact area $\frac{r_c}{r_p}$. The finest grid of $0.5 \cdot 10^6$ CVs was used for $\frac{r_c}{r_p} = 0.01$. Grid studies were carried out showing that all grids resolutions were sufficient to obtain grid-independent results.

The results of the simulations are shown in Fig. 2.9, which depicts the spatial distribution of the nondimensional electric field potential ϕ^* , the stream lines of the electrical current density and the absolute values of the nondimensional *electrical field intensity* $\|E^*\| = \sqrt{\left(\frac{\partial\phi^*}{\partial r^*}\right)^2 + \left(\frac{\partial\phi^*}{\partial z^*}\right)^2}$. It can be seen that the electrical current density reaches its maximum at the contact area between two particles, thus the Joule heating term $\frac{\vec{j} \cdot \vec{E}}{\sigma} = \sigma \vec{E}^2 = \sigma \left(\left(\frac{\partial\phi^*}{\partial r^*}\right)^2 + \left(\frac{\partial\phi^*}{\partial z^*}\right)^2 \right) \left(\frac{\Delta\phi}{0.5d_p}\right)^2$ reaches the maximum at the contact area between particles.

To illustrate the influence of the Joule heating on the temperature distribution inside particles, Fig. 2.10 depicts shows temperature contour plots for 3 particles under 0.2 V electric potential. The following input parameters were used: ambient gas temperature 300 K, convective heat transfer coefficient $h=43 \text{ W}^2/\text{m}^2 \text{ K}$ corresponding to $Re = 1000$, surface emissivity 0.9, contact area of $r_c/r_p = 0.01$. From 2.10 it can be seen that the hottest point is the area contact between two particles, due to the high current density, and the coldest point is the side surface, due to convection. The electrical conductivity of nickel is $\kappa = 3.47 \times 10^{-6} \text{ S/m}$.

The area between particles depends on the normal force between particles. Hertz model contact mechanics are used to calculate the contact area. It was shown that the contact radius is about 0.5% to 1% of the particle radius in a gravity-compacted fixed bed. Considering the sintering effects of electric current, we can safely say that a 1% particle radius is a valid assumption. The temperature difference between the hottest point (particle bridge) and the coldest point (side) predicted for different contact surface areas and electrical field potentials is shown in Fig. 2.11. In Fig. 2.11, it is shown that the temperature range varies linearly with current on a log-log scale plot. The temperature range is also dependent on the contact area.

Finally, to evaluate the particle resistance and nondimensional shape factors, Table 2.1 summarizes results of simulations for different contact areas, since the resistance is concentrated at the contact area between particles. It can be seen that there is a consistent overestimation from the simple approximations. However, if a power of -0.95 is used instead of -1 , the error is significantly reduced.

r_c/r_p	Num. grid	f(S),MHD	$f(S),\left(\frac{\pi r_c}{2r_p}\right)^{-1}$	% error	$f(S),\left(\frac{\pi r_c}{2r_p}\right)^{-0.95}$	% error
0.01	1406864	51.82	63.66	+22.27	50.57	-2.42
0.05	89376	10.87	12.73	+17.11	10.96	+0.84
0.1	70828	5.733	6.366	+11.04	5.674	-1.03
0.2	57398	3.019	3.183	+5.43	2.985	-1.14

Table 2.1: Comparison of shape factors obtained from simple approximation versus numerical simulation

2.5 Validations

2.5.1 DEM Validation

In this work, fixed-bed structures were generated using the DEM software YADE [50, 57]. Yade is an open-source 3-D simulation software that serves as a framework to provide a stable and uniform environment for scientists to implement computational algorithms for the discrete element method (DEM). YADE runs under OS Linux. Time is integrated using a leapfrog time-integration scheme [50]. To track particles, Newton’s second law of motion is used to compute the dynamics of particles. YADE uses the soft-body model, which allows rigid particle surfaces to penetrate each other during collision. The particles are assumed to be rigid bodies, but interparticle deformation is allowed by overlapping between particles using a simple force displacement law [57]. The period and distance of overlapping are controlled by the collision time constant. The collision time must be at least an order of magnitude larger than the timestep to produce viable results.

To validate the DEM software, we calculate the void fraction distribution in a cylindrical packed bed with a bed height of $7.84d_p$ and different diameter ratios in line with experiments conducted by Mueller [1]. Mueller measured the radial void fraction distributions in randomly packed fixed beds of uniformly sized spheres in cylindrical containers with different tube-to-particle diameter ratios. This experiment is widely used to validate of DEM software, e.g. see [43, 58]. Fig. 2.7 shows generated packing with diameter ratios of $5.96d_p$ and $7.99d_p$ and corresponding radial void fraction profiles predicted numerically and measured in experiments [1]. It can be seen that the radial void fraction profiles of numerically generated packing agrees well with experimental data.

2.5.2 Validation of the Heat Transfer Model

To validate our heat transfer model, we carry out 3D CFD simulations based on setup used in the work [59]. The only difference is we use a cylinder with thermally isolated sidewalls. A CFD case consisting of 374 conductive particles made of Ni is used to compare empirical modelling with CFD simulation. The second-order upwind scheme was used during the discretisation of convective terms in transport equations. The normalized maximum residual to stop iteration was set at 10^{-6} . The validation case has operating conditions and transport properties listed in Tab. 2 and Tab. 3. The validation case has the operating conditions and transport properties listed in Table 2.2 and Table 2.3.

N_p	374
d_p	3 mm
Inlet velocity	1 m/s (Re=446)
Inlet T	283 K
ε_{void}	0.53
\dot{q}	7943562 W/m ³
Total Power, W	37.44 W
Flow Regime	Laminar
Grid, CVs	$8 \cdot 10^6$

Table 2.2: Operating conditions for the CFD validation

	Gas	Solid
Density, kg/m ³	1.225	8900
Cp (Specific Heat), J/kg K	1006.43	444
Thermal Conductivity, W/m K	0.0242	91
Viscosity, kg/m s	$1.79 \cdot 10^{-5}$	–

Table 2.3: Transport properties used in the CFD validation

The visualization of particles temperature and wall temperature predicted using our model and CFD-based simulation is shown in Fig. 2.12. The average temperature of particles along the z-axis is plotted in Fig. 2.13. Relatively good agreement is found, explained by the fact that the side walls are thermally isolated and the particles are heated by a volume source. Thus, the wall channelling effect does not play a significant role in the heat balance for particles. However, it should be noted, that excluding the wall channelling effect from consideration in our model may lead to some inaccurate prediction of the particle temperature because we utilize only the Gunn relation, which is valid only for the bulk of the packing. To take wall channelling into account, the domain should be split into two virtual coaxial cylinders, where the Gunn relation is used in the central region and a special Nu relation taking into account the wall channelling effect is used in the outer cylinder. The effect becomes obvious when the velocity profile is examined in Fig. 2.12c. There is a delay in the balance of temperature distribution due to the velocity difference in the fixed bed. Because the 1-D empirical model does not account for this effect, there is some discrepancy between the particle temperatures. However, since the cases under investigation have much larger diameters than the validation case, the wall channelling effect can be ignored. In a scenario where the cross-sectional diameter is over 10 times the particle diameter, the heat transfer coefficient should be close to the empirical equation.

2.6 Results

The mass flow rate of the gas is set at 0.05 kg/s. The mass flow rate is chosen based on three criteria, conversion rate, fluidisation speed and pressure drop. The current of the fixed bed is adjusted so that the gas temperature at the exit of the fixed bed is 1300K. The Reynolds number is calculated according to Eq. 2.23, based on the superficial velocity, defined in Eq. 2.24, and the mean particle diameter. The mean particle diameter is calculated based on surface area, see Eq. 2.25. The resultant Reynolds number is between 400 and 600.

$$Re = \frac{\rho u_s D_{mean}}{\mu(1 - \varepsilon_{void})} \quad (2.23)$$

$$u_s = \dot{V}/A_b \quad (2.24)$$

$$D_{mean} = \sqrt{\frac{\sum_{i=1}^N D_i^2}{N}} \quad (2.25)$$

The current of the fixed bed is adjusted so that the total heating power remains constant for all cases. The operating conditions are listed in Tab. 2.4 are used for simulation. Table 2.4 shows input conditions (e.g.

volume fraction of catalyst, ε_{cat} , electrical power input, \dot{E}_g , Reynolds number) and output conditions such as total electrical current I and the electrical potential difference U . The total current passing through the fixed bed is in the magnitude of 1000A. Despite a large current through the bed, the current is well distributed that the maximum current through each particle is no more than 100A. In Fig 2.11, the temperature range inside each particle is shown to related to the current. 100A of current corresponds to a contact point less than 100K over average temperature in the particle when r_c/r_p is 0.01.

As a basic case we use 4mm-diameter catalyst particle. A 2mm diameter was a good size for catalyst particle. The radius was just under the ratio of the size of the octahedral sites in a close packed structure. The ratio ensures not only the maximum amount of catalysts can fit in the naturally occurring gaps between conductors, but also the catalysts are not easily percolating through the gaps towards the bottom of the bed.

ε_{cat}	Re	Nu	R_{tot} , Ohm	I_{tot} , A	U , V
0.06	680.47	16.62	0.0042	1664	6.94
0.11	621.47	16.66	0.0043	1636	7.06
0.16	572.57	16.72	0.0047	1565	7.38
0.20	535.07	16.75	0.0049	1534	7.53
0.24	507.83	16.74	0.0053	1482	7.79
0.27	486.05	16.71	0.0066	1318	8.76
0.30	469.05	16.67	0.0074	1248	9.25
0.33	455.55	16.55	0.0081	1194	9.66
0.36	445.12	16.48	0.0104	1055	10.94
0.38	434.61	16.43	0.0084	831	13.89
0.40	426.18	16.36	0.00102	752	15.35

Table 2.4: Results of simulations using parameters $\dot{V} = 0.1m^3/s$, $T_i = 300K$, $T_o = 1300K$, $Q_h = 11544$ Watt.

Yade simulation showed that the initial mixing conditions affect packing condition in the fixed bed. Void fraction, structural rigidity and electric conductance were significantly affected by packing for the same catalyst proportion. Structured packing gives a good uniform conduction through the fixed bed, but it is impossible to achieve in a gravity condensed fixed bed. Instead, the achievable state is a random packing, where the scale of resolution is a few particles. Therefore, our simulation produced randomly mixed solids discharged through a cone to settle in a cylinder, resulting in a randomly packed but controlled bed of particles.

The conducting paths of electric current are shown in Fig. 2.14. The conducting paths were well distributed in the bed to allow for uniform Joule heating. However, as the more non-conductive catalysts were added, the contact between conductive particles was gradually worsened. Based on visual observation, the dividing case is where the catalysts occupy 0.30 of the total solid volume fraction, where the number of conducting paths dramatically reduced. Any more catalyst added in the fixed bed would result in very non-uniform Joule heating.

The steady state temperature of particles computed are shown in Fig. 2.15. The particles with temperature above 950K were active catalysts on which reactions occur. The temperature of the catalysts were very close to conductors due to conductive and radiative heat transfer between particles. Gas bulk temperature must be at least 100K lower than particle temperature under convective conditions. The enthalpy change absorbed significant amount of heat, which lowers the gas temperature further. The lower gas temperature was advantageous for energy efficiency, reliability and safety.

The simulation used room temperature for gas entering the reactor. The initial low temperature resulted in non-reaction at the lower region of the reactor. It is better to preheat gas to maximize reaction. One option to preheat gas is to exchange residual heat in the exit stream with feed stream. Thus the energy in the exit stream is saved and the overall efficiency is improved. Such design is already used in commercial gas-fired SMR. In fact, barring changes for heat mechanism, most of the practices of the gas-fired SMR

can be incorporated into the electrically heated system. Therefore if the concept is proven successful, the technology has good potential for commercialization.

The performance of the fixed-bed reactor depends on temperature and surface area. While high volume fraction of catalysts has large surface area, temperature is very non-uniform. Therefore most of the reactor volume is too cold for reaction to occur, resulting in low conversion. On the other hand, low volume fraction of catalysts has too little surface area. The overall performance of the reactor can be evaluated by calculating the total surface area of catalysts above reaction temperature. As shown in Fig. 2.16, the amount of active surface area steadily increases and peaks off between 0.24 and 0.31. Although higher catalyst volume may have more active surface area, the cases over 0.34 are unqualified because of particles exceeding melting temperature. Since conduction is more unpredictable and unreliable as catalyst increases, the optimal catalyst volume fraction is between 0.24 and 0.30.

The impact of the flow rate on the temperature distribution is shown in Fig. 2.17 and Fig. 2.18. In Fig. 2.17, the temperature of the particles was visualized for a fixed bed where the gas flow rate was raised to 0.5kg/s and 5kg/s, 10 and 100 times the original condition respectively. While the heating power remained the same, the temperature gradient in the gas phase diminished. The increased flowrate also resulted in high Nusselt number and particle-gas heat transfer. However, the temperature difference between conducting particle and non-conducting particles was still high. Therefore the increasing the flowrate does not help the thermal uniformity in the fixed bed.

2.7 Conclusions

The new type of fixed bed reformer using Joule heating has been developed in this article. Compared to conventional steam-methane reforming process, the largest benefit of an electrically heated fixed bed is thermal efficiency. Heat is internally supplied, which reduces heat loss to the surroundings. The solid phase is hotter than the gas phase, which reduces waste heat in the exit stream. Since heating occurs uniformly in the reactor, temperature is in the cross-sectional area also homogeneous, as is reaction rate.

The design criteria of an electrically heated fixed-bed reactor is investigated. The ratio of the radius and the volume fraction of catalytic particles are two important design parameters that affect the performance of the reactor. For conductive particles that are 0.5 cm in radius, the optimal radius of catalyst particles is determined to be 0.2 cm. The choice of catalyst size is made upon its superior performance in electrical conductance and surface-area-to-volume ratio. The 0.2 cm catalyst is also large enough to allow good thermal conductance and gas flow continuity. 11 cases of fixed bed with different volume fractions are evaluated by simulating electrical current and temperature profile in the fixed bed. The suitable amount of catalyst particles must have stable electrical conduction and safe operating temperature. The volume fraction of catalyst particle is optimized based on the total surface area of the catalytic sites, which is proportional to total surface area of catalysts at elevated temperature. The optimal catalyst volume fraction is 0.27.

2.8 FIGURES

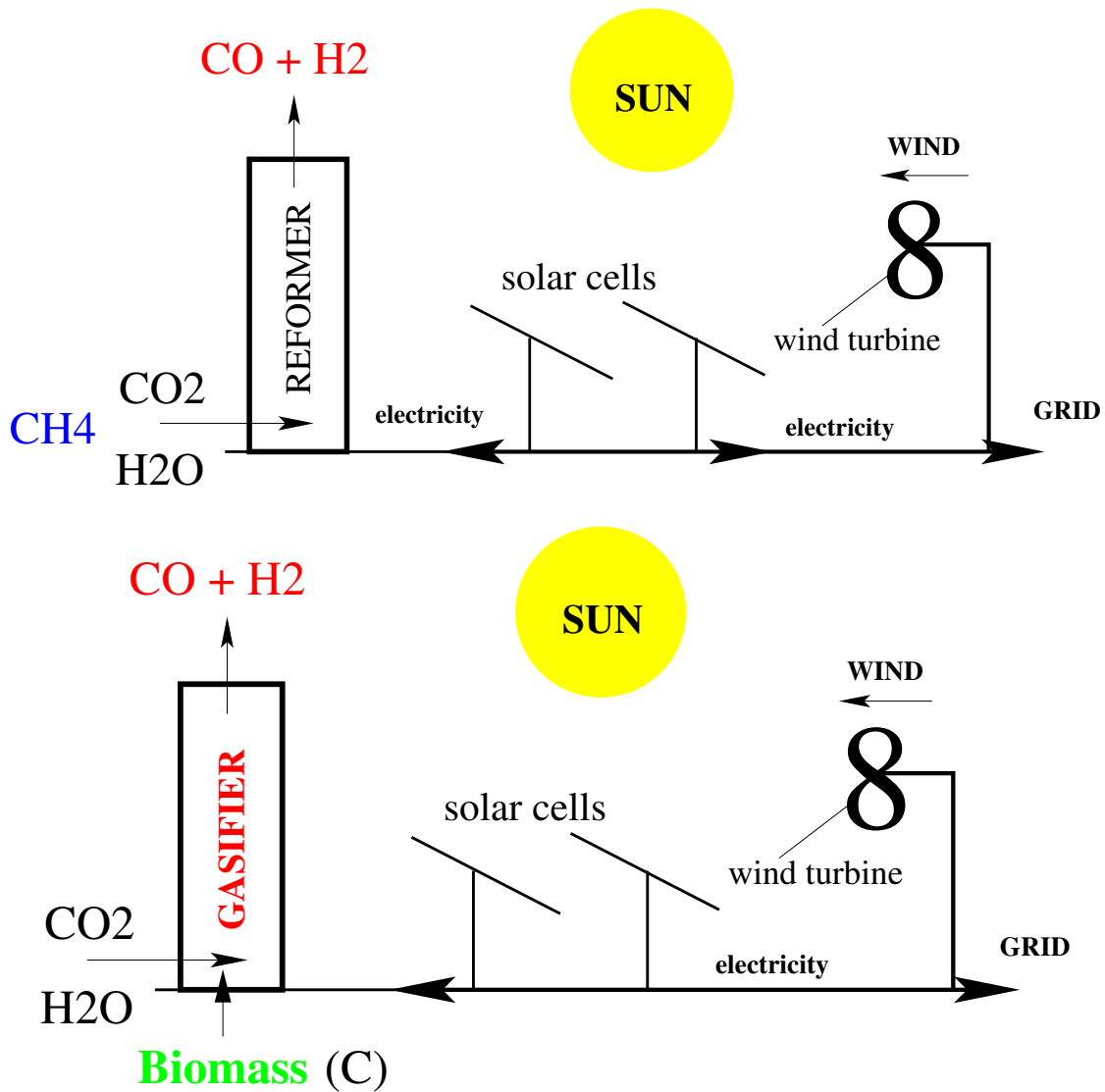


Figure 2.1: Principal scheme of the energy to chemicals (E2C) concept.

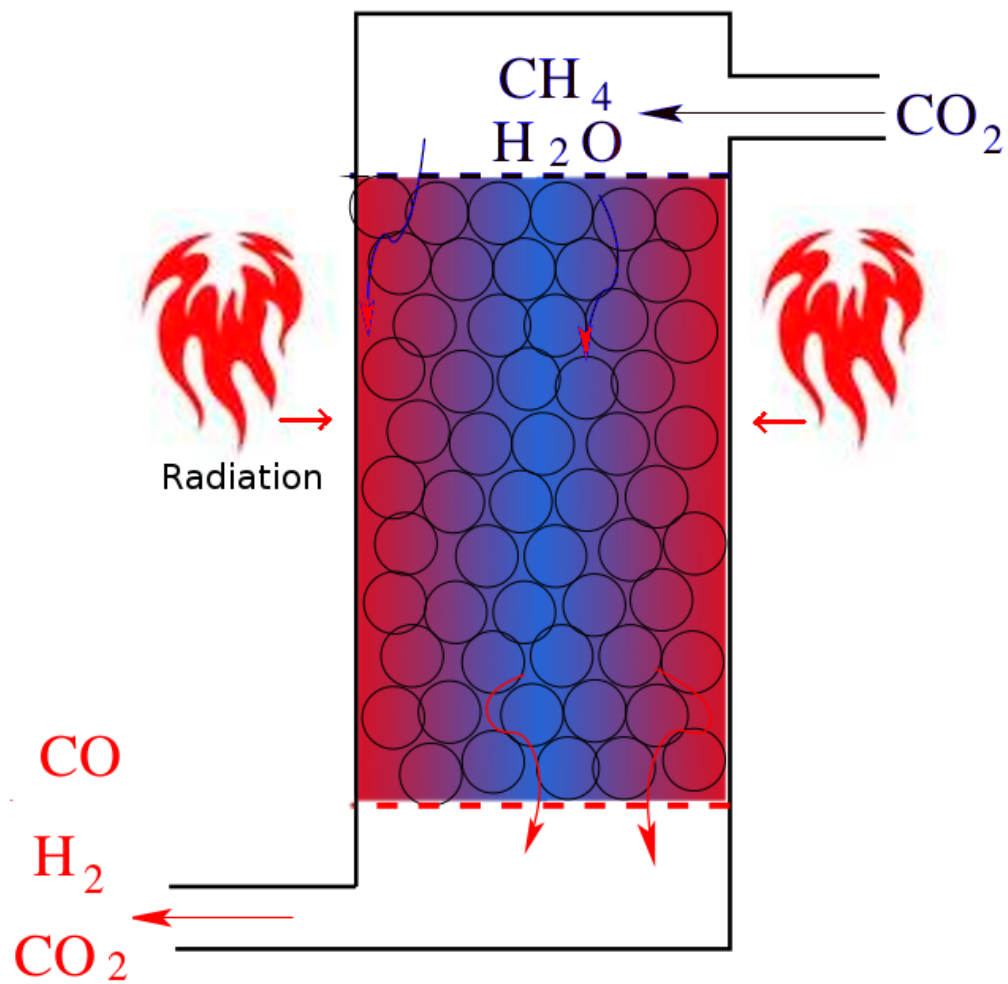


Figure 2.2: Principal scheme of conventional SMR-reactor.

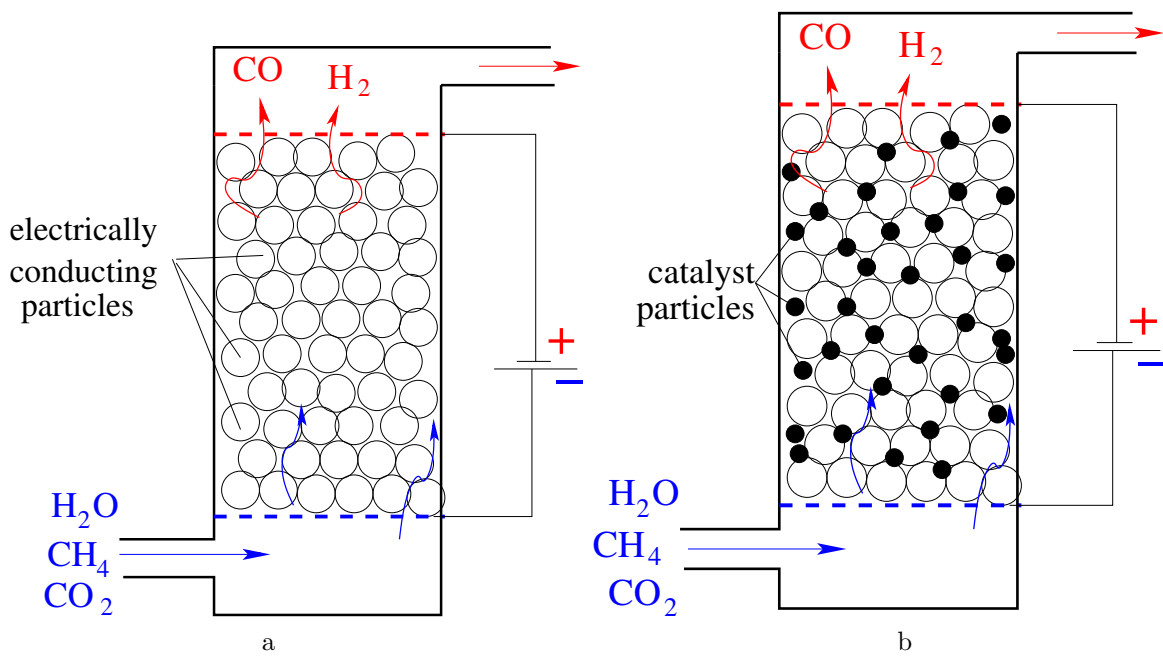


Figure 2.3: Principal scheme of a standard reformer [48] (a) and a new fixed bed reactor (b) heated by DC discharge using the Joule heating effect.

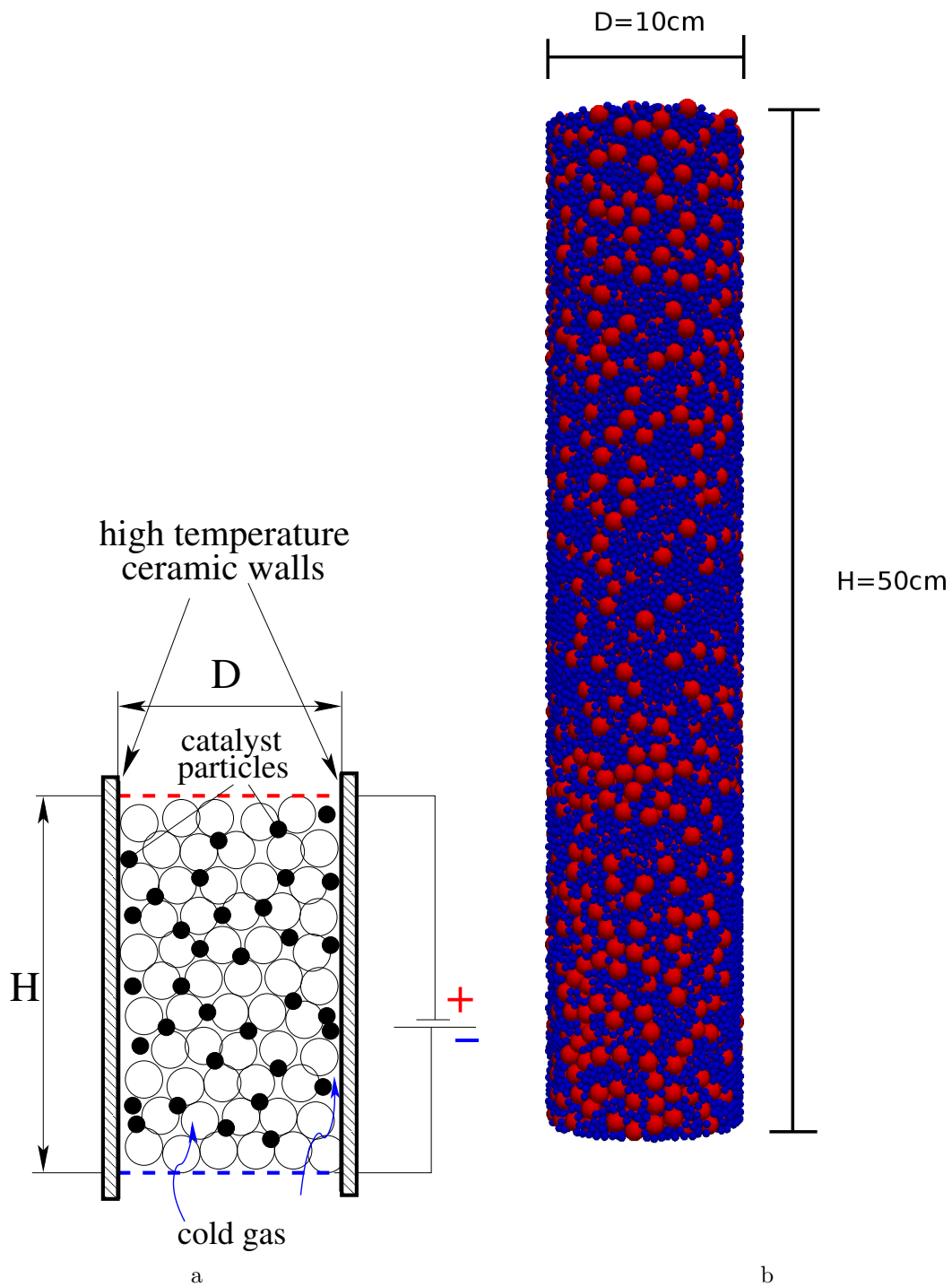


Figure 2.4: Principal scheme of a bed (a) and DEM-simulated fixed bed filled with conducting and catalyst particles, 1cm and 0.4cm in diameter respectively

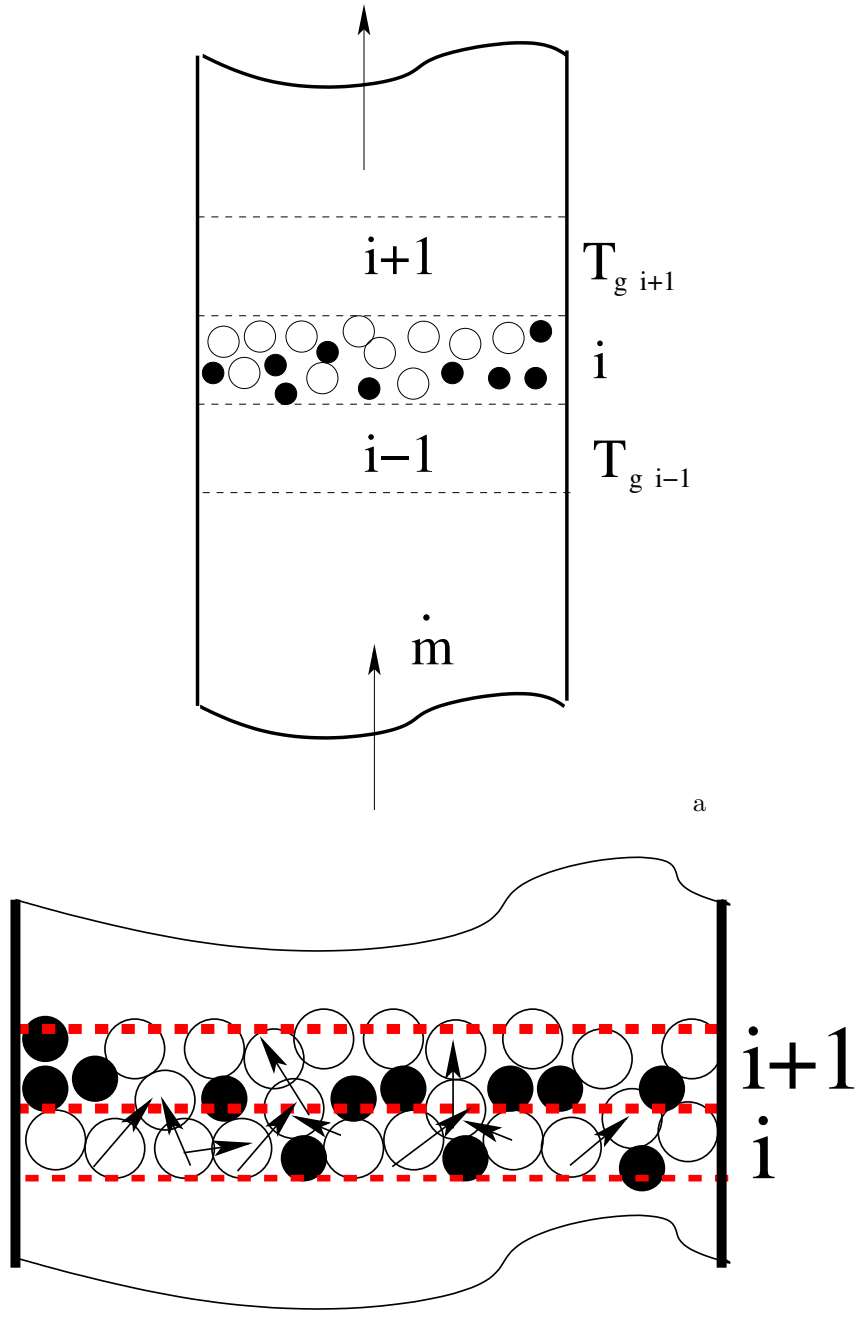


Figure 2.5: Schemes explaining calculation of T_g along reactor height (a) and electrical current distribution inside the reactor (b).

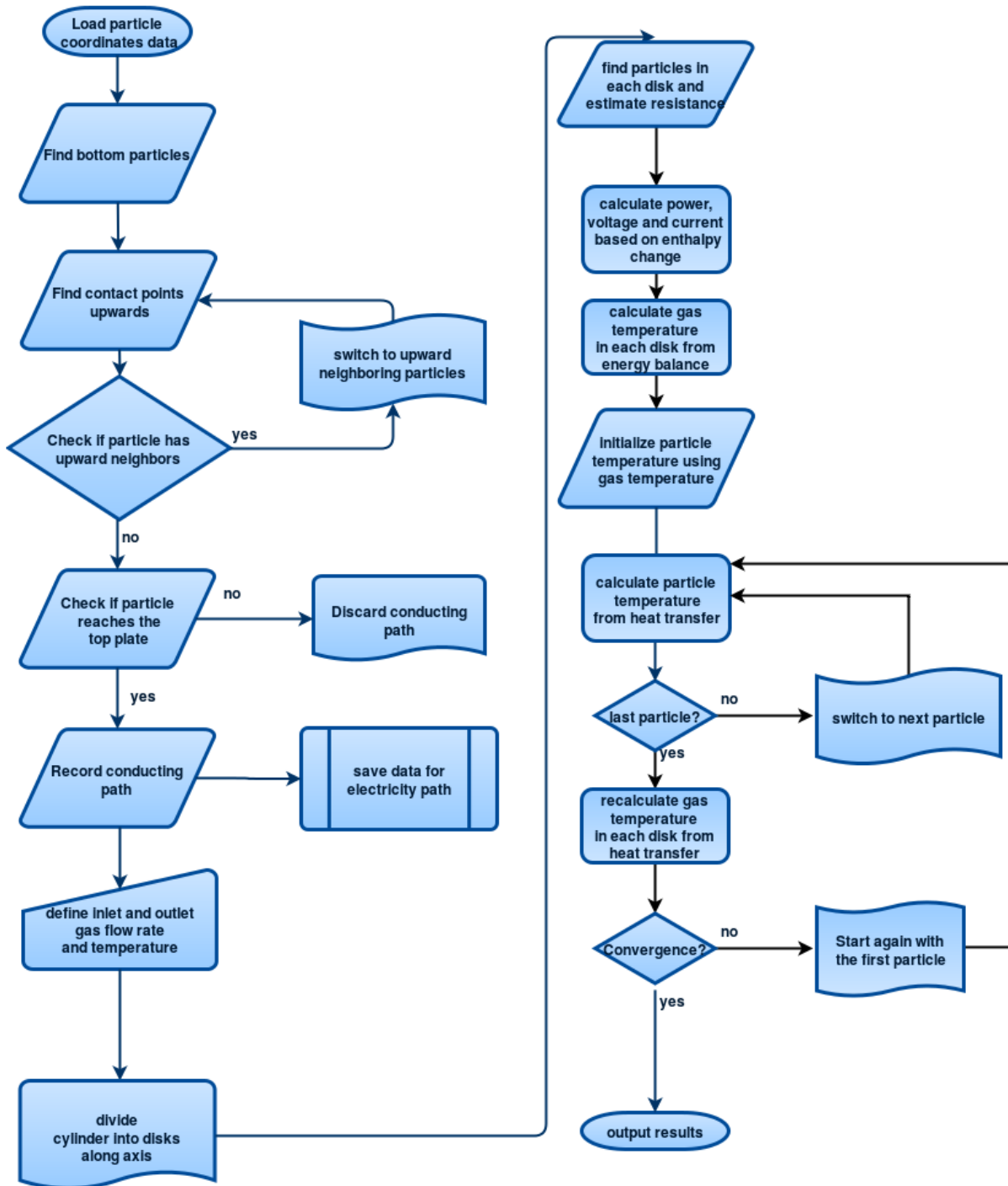
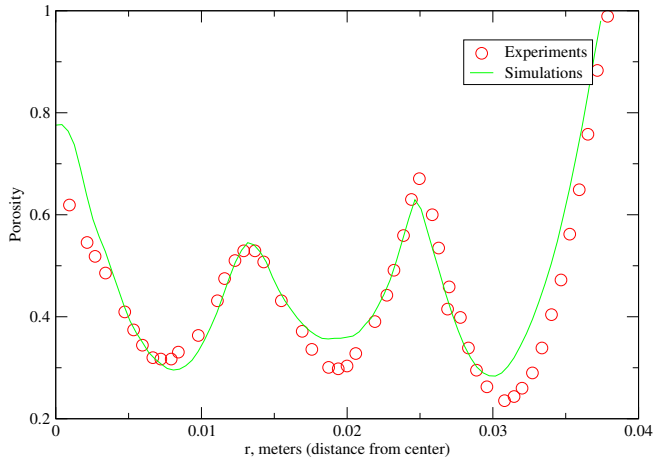
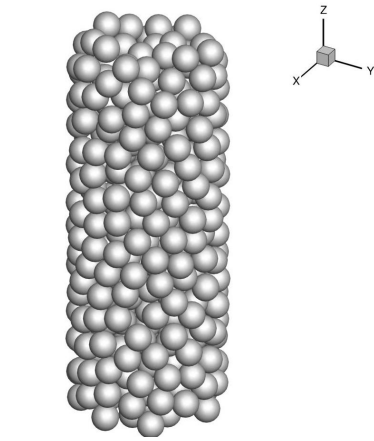


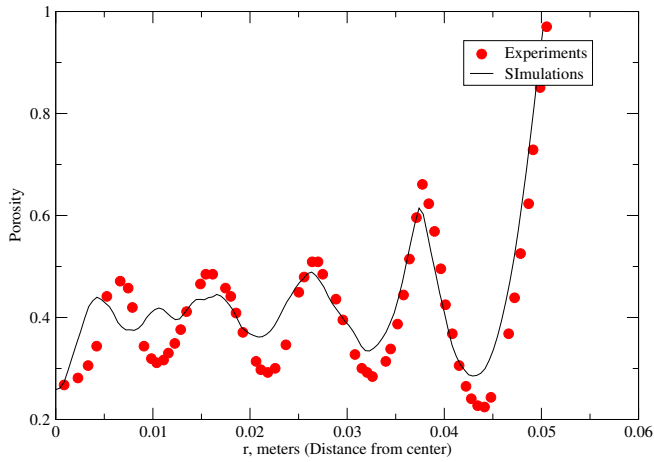
Figure 2.6: Flow-chart diagram of computational algorithm used to calculate the temperature distribution in the endothermic fixed bed heated by DC discharge.



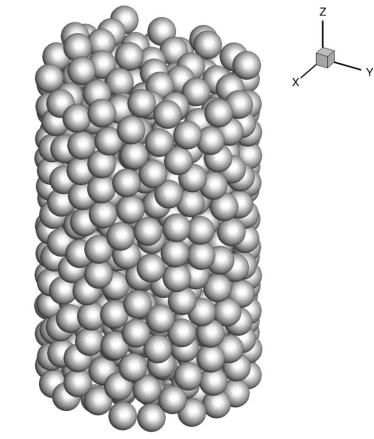
a



b

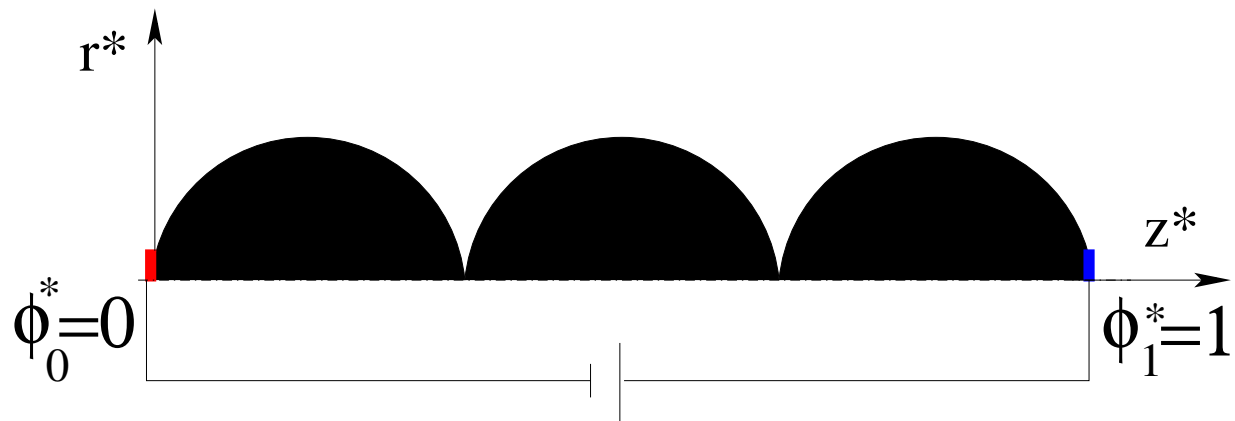


c

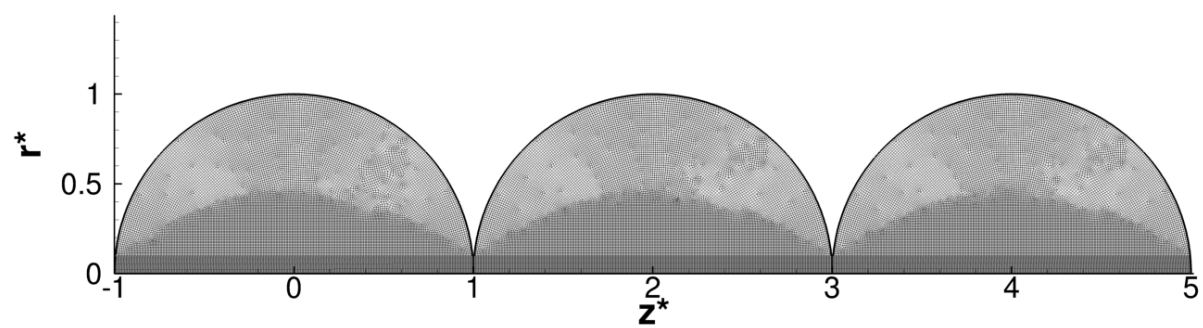


d

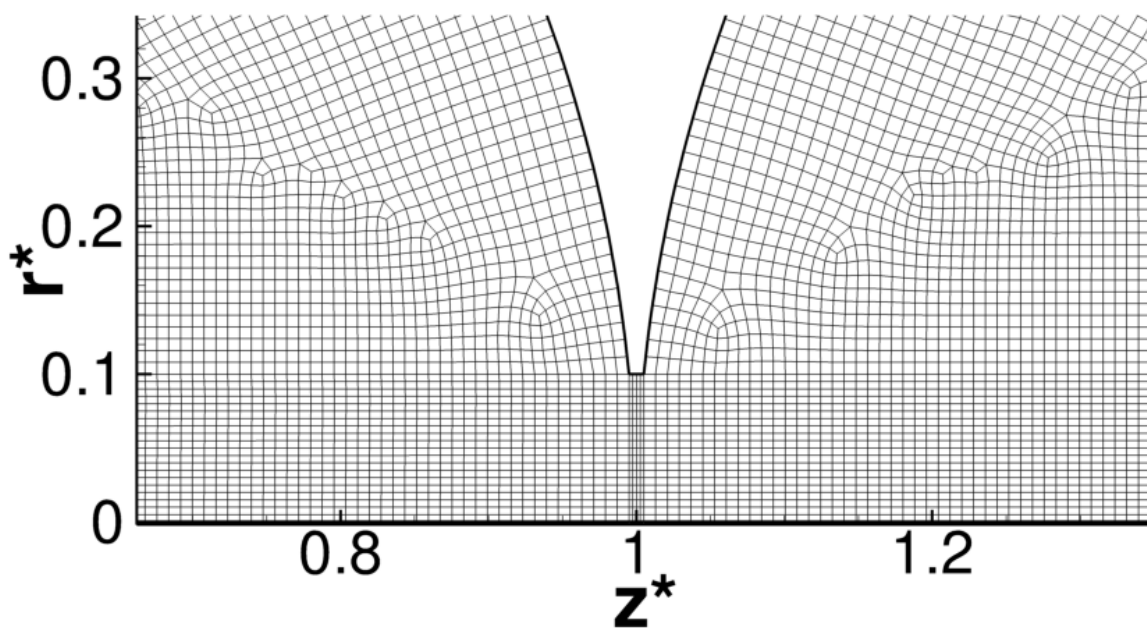
Figure 2.7: Validation of the DEM software used in this work against experimental data [1] for different ratios between tube diameter and particle diameter: a) radial void fraction distribution for $\frac{D}{d_p} = 5.96$; b) generated packing for $\frac{D}{d_p} = 5.96$; c) radial void fraction distribution for $\frac{D}{d_p} = 7.99$; d) generated packing for $\frac{D}{d_p} = 7.99$.



a



b



c

Figure 2.8: Scheme of setup and the numerical grid used for the modeling of electrical field distribution.

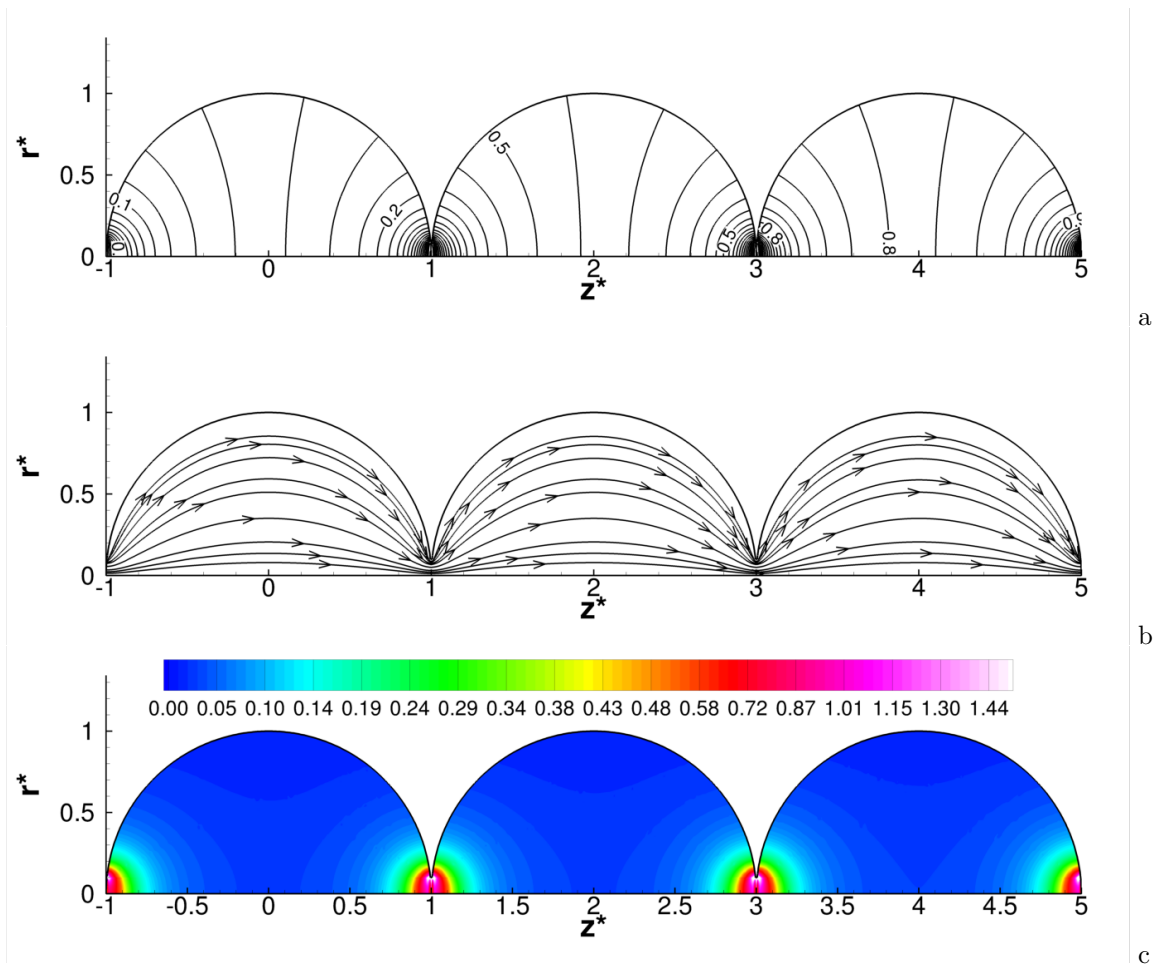


Figure 2.9: Spatial distribution of the nondimensional electric field potential ϕ^* (a), stream lines of the electrical current density (b) and the absolute values of the nondimensional *electrical field intensity* magnitude $\|E^*\| = \sqrt{\left(\frac{\partial\phi^*}{\partial r^*}\right)^2 + \left(\frac{\partial\phi^*}{\partial z^*}\right)^2}$ (c). Here, the radius of the contact area is $0.05r_p$.

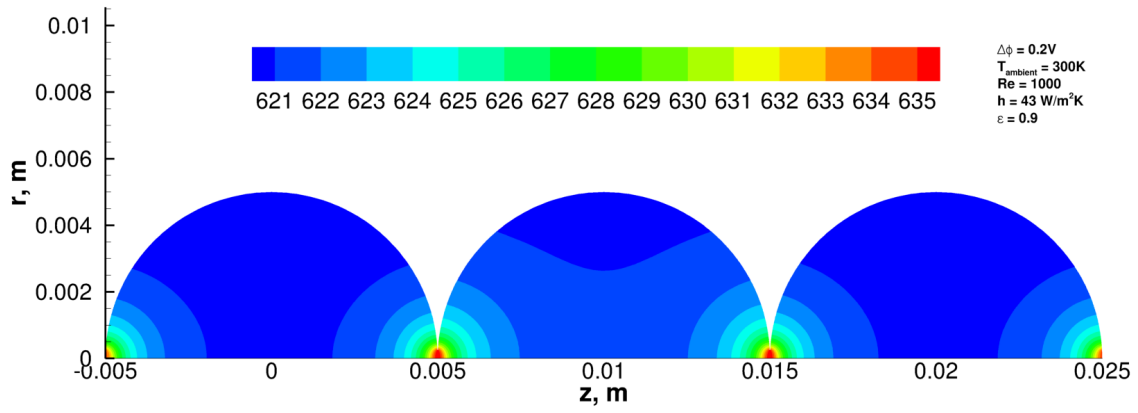


Figure 2.10: Temperature profile of electrically heated particles under convection and radiation.

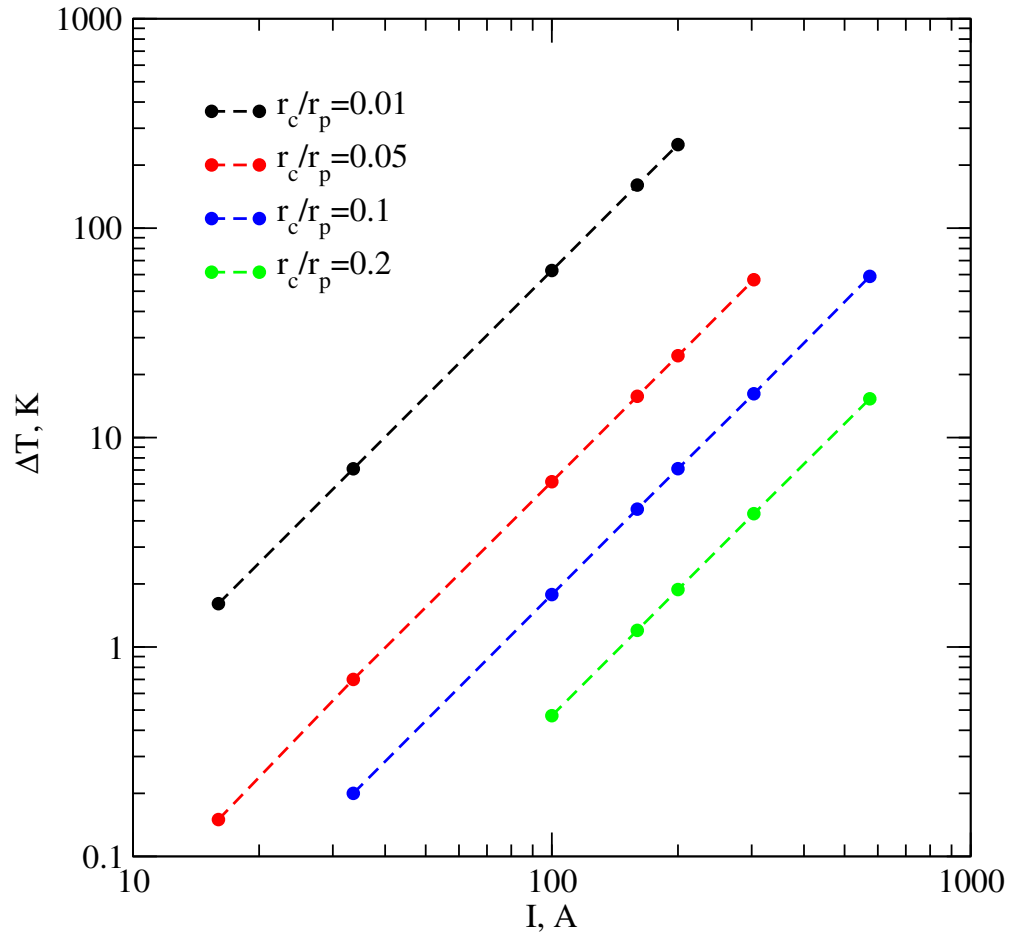


Figure 2.11: Change of the temperature difference inside a particle in relation to the electrical current going through the particle. The radius of the contact area r_c plays a governing role in ΔT .

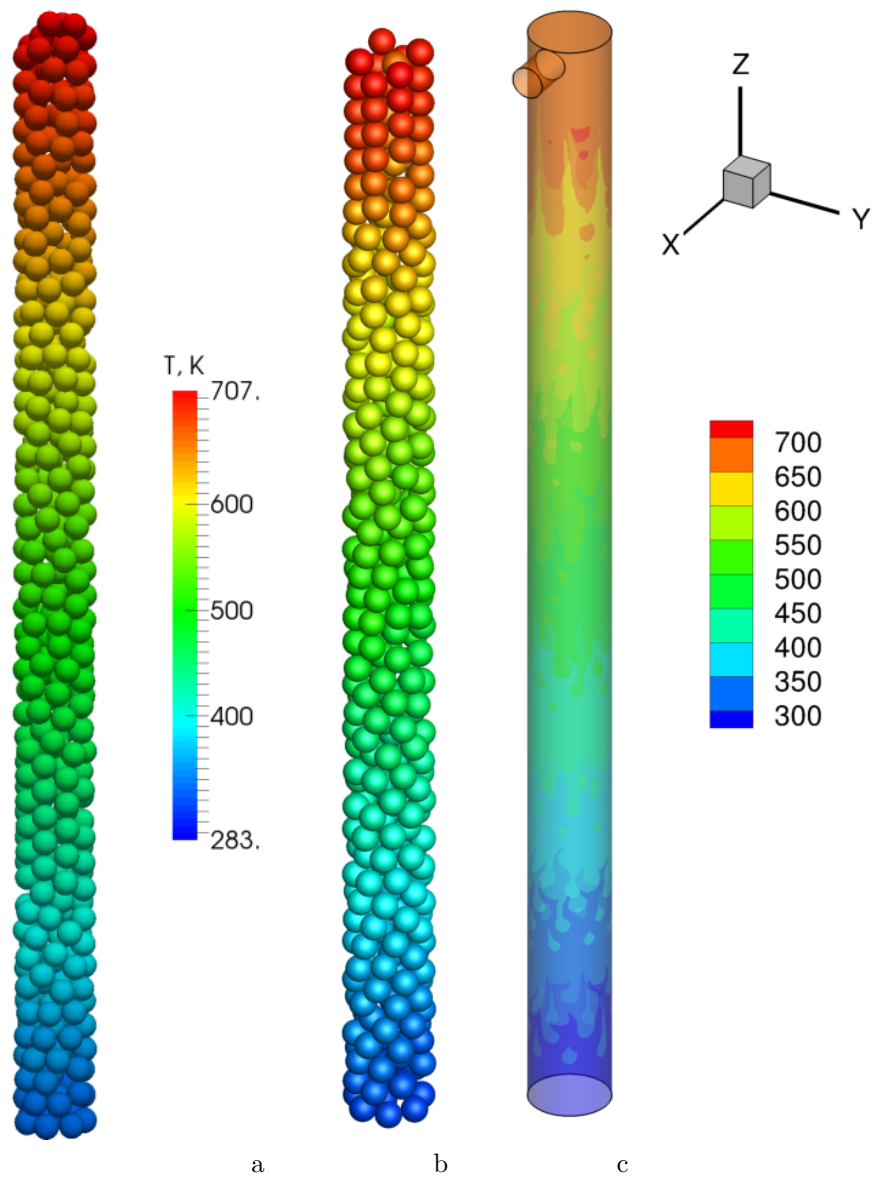


Figure 2.12: Temperature of particles predicted using our model (a), 3-D CFD simulation (b) and (c) wall (gas) temperature

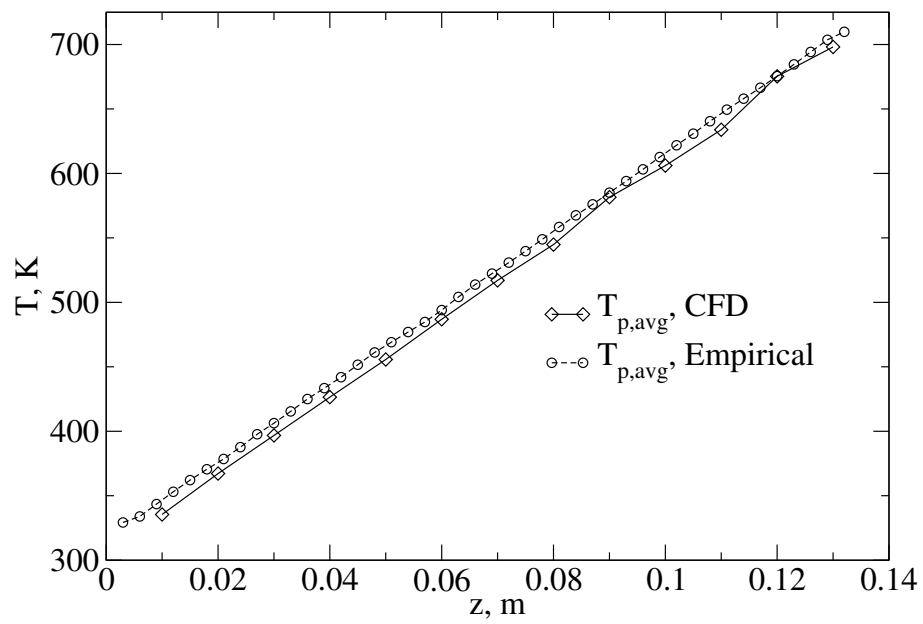


Figure 2.13: Axial profiles of the gas temperature predicted using our model and CFD based model

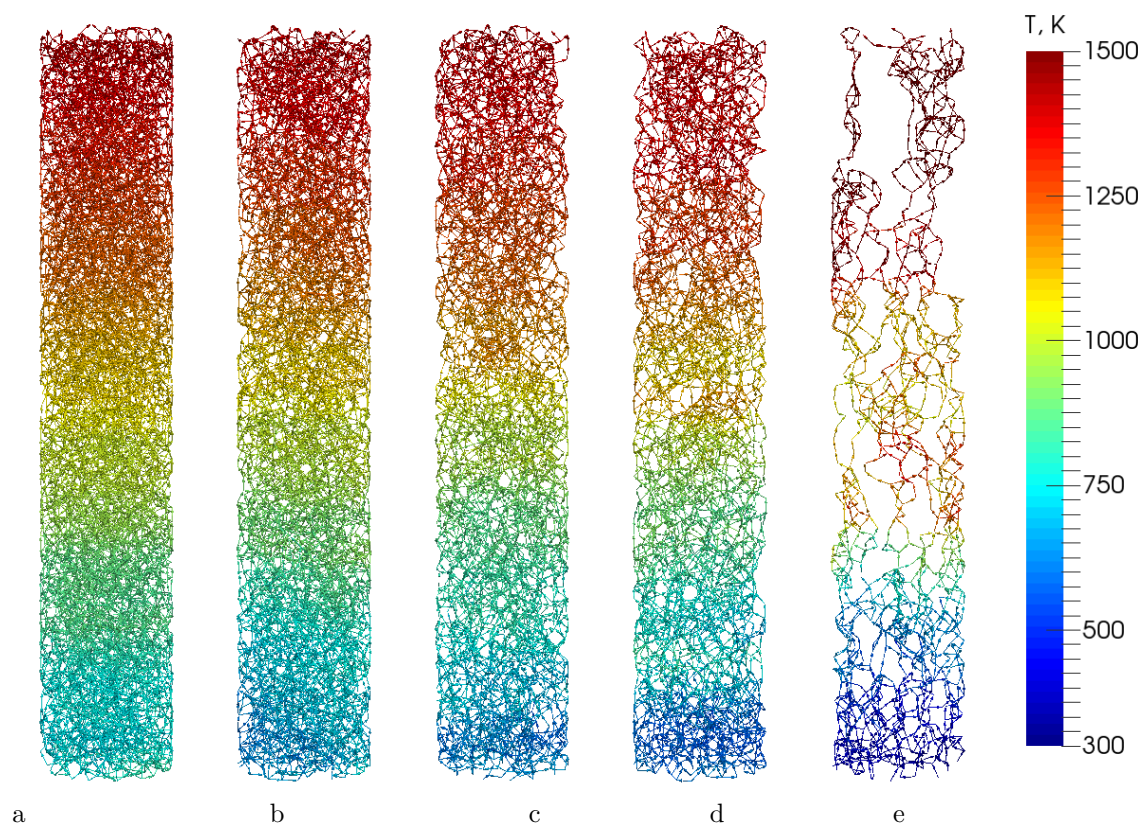


Figure 2.14: Path of the electrical current (colored by the particle temperature) predicted numerically for different values of the volume fraction of catalyst particles: a) $\varepsilon_{cat} = 0.06$; b) $\varepsilon_{cat} = 0.16$; c) $\varepsilon_{cat} = 0.20$; d) $\varepsilon_{cat} = 0.24$; e) $\varepsilon_{cat} = 0.40$;

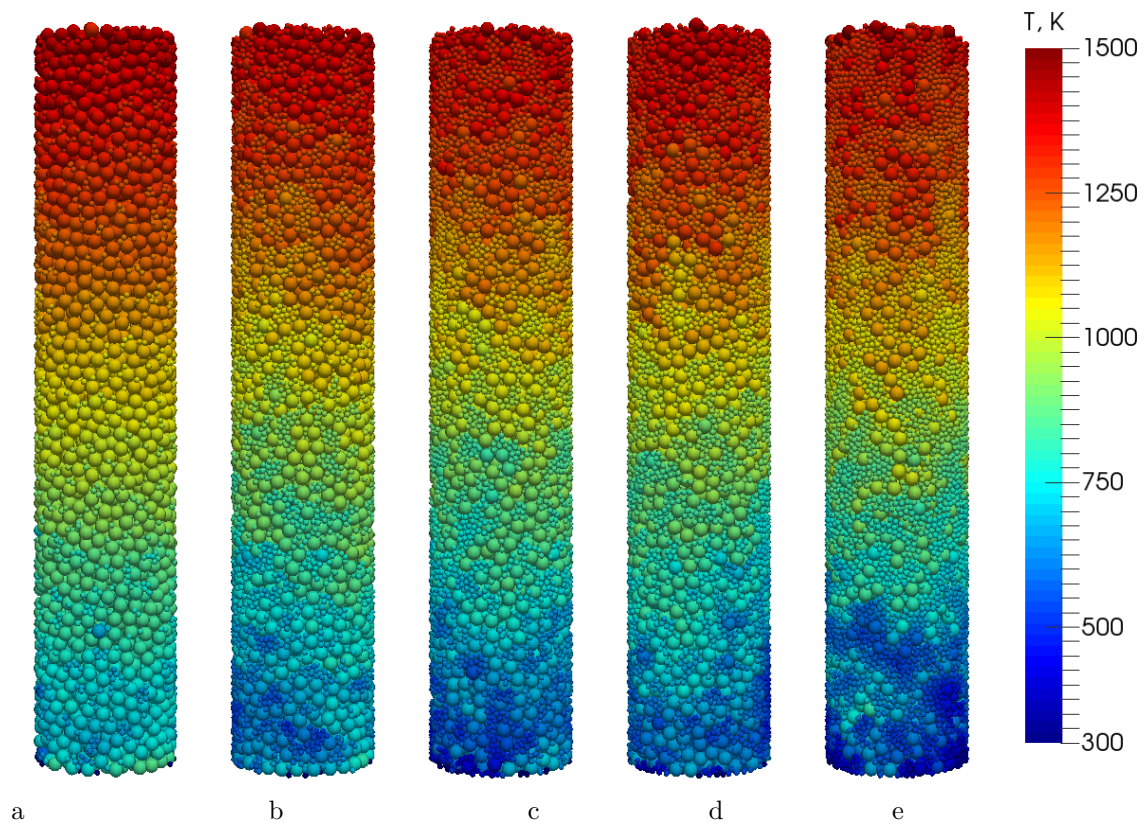


Figure 2.15: Particles temperature predicted numerically for different values of the volume fraction of catalyst particles: a) $\epsilon_{cat} = 0.06$; b) $\epsilon_{cat} = 0.16$; c) $\epsilon_{cat} = 0.20$; d) $\epsilon_{cat} = 0.24$; e) $\epsilon_{cat} = 0.40$;

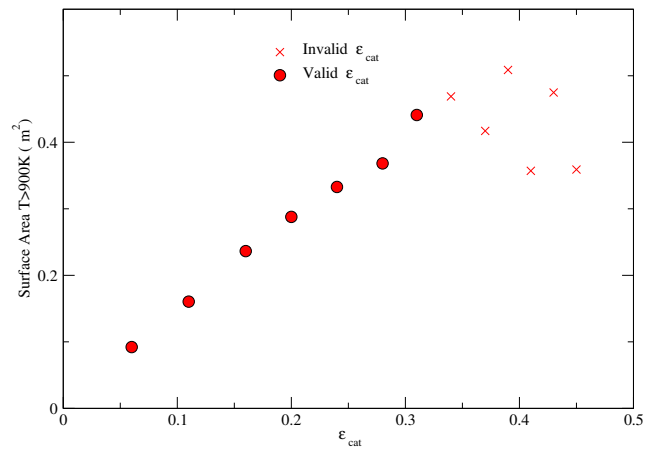


Figure 2.16: Total surface area of catalyst particles which temperature exceeding 950 K calculated for different values of ϵ_{cat} .

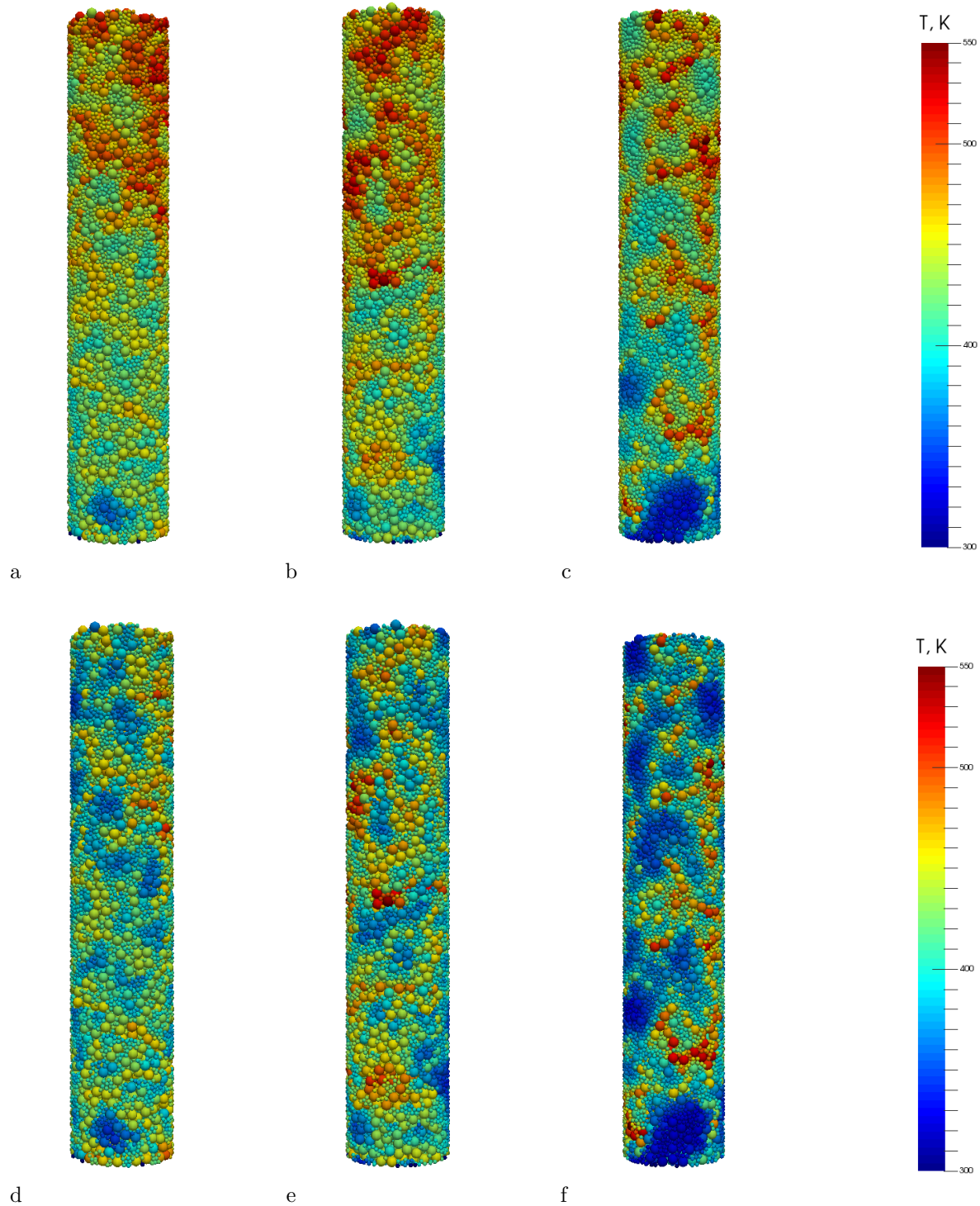
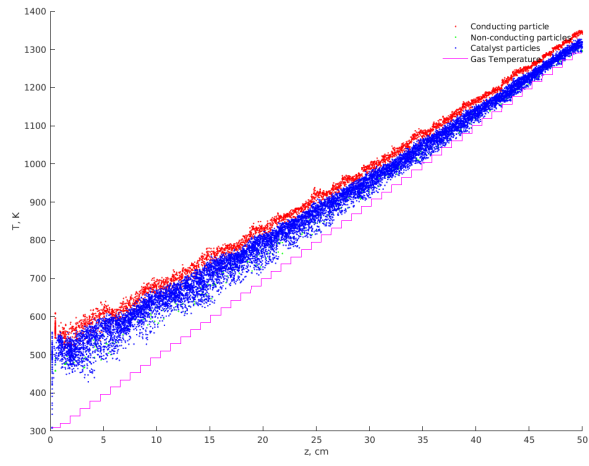
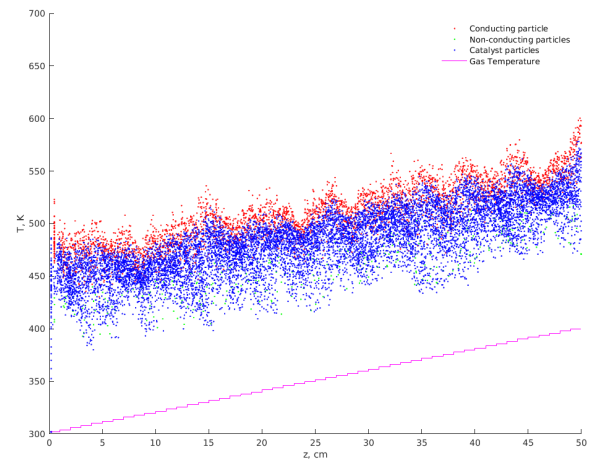


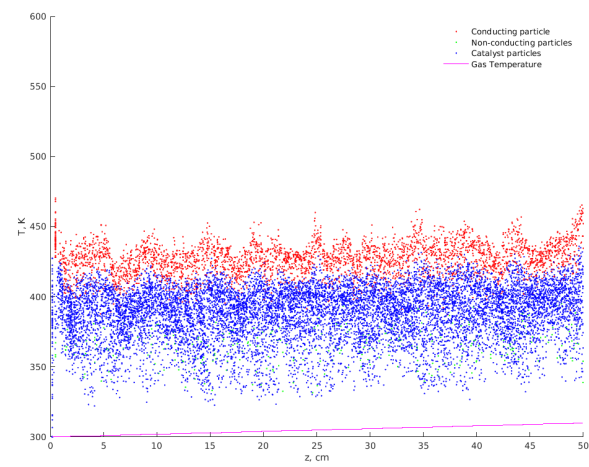
Figure 2.17: Particles temperature predicted numerically for different values of the volume fraction of catalyst particles and gas flow rate: a) $\dot{m} = 10 \cdot \dot{m}_0$, $\varepsilon_{cat} = 0.16$; b) $\dot{m} = 10 \cdot \dot{m}_0$, $\varepsilon_{cat} = 0.24$; c) $\dot{m} = 10 \cdot \dot{m}_0$, $\varepsilon_{cat} = 0.30$; d) $\dot{m} = 100 \cdot \dot{m}_0$, $\varepsilon_{cat} = 0.16$; e) $\dot{m} = 100 \cdot \dot{m}_0$, $\varepsilon_{cat} = 0.24$; f) $\dot{m} = 100 \cdot \dot{m}_0$, $\varepsilon_{cat} = 0.30$. Here $\dot{m}_0 = 0.05$ kg/s.



a



b



c

Figure 2.18: Axial profile of particles temperature predicted for $\varepsilon_{cat} = 0.3$ and different flow rates: a) $\dot{m}_0 = 0.05$ kg/s; b) $\dot{m} = 10 \cdot \dot{m}_0$; c) $\dot{m} = 100 \cdot \dot{m}_0$.

Chapter 3

Phase Change inside a Spherical Capsule

3.1 Introduction

Thermal energy storage (TES) has seen growing interests recently due to the need of energy efficient heating and cooling solutions. Latent heat storage using phase change material (PCM) is especially promising due to its thermostatic nature. In a latent heat storage system, the heat is stored at the interface where phase change occurs. The interface moves away from heat source as the PCM melts. As a result, the rate at which the system harvests or supplies is not constant. The heat storing power depends on heat transfer rate between the source and destination. The heat rate is equal to the quotient of thermal potential and thermal resistance.

$$q = \frac{\Delta T}{R_{th}} \quad (3.1)$$

Therefore it is important to understand how thermal resistance changes at a small scale. Failure to understand mechanism results in a lack of control, which limits the usability of latent heat storage as a heating and cooling system.

In a charging cycle, heat is absorbed as the PCM begins to melt from the surface closest to the heat source. As the interface between solid and liquid PCM moves away, the resistance between the melting heat transfer medium increases. Since PCM has relatively low thermal conductivity, the heat transfer rate for the system is mostly determined by the thickness of the melt. Initially the heat transfer mode is pure conduction. As the liquid thickness increases, flow is able to circulate in the zone and convection becomes the dominant heat transfer mode. In a discharging cycle, heat is released as the PCM melt. However, solidification also has to begin from the surface close to the heat transfer media. In the solid layer, there is no convection. The thermal resistance of a solid layer is easy to predict. The temperature profile of a solid can be solved numerically to not only account for the latent heat stored in the system, but also predict the sensible heat accurately.

One of the methods to improve heat transfer is to encapsulate the PCM materials in small metal shells. Spherical capsules have larger surface area per unit volume compared to cylindrical tubes [60]. The PCM in question, paraffin wax, is a mixture of esters, hydrocarbons, and alkanes. Under the cycling of each melting and solidification, the PCM tends to segregate due to difference in chain length. Therefore shells not only provide good surface area for heat transfer, but also confines the PCM in its space so that segregation does not occur at a larger scale. The shell also protects the PCM and maintains structural integrity for a fixed bed. making heat storage unit a durable device in repeated cycles. However, heat transfer rate is not constant through the process as the PCM gradually melts or solidifies. To model the heat storage units consisting of many PCM capsules, it is necessary to understand the changes occurring in the capsules when the PCM is melting and solidifying. This chapter is dedicated to modeling the melting and freezing of PCM inside one capsule, and deriving a mathematical submodel that can be used in simulation.

Encapsulated PCM can be used in both fixed bed and fluidized bed. In fixed bed, the diameters of the PCM are in the order of a few millimetres to a few centimetres [61]. In fluidized bed, the PCM are often sized less than 1 mm [62]. Reducing the size of the PCM capsules improve heat transfer by increasing surface-to-volume ratio [63], but the volume fraction of PCM is reduced at the same time. Bellan [64] studied the thermal performance of molten salt in spherical capsules, and found that Stefan number is vital to the total heat storage capacity due to sensible heat and the shell thickness is important to the thermal performance of the system. Reducing shell thickness has significant effect on charging time, but shell too thin compromises in mechanical strength. Yu et al. [65] showed that the thickness of the shell made of Cu-Ni alloy should be at least 200 microns for a PCM capsule of 500 microns for it to be used in fluidized bed. In fixed bed, mechanical strength is also an important consideration, as both external pressure due to gravity and internal stress due to thermal expansion have the potential to make the shell crack [66].

In addition to confinement, fins are also often used in capsules. Mahdi et al. [67] showed through numerical studies the enhancement that fins can effectively provide. Fins serve two purposes, first, to increase the thermal conduction in the capsule, and second, to fix the solid PCM in position to reduce the scale of segregation. They help ensure the cyclic behaviour of system so that control is easier. Fins are especially helpful when used in conjunction with nanoparticles. The melting and solidification of PCM in cylindrical annulus is studied by Darzi et al. [68]. Natural convection was found to play a significant part in the heat rate during melting. Inserting fins were especially useful during solidification, but suppress natural convection somewhat, making it not so effective in melting.

Takeda et al. [69] used granulated porous media, where the fixed bed consisted of 35% PCM and 65% porous ceramic by weight, to directly heat and cool air in a ventilation system. The particle diameter was 1-3 mm, which resulted in great heat transfer properties, but high pressure drop. The system is suitable for low-flowrate ventilation, in a moderate climate, but ineffective for intensive heating or cooling.

Energy loss due to friction is one of the most important metrics designing a TES because it determines the efficiency of the system. There are a number of factors determining the loss of energy of flow in the fixed bed, including the size and shape of the particles, the void fraction and flowrate. Ergun [70] defined friction factor through analysis of pressure drop and correlated the friction factor to the size of particles in the bed. Standish and Drinkwater [71] used sphericity to characterize the shape of particles in packing. Chandra and Willits [72] reported that pressure drop depended on particle size and void fraction, but the convective coefficient only depends on size and flow rate. This conclusion was in disagreement with more recent studies, as Singh et al. [73] studied the effect of particle shape in a fixed bed for energy storage. Nusselt number was found to be highest for spherical particles with minimum void fraction, which gave spheres the best thermohydraulic performance despite having high friction factors [74]. Inelaborate models found reasonable success through the use of effective conductivity [75]. However, the concept of effective conductivity is not theoretically sound, as it is an empirical based on conductive equations. Convection is a distinct mechanism where momentum transport is involved. Thus any change to the conditions under which effective conductivity was obtained leads to uncertainty of its validity.

Before the development of modern computational technologies, melting and solidification has been studied analytically. Paterson [76] formulated an analytical solution using one-dimensional heat transfer only by conduction. Grimado and Boley [75] solved the same equation using isotropic boundary and for constant and variable heat influx conditions. Despite various efforts to investigate the process, plausible solutions have not been reported until the extensive use of numerical methods. These methods worked for solidification under the correctly assumed conditions. Ismail [77] studied the solidification of PCM inside a spherical capsule numerically. The effect of size, thickness and material was investigated in Ismail's paper. Ismail [78] also studied the charging and discharging of a latent heat storage system in the form of a fixed bed. The numerical and experimental results showed that the charging/discharging time is predominantly decided by heat transfer in the spherical capsule, for a capsule sized 0.077m in diameter. Lakshmi Narasimhan [79, 80] et al. studied the solidification of a PCM dispersed with particles. The macro-particles are effective when the Stefan number is low. Other authors also studied the solidification in spherical capsules numerically and experimentally [81, 82]. Overall, the solidification of PCM in capsules are easily to understand and easy to compute. The researchers were able to reach a consensus that heat transfer during solidification of PCM in a capsule is dominated by conduction.

As for melting, results varied due to difference in the conditions and models. Moore and Bayazitoglu [83] studied the melting inside a spherical capsule. Moore and Bayazitoglu derived their solution assuming that the solid sank to the bottom of the sphere and flow is constantly driven by pressure through the gap between solid boundary and shell. The flow between gap is approximated using flow between parallel plates and velocity is calculated using force equilibrium instead of momentum balance, meaning inertial terms are neglected. Natural convection arising from buoyancy is also neglected. As a result, energy storage is shown to be directly proportional to time. Because of the neglected terms, their model only applied when Reynolds number (Re), Stefan number (Ste) and Fourier number (Fo) are small. Khodadadi and Zhang [84] were the first to apply fully numerical solutions to melting inside a sphere. However, the quality of their grid was limited and the accuracy was poor.

In a more recent effort, Tan [2] investigated melting of PCM using thermal couples and photography for experiments on both constrained and unconstrained melting inside a spherical glass capsule full of n-octadecane (paraffin), with different wall temperatures and subcooling temperatures. The experiments successfully captured the shape and temperature changes illustrated the convective currents arising from gravity in both cases. Constraining the solid reduces the heat flux because the solid can no longer be in contact with the shell directly. However, constrained melting has stabler, smoother curve because convection dominates almost the entirety of the melting process, except for the initial stage before liquid layer forms. Despite a reduction in peak performance, constrained PCM provides steady energy charging/discharging rate and identical overall capacity. Tan et al. [3] went on to use computational simulation to model constrained melting. However their simulation showed poor consistency with experimental data. The simulation generally captures the trend of liquid fraction change and vortex forming during the melting process. However, there have been several noticeable mistakes and areas of improvement. For example, the simulation assumes subcooling of 1°C, but compares to experiment with subcooling of 20°C. Dirichlet boundary condition is assumed, though the experimental data clearly shows temperature changes in the boundary. Thermal resistance in the shell and from external convection must be considered. The large fluctuation and irregular shape indicates ill-proportioned conductive and convective heat transfer. In a related research, Rizan et al. [85] showed that the flow created from melting on the bottom of solid had sufficient momentum to move the solid away from upright position, especially in cases with higher heat input. The movement indicates small disturbance in the flow causes turbulence. Under such circumstances, the flow becomes nonaxisymmetric and likely chaotic. The melting rate and heat absorption rate will not be determined numerically. Despite occurrence of chaotic movement, S.F. Hosseinzadeh et al. [86] performed numerical simulations for unconstrained melting using axisymmetric 2D space and developed dimensionless correlation which agrees with experimental data from cases where turbulence does not occur. To simplify the problem and ensure axisymmetry, constrained melting is the interest of this study and it should have the advantage in stability and consistency.

3.2 CFD Numerical Formulation

The melting and solidification are simulated using ANSYS Fluent 16.2. Since the previous simulation and experimental data have proven that the effect in the tangential direction is small [3, 86], a 2-D axisymmetric model is used to simplify the simulation. Three built-in models are used to solve the equations in this problem, Flow, Energy and Solidification/Melting. Because of low velocity inside the sphere, flow is assumed to be laminar and based on incompressible forms of Navier-Stokes equation. Incompressible laminar flow is assumed because of the low current velocity which is induced only by natural buoyancy. Energy balance is based on enthalpy equation, which separates into two parts, sensible heat and latent heat. Solidification and melting is a model that calculate liquid fraction from temperature. It is coupled with momentum and energy equations to model the changes happening in the partially melted region.

3.2.1 Transport Properties

Several assumptions are made to simplify this problem. The thermal conductivity, dynamic viscosity, specific heat capacity and thermal expansion coefficient of the fluid are considered constant as the change does not have notable effect on the results. The melting temperature is represented by solidus and liquidus

Property	density	specific heat capacity	thermal conductivity	dynamic viscosity
Symbol	ρ_o	c_p	k	μ
Unit	kg/m ³	J/kg-K	W/m-K	kg/m-s
Value	772	2330	0.1505	0.00386
Property	thermal expansion coefficient	Melting heat	Solidus temperature	liquidus temperature
Symbol	β_T	L	$T_{solidus}$	$T_{liquidus}$
Unit	1/K	J/kg	K	K
Value	0.00091	2435000	301.15	301.35

Table 3.1: Transport properties of liquid paraffin

temperatures where liquid fraction varies linearly between the melting range. Latent heat of fusion varies linearly with liquid fraction in the partially melted zone.

Boussinesq approximation is chosen to handle density change for two primary reasons. First, the inertial momentum change due to volume change is negligible. Second, the liquid volume change is unattainable in the simulation since it is put in confined volume with fixed grid. Boussinesq approximation allows the equations to treat density as a constant in the governing equations except when it is multiplied by gravitational acceleration.

The transport properties of the fluid are listed in the following table.

3.2.2 Governing Equations

Continuity, momentum balance and energy balance are three sets of governing equations that need to be considered in this study. The phase change problem requires a model to handle liquid and solid. Instead of tracking the liquid-solid interface explicitly, liquid fraction ϕ_l is defined as a function of temperature in three cases.

$$\phi_l = \begin{cases} 0 & \text{if } T < T_{solidus} \\ 1 & \text{if } T > T_{liquidus} \\ \frac{T - T_{solidus}}{T_{liquidus} - T_{solidus}} & \text{if } T_{liquidus} < T < T_{solidus} \end{cases} \quad (3.2)$$

With liquid fraction being a function of temperature, one set of equations can be applied to both liquid, solid, and partially liquid zones, removing the need to track melting interface, making the computational algorithm much more stable and robust. This model has sounder reasoning physically since the phase change material (paraffin) is an amorphous material, which has not a set melting point, but rather a range over which the material gradually softens into the liquid phase. Because the process is contained in an enclosure, free expansion is not allowed. Boussinesq approximation is therefore applied.

$$\rho = \rho_o \quad (3.3)$$

The continuity equation becomes

$$\nabla \cdot \mathbf{u} = 0 \quad (3.4)$$

Boussinesq approximation simplifies the density to be a constant except in the body force term of the momentum equation. The body force accounts for the buoyancy induced advection, where density change affects flow. The momentum is governed by the following equations in the radial and axial direction respectively.

$$\rho_o \frac{\partial \mathbf{u}}{\partial t} + \rho_o \mathbf{u} \cdot \nabla \mathbf{u} + \nabla p = \rho g - \mu \frac{\mathbf{u}}{K_u} \quad (3.5)$$

Density is a variable as a function of temperature in the body force term.

$$\rho = \rho_o \beta_T (T - T_{ref}) \quad (3.6)$$

In order to simulate the corresponding velocity in the partially melted and solid zone, a sink term is added to damp the momentum of fluid. K_p is the permeability constant that damps the velocity in the partially solid zone. K_u is equal to zero in solid zone and infinitely large in liquid zone. K_p is a function of liquid fraction ϕ_l [87].

$$K_u = \frac{\phi_l^3}{c_u(1 - \phi_l)^2} \quad (3.7)$$

Overall, the momentum equation for takes the following form:

$$\rho_o \frac{\partial \mathbf{u}}{\partial t} + \rho_o \mathbf{u} \cdot \nabla \mathbf{u} + \nabla p = \rho_o \beta_T (T - T_{ref}) g - \mu \mathbf{u} \frac{c_p(1 - \phi_l)^2}{\phi_l^3} \quad (3.8)$$

Energy in the liquid region is governed by the following equation. with the absence of source term, since viscous heating is negligible.

$$\frac{\partial}{\partial t}(\rho H) + \nabla(\rho u H) = \nabla \cdot (k \nabla T) \quad (3.9)$$

The enthalpy H is defined as the summation of sensible heat h and latent heat ΔH .

$$h = h_{ref} + \int_{T_{ref}}^T c_p dT \quad (3.10)$$

where c_p is the specific heat capacity

$$\Delta H = \phi_l L_m^f \quad (3.11)$$

where L_m^f is the latent heat of fusion.

Therefore, we only have to specify liquid fraction to apply the momentum and enthalpy equation to all three regions regardless of melting condition, and liquid fraction is defined as follows [87]. Governing equation for freezing is simpler than that of melting. Stefan boundary condition is applied at the melting surface. Because Biot number is very large, steady state approximation can be assumed.

$$q_s = \frac{\Delta T}{R_s} = \frac{(T_\infty - T_f)(4\pi r_i r_o k_s)}{r_o - r_i} \quad (3.12)$$

$$q_l = \frac{\Delta T}{R_l} = hA(T_f - T_i) = \frac{Nu \cdot k_l 4\pi r_i (T_f - T_i)}{2} \quad (3.13)$$

$$Nu = 2 + \frac{0.589 Ra^{1/4}}{[1 + (0.469/Pr)^{9/16}]^{4/9}} \quad (3.14)$$

3.2.3 Boundary conditions and Initial condition

Not only does the model need to satisfy the governing equations, it must also correctly implement the same initial and boundary conditions in experiment to yield valid results. The encapsulated sphere was submerged in a sink filled with water at 40°C. Even though the water temperature in the sink is held constant, there is still temperature on variations at the surface of the shell, as observed in the experimental measurements. The heat transfer mode between the shell and external water is best described as free convection. The average heat transfer coefficient is dependent on the temperature difference between the shell and free stream water. The external free convection is most important in determining the initial heat transfer rate, as internal convection dominates later on in the process. Therefore the heat transfer coefficient is estimated based on the initial temperature difference, based on the following correlation

$$Nu = 2 + \frac{0.589 Ra^{1/4}}{[1 + (0.469/Pr)^{9/16}]^{4/9}} \quad (3.15)$$

The shell also has a thermal resistance, estimated based on the thickness and the conductivity of Pyrex glass used in the experiment. The calculations show that external convection, wall resistance, internal convection

are all in the same order of magnitudes during at least one part of the melting process. Thus they all have to be considered in the simulation. Compared to the Dirichlet boundary condition used in previous studies, convective boundary conditions should have more accurate melting rate in the initial stage of the process.

Initial condition is also very important. The experiments studied separate cases where the whole sphere is subcooled to 1°C and 10°C below the melting point. The corresponding simulations should reflect the condition used in the experiment. The published simulation failed to compare numerical results to the correct experiment case. Therefore their simulation is very invalid. This study will focus on the 1°C subcooling case and initial condition will be set as such.

3.2.4 Computational Methods

In the published model [3], Power Law discretization scheme, a grid of 7636 triangular and quadrilateral cells, a timestep of 0.1s and 200 to 400 iterations per timestep were used. The computational methods were revised to be more efficient and accurate. In the new simulation, a structured grid with 18876 cells is used instead. Structured grid is chosen for better performance. Timestep is refined to 0.05s. It was found that 50 iterations were able to satisfy the convergence criterion, set at 10^{-6} in absolute error. QUICK scheme was the discretization scheme used. QUICK is a third-order upwind scheme that offers robustness and accuracy.

In order to validate the performance of the new methods, sensitivity analysis is performed for grid size, time step and the number of iterations per time step. In comparison cases, every subject is refined by a factor of 2. The simulation is allowed to run for 20 seconds of simulat time and relative error is calculated based on integral liquid fraction.

Subject	Grid	Timestep	Iteration	Scheme
Control	18876	0.05s	50	QUICK
Validation	45063	0.02s	100	Second Order Upwind
ERE <	10^{-3}	10^{-4}	10^{-6}	10^{-5}

Table 3.2: Numerical setup and validation

Sensitivity analyses proved that the number of iterations is the least important factor affecting the accuracy of simulation. Instead, timestep and mesh refinement is more useful allocations of computational power. Timesteps of 0.02s and 0.05s are further compared. The cumulative relative error for liquid fraction and total enthalpy is less than 10^{-3} after 4000 seconds of simulation time. Timestep independence is achieved with this level of accuracy. The choice between methods has very little influence on accuracy. Although Second-order upwind is less computationally demanding, the performance gain in the real world is minimal. Therefore QUICK scheme is chosen for its better stability.

Grid validation is conducted by refining the mesh while keeping all other parameters constant. A new structured mesh is also used instead of the original mesh. Grid study showed that the grid refinement had a noticeable effect on the results. The overall melting rate was seen to shorten using a grid that is automatically refined by halving the cell size. Structured grid was shown to extend this trend despite having fewer cells. Although it could not be said that we had achieved grid independence, the finer grid only showed a small error and exhibited consistent trend that approached the experimental results in literature. Therefore the CFD simulation was validated.

The numerical results to be analysed uses the setup in the following table:

3.2.5 Results and Discussion

Results from CFD have shown consistency with experimental data. Because of the corrections made to the model, the accuracy of the modeling is much improved. The comparison between CFD results and

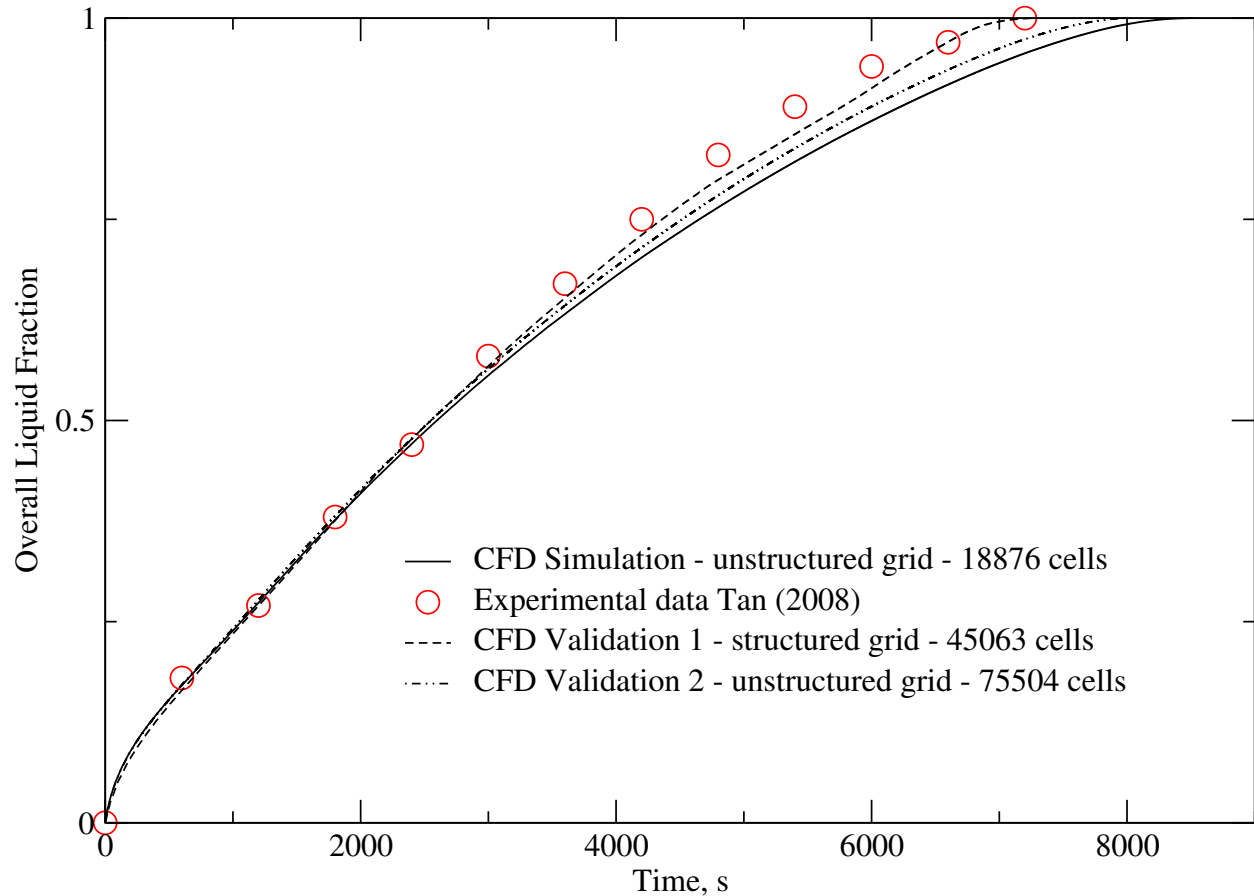


Figure 3.1: Grid study by the comparison of liquid fraction over time using refined mesh versus experimental results published in [2] [3]

experimental data are found in Fig. 3.1. Initially, the results are very consistent. The consistency was not only shown in overall liquid volume fraction, but also shown in the shape of the melting solid. The shape changes resembles actual snapshots of the melting solid. The similarity indicates that the simulation correctly captured the flow pattern in capsule.

At the beginning of the melting process where convective effect is small, melting happens in all directions almost uniformly. At this stage, external convection and shell conduction are the dominant heat resistance. Around the 30 min mark, the melting is transitioned to a stage dominated by internal convection. The melting front at this stage can be divided into 3 parts. At the upper part of the sphere, warm liquid accumulates. The high temperature gradient causes the upper interface to melt the fastest. At the lower part of the sphere, warm liquid also floats upward but hits the solid. Melting is not as fast because the liquid at the bottom is colder than at the top. The flow is cooled and sinks toward the bottom. The hot rising flow and cold sinking flow exchange intensively, creating chaotic liquid movement. The chaotic motion results in a rough and constantly changing shape. On the side, warm liquid flows steadily along the surface to reach the top and hardly penetrates the pores in the melting solid. The side melts slowest but has a smooth surface.

Despite the difference of melting rate at different parts of the interface, the shape of the solid remains large spherical until very close to the completion of the process, evident in the Figure 3.2. This observation allows us to directly convert the radius of solid to the interfacial area and solid fraction by using simple geometry relations. If the heat transfer coefficient for internal convection is known, we are able to reduce

Subject	Grid	Timestep	Iteration	Scheme
Final Setup	45063 cells	0.02s	50	QUICK

Table 3.3: Final numerical setup used for full simulation

the modeling of melting for two dimensional to zero dimensional, much expediting the computational time.

The most noticeable discrepancy between the simulation and Tan’s published experiment data is the shape of the solid near the end of melting. In part, it is because of the limitation of 2-D axisymmetric model that is capable of modeling 3-D chaotic flow below the solid. The other reason is that there exists a significant difference in conductivity between solid paraffin and liquid paraffin. Initially, the conductivity in different phases is assumed to be the same, which results the profile in the following figure. The results are falsified using undifferentiated conductivity, because the shape does not resemble the shape observed in [2]. The difference in shape between Figure 3.5 and Figure 3.2 is especially obvious near the end. It is not fully clear why solid conductivity causes the shape to differ, but it is likely because the high conductivity in solid causes the heat from the rising current to penetrate the solid quickly and results in well distributed melting rate. Although the overall melting rate is largely unaffected, it should be noted the correct modeling must accurate information.

Heat transfer in solidification is shown to be dominated by conduction in the solid. When a melted sphere is cooled from outside, solidification begins to form on the inner surface of the shell. Solid transfers energy much slower than liquid due to the lack of convection. Heat transfer rate is significantly slowed as the thermal resistance continues to increase between the heat source, melting front, and the heat destination, free stream. As a result, discharging the heat storage unit is much slower process than charging. While the charging cycle takes around two hours to complete, the discharging cycle takes over 7 hours using equal temperature difference. The difference in heat transfer rate must be accounted for in the design of the TES device. The methods to achieve symmetric charging/discharging time includes choosing material with melting point closer to the hot stream temperature and farther from the cold stream temperature, bringing closer the overall heat transfer rate and charging/discharging time.

3.2.6 Figures

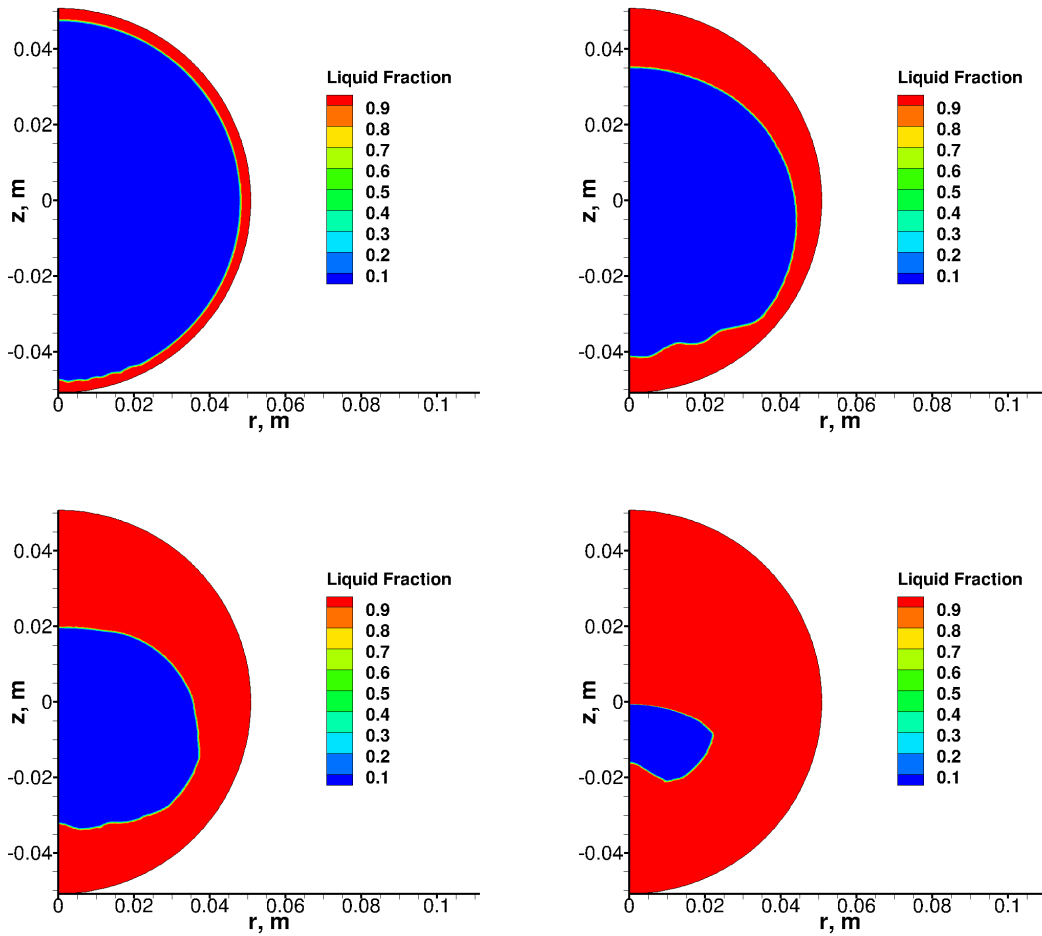


Figure 3.2: Melting: liquid fraction contour from CFD

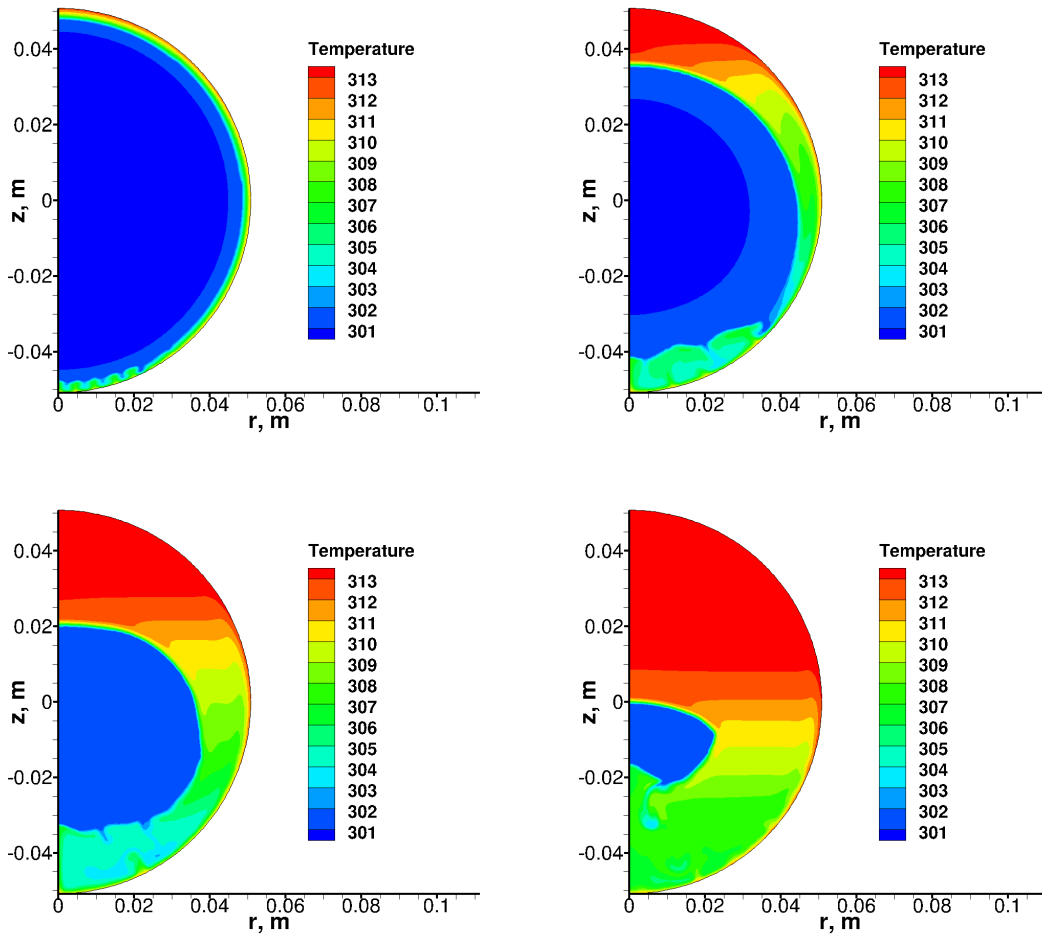


Figure 3.3: Melting: temperature contour from CFD

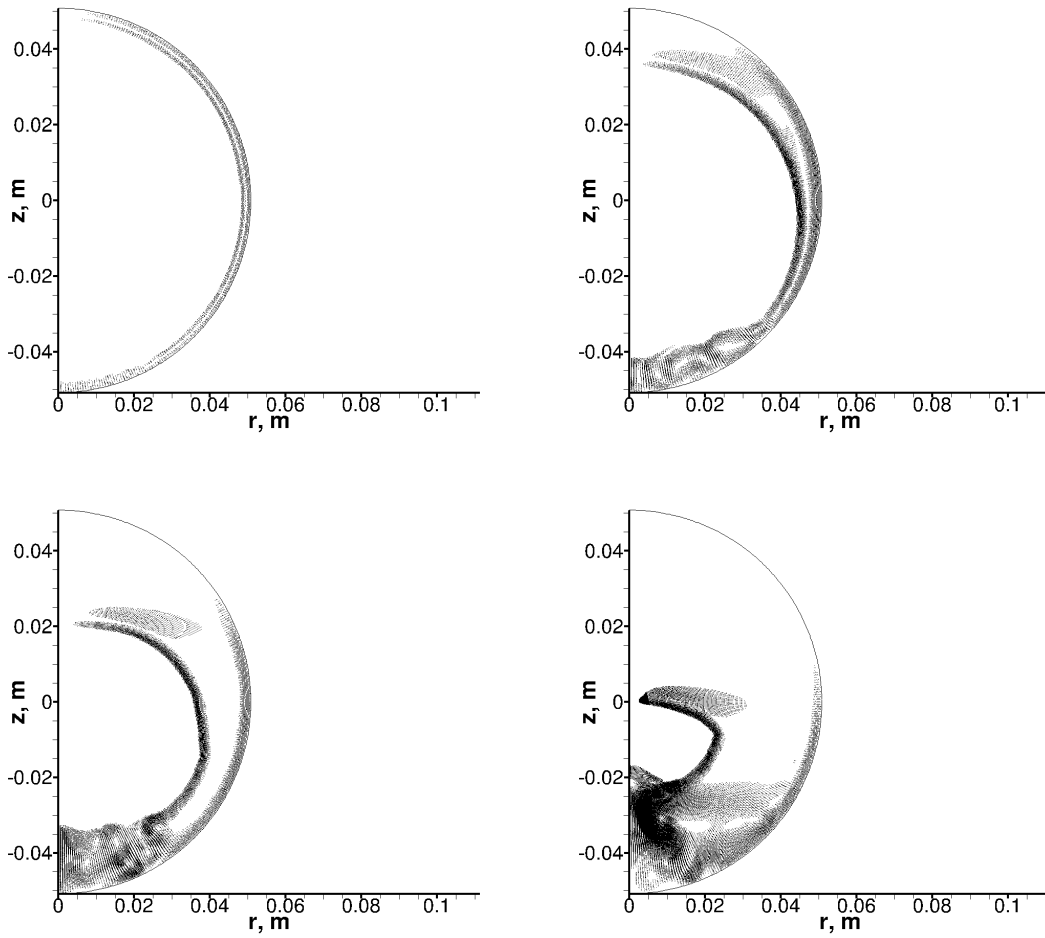


Figure 3.4: Melting: stream velocity contour from CFD

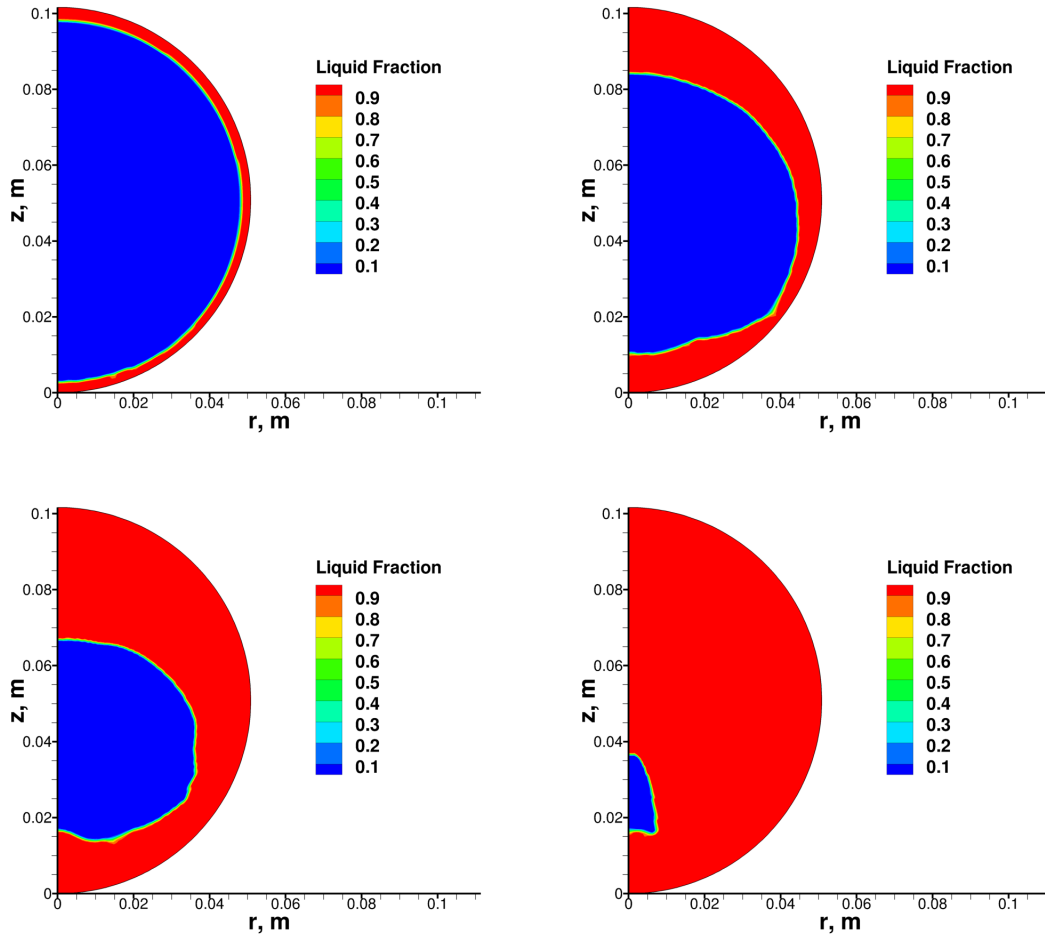


Figure 3.5: Melting: liquid fraction contour from CFD

3.3 Semi-Empirical Model Formulation

Although CFD shows good accuracy for the melting and freezing of PCM, it is computationally costly. The simulation for melting took over two days and the simulation for freezing took over one week to complete. For a system that consists of thousands of particles, such simulations would not be feasible.

In order to reduce the computational time, a semi-empirical model is proposed to simplify the 2-D simulation, yet to retain the important physical characteristics. In both solidification and melting, heat transfer is initially dominated by external convection. As the layer of solidified or melted layer thickens, internal thermal resistance becomes the limiting step. Thus solidification is simple because conduction in solid obeys Fourier's Law. Heat transfer in melting is mostly dependent on the effects of convection.

Convection in melting is a complicated phenomenon. Although the solid remains closely spherical during melting, the correlation for concentric spheres do not apply here. One of the reason is that the center of the solid sphere moves down from origin as the top melts faster than the bottom. The other is the that the melting interface is different from a solid-liquid interface, especially for paraffin, which is an organic mixture. The boundary layer at the melting interface is unique, and has much more influence on the heat transfer coefficient than the outer liquid-shell interface. Therefore, the successful modeling of melting must include a correlation specific for the convective heat transfer inside capsule of constrained melting sphere.

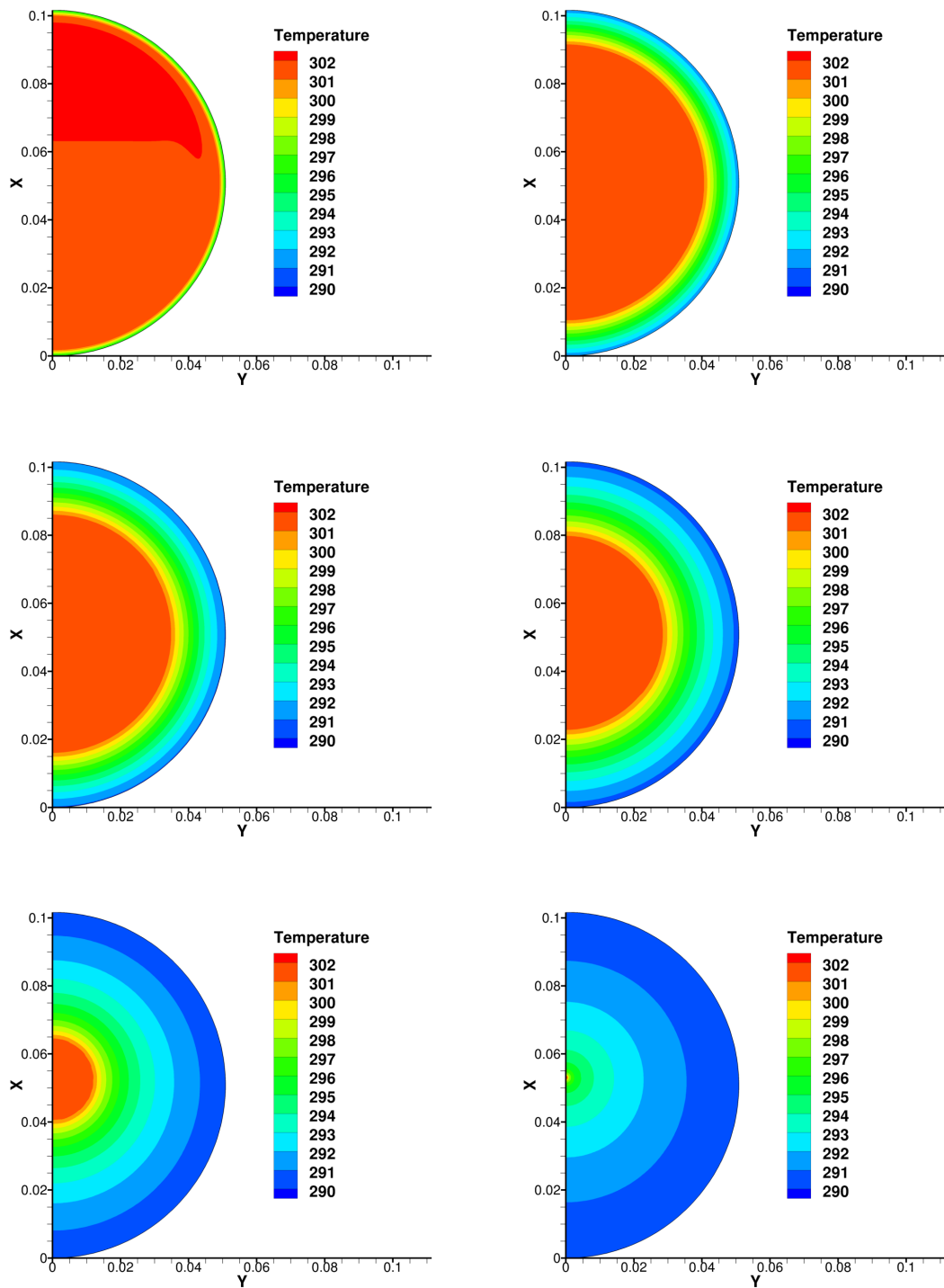


Figure 3.6: Solidification: liquid fraction contour from CFD

3.3.1 Melting

The melting of PCM happens during the charging cycle of the heat storage system. The melting process is treated as a Stefan boundary problem. The current design features a solid sphere that is constrained in position so it would not sink or float due to density changes. Throughout the melting process, the solid is assumed to remain in spherical shape. The assumption is valid for melting up to 90% liquid fraction. If a correlation can accurately capture the heat transfer coefficient for spherical shape, the process can be simplified to zero dimensional.

Depending on the nature of the system, the sensible heat may or may not be negligible, but it is generally much smaller than latent heat. Instead of solving complicated heat equations, simple equations are used to approximate sensible heat. Approximations for average solid and liquid temperature are applied with their respective equations. The solid temperature approximation is an ordinary differential equation based on an artificial radius.

- **Energy Balance for the solid phase temperature**

The energy balance equation for solid temperature is taken from journal article by Hemant Bansal et al. [88]. The approximation is verified in experiment.

r_{sol} is the radius of solid phase PCM, r_t is artificial radius corresponding to T_{sol} location, which is equal to $0.5^{1/3}r_{sol}$

The liquid temperature is neglected because the external liquid temperature should be close to the melting point of the PCM. The sensible heat change in the melted material is insignificant.

- **Solid-Liquid Interface: Stefan condition**

The latent heat of fusion determines the rate of melting.

$$q_{melting} = \rho_{sol} L_m^f \frac{4}{3}\pi \frac{dr_{sol}^3}{dt} \quad (3.16)$$

$$q_{sol} = \frac{4\pi k_{sol} (T_m - T_{sol}) r_t r_{sol}}{r_{sol} - r_t} \quad (3.17)$$

where T_{sol} is the average temperature of the PCM solid corresponding to the temperature at the distance r_t ($= 0.5^{1/3}r_{sol}$) from the center.

The overall heat rates from the liquid side can be formulated using classical heat transfer theory:

$$q_{liq} = 4\pi r_{sol}^2 h_{SL} (T_{sin} - T_m) \quad (3.18)$$

where h_{SL} is the internal convective heat transfer coefficient that needs to be determined from experimental and numerical data. The equality of heat transfer at Stefan boundary is.

$$q_{melting} = q_{liq} + q_{sol} \quad (3.19)$$

- **Internal surface of the outer sphere**, we neglect heat storage inside the shell

$$4\pi r_{sol}^2 h_{SL} (T_m - T_{sin}) = \frac{4\pi k_s (T_{sin} - T_{sout}) r_{sin} r_{sout}}{r_{sout} - r_{sin}} \quad (3.20)$$

- **External surface of the outer sphere**

$$\frac{4\pi k_s (T_{sin} - T_{sout}) r_{sin} r_{sout}}{r_{sout} - r_{sin}} = 4\pi r_{sout}^2 (h_{\infty} (T_{sout} - T_{\infty}) + \varepsilon\sigma (T_{sout}^4 - T_{\infty}^4)) \quad (3.21)$$

$r_{sout} - r_{sin}$ is the thickness of the shell.

3.3.2 Internal convection

The average internal Nusselt number correlation can be separated into two parts, the contribution by conduction and the contribution by convection. If we presume melting to be symmetric and the solid remains spherical, the heat transfer mode for melting inside a spherical shell is analogous to that between concentric spheres. A number of different setup with concentric spheres are simulated in Fluent. We find that the average Nusselt number is only a function of Gr , Pr and r_i/r_o . In other words, similar solution applies to the problem at all times and all length scales. Since Pr is a material property that remains constant and $Ra = GrPr$, we can simplify the equation for a single-material system.

$$\overline{Nu} = f(Ra, r_i/r_o) \quad (3.22)$$

The equation for conduction Nusselt number is derived analytically and only dependent on r_i/r_o .

$$\overline{Nu}_{cond} = \frac{2}{1 - r_i/r_o} \quad (3.23)$$

We propose that the convection Nusselt number is a ratio of the Churchill equation for a sphere in the a fluid with constant temperature at infinite distance. Since the Nusselt number in infinite fluid is already a function of Ra , that ratio should be only dependent on r_i/r_o .

$$\overline{Nu}_{conv} = f(r_i/r_o) \frac{0.589Ra^{1/4}}{(1 + (0.469/Pr)^{9/16})^{4/9}} \quad (3.24)$$

In the correlation for free convection of sphere submerged in infinite fluid, the contribution by conduction and convection are added together directly.

$$\overline{Nu} = \overline{Nu}_{conv} + \overline{Nu}_{cond} \quad (3.25)$$

We know that the overall heat transfer rate is contributed by both conduction and convection. The same simple addition of the two terms gives a reasonable solution, but it is not the most accurate form of correlation we can have. However, it is found that instead of adding Nusselt numbers of conduction and convection, the co-relation can achieve better accuracy if the terms in the relation are all raised to the power of n . This is a sound modification because in case either conduction or convection dominates heat transfer, the equation approaches the correct limits.

$$\overline{Nu}^n = \overline{Nu}_{conv}^n + \overline{Nu}_{cond}^n \quad (3.26)$$

With the new expression, we can now find the shape function $f(r_i/r_o)$. By changing the choice of n , the accuracy can be improved. However, as the shape factor $f(r_i/r_o)$ has no set form, a complicated correlation lacking physical meaning is trivial. Instead, $n = 1$ is settled on and the simplest form is chosen for $f(r_i/r_o)$. The simulation results from a near-limiting case actually shows that Nu is very close to the Churchill's original equation. Therefore the closest reasonable approximation of average Nusselt number for melting sphere is :

$$\overline{Nu} = \left((1.2 - r_i/r_o) \frac{0.589Ra^{1/4}}{(1 + (0.469/Pr)^{9/16})^{4/9}} \right) + \left(\frac{2}{1 - r_i/r_o} \right) \quad (3.27)$$

3.3.3 Solidification

Solidification is much simpler to model because convection only exists inside the solid-liquid interface. Because the majority of heat is released from the solidification and flows outward, the heat transfer rate is no longer significantly affected by convection. Consequently, governing equation for freezing is simpler than that of melting. Stefan boundary condition is applied at the melting surface.

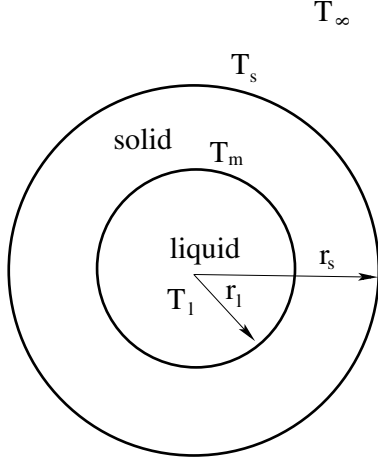


Figure 3.7: Principal scheme of a sphere freezing

- Stefan number

$$Ste = \frac{c_p(T_f - T_o)}{L_m^f} = 0.011 \ll 1 \quad (3.28)$$

Stefan number is the ratio of sensible heat to latent heat in a system. If the ratio of sensible heat is much smaller than latent heat, the sensible heat storage can be neglected. Therefore we can approximate quasi-steady temperature profile for the solid and determine heat transfer rate using Fourier's Law.

$$\rho L_m^f \frac{dV_s}{dt} = q_l - q_s \quad (3.29)$$

$$V_s = 4/3\pi(r_o^3 - r_l^3) \quad (3.30)$$

$$\frac{dV_s}{dt} = -4\pi r_l^2 \frac{dr_l}{dt} \quad (3.31)$$

- Solid side:

$$q_s = 4\pi k_s \frac{(T_m - T_s) r_l r_s}{r_s - r_l} \quad (3.32)$$

- Liquid side (no convection):

$$q_l = 4\pi k_l \frac{(T_l - T_m) r_t r_l}{r_l - r_t} \quad (3.33)$$

where $r_t = 0.5^{1/3} r_l$

- Liquid temperature:

$$\rho c_p \frac{dT_l}{dt} = 4\pi k_l \frac{(T_l - T_m) r_t r_l}{r_l - r_t} \quad (3.34)$$

- Equation for T_s :

$$A_s h_s (T_s - T_\infty) + A_s \sigma \varepsilon (T_s^4 - T_\infty^4) = 4\pi k_s \frac{(T_m - T_s) r_l r_s}{r_s - r_l} \quad (3.35)$$

h_s can be calculated using Ergun equation for the fixed beds.

3.3.4 Results and Discussion

The cumulative melting fraction was plotted in Fig. 3.8. The results also compared favourably with the data from experiments and 2-D numerical simulation. The semi-empirical model predicted the melting or freezing time with good accuracy. In fact, the semi-empirical model showed even greater consistency with experimental data than CFD simulation. The results should not be interpreted as if the semi empirical equation is more accurate. This underprediction is probably due to the laminar flow regime used in CFD simulation. The discrepancy in shape makes it evident that the flow regime was not sufficient when remaining solid is less than 20%. While the CFD simulation might lack the complexity to account for all flow regimes near the end, the semi-empirical model did not provide any flow detail at all. A factor that might contribute to the improvement is that the semi-empirical model neglects sensible heat storage in liquid portion, which was significant for melting only at the later stage. The CFD simulation underpredicted melting rate at this stage. The sensible heat that was assumed to be absorbed as latent heat could account for much of the extra melting in the semi-empirical model. The improvement resulting from the semi-empirical model over CFD was not completely incidental. Although the correlation for convective heat transfer is derived from curvefitting, it encompasses analytical reasoning behind its development. In terms of overall accuracy, the semi-empirical model was at least a valid simplification of CFD.

The liquid fraction during solidification was plotted in Fig. 3.8. In the CFD simulation conducted in this work and published experimental data, convection was found to not play any significant role and the solid layer formed concentrically [77, 81, 79]. Therefore in the semi-empirical model convection was omitted along with the sensible heat in the liquid portion. The results showed very good consistency. The relative errors observed were less than 1%, attributed to the numerical truncation error and the small unaccounted portion of sensible heat.

The results from the semi-empirical model showed that charging/discharging time is a function of temperature difference and particle diameter, as seen in 3.10. The log-log plot of time shows a linear decrease with temperature and increase with diameter. The relation could be expressed in the following equation. It should be noted that the coefficients a and b are not constant when conditions change. A change in ΔT will result in change in b and a change in d will result in a change in a and a change in either can result in change in c .

$$\log t_{dc} = a \log \Delta T + b \log d + c \quad (3.36)$$

The temperature difference, melting or solidification time have the same slope on a log-log scale graph but different intercepts. The temperature difference should be about 3 times larger for solidification than for melting to achieve similar time for a sphere that is around 10cm.

As the particle diameter decreases, the effect of convection becomes less significant, which results in similar time between charging and discharging cycle. The times become practically equal when the diameters are around 2cm. If the diameter continues to decrease, solidification can become even faster than melting because of the higher thermal conductivity of the solid phase.

The semi empirical model proves to be an effective tool to calculate phase change and thermal energy storage inside an encapsulated spherical PCM particles. The correlation for convective heat transfer is calculated using Eq. 3.27, which is the dominant heat transfer mode for the majority of the thermal charging cycle. The solidification does not depend on internal convection. The dominant heat transfer mode during the discharging cycle is the heat transfer through the solidified layer outside the solid-liquid interface, show in Eq. 3.29.

3.3.5 Figures

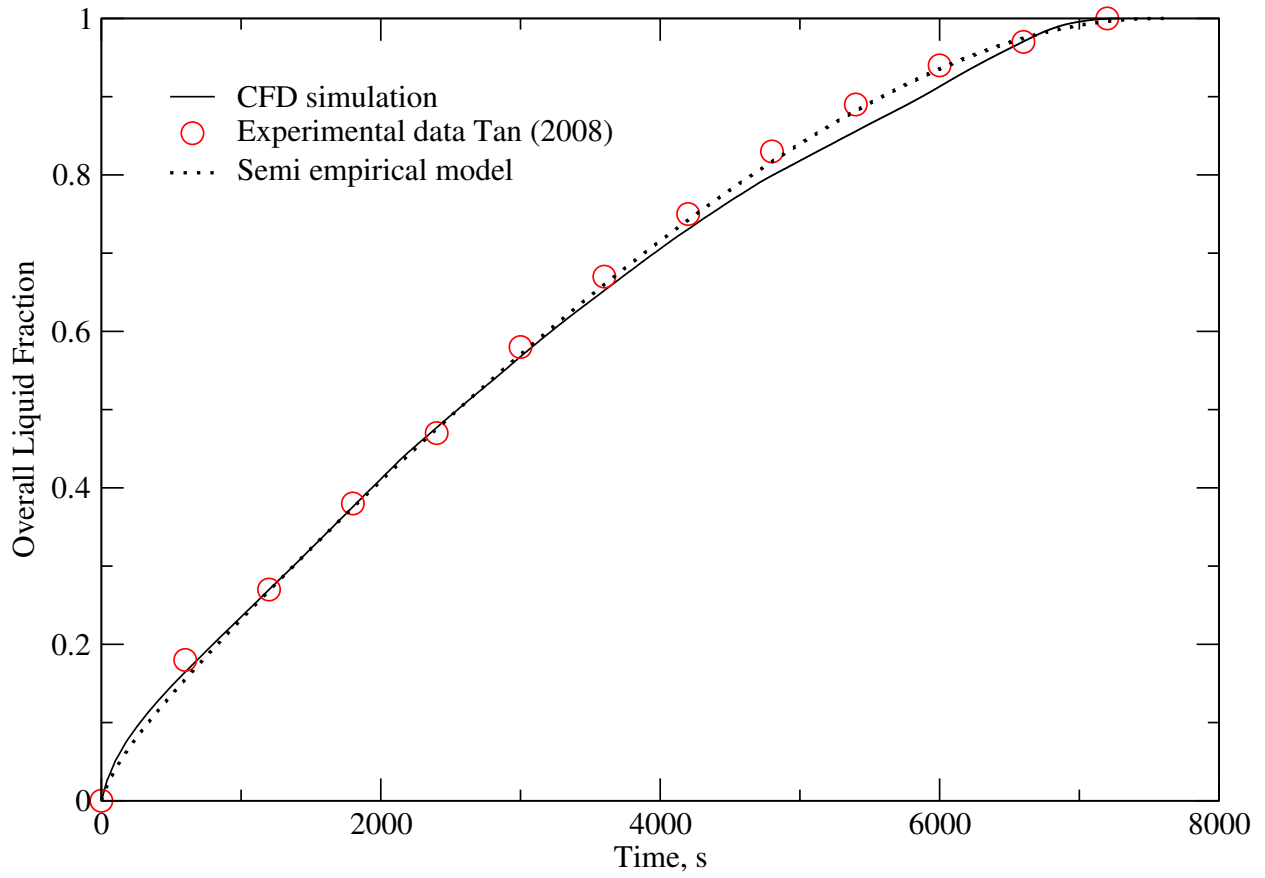


Figure 3.8: Comparison of liquid fraction for melting with CFD and Tan's experimental [2] results

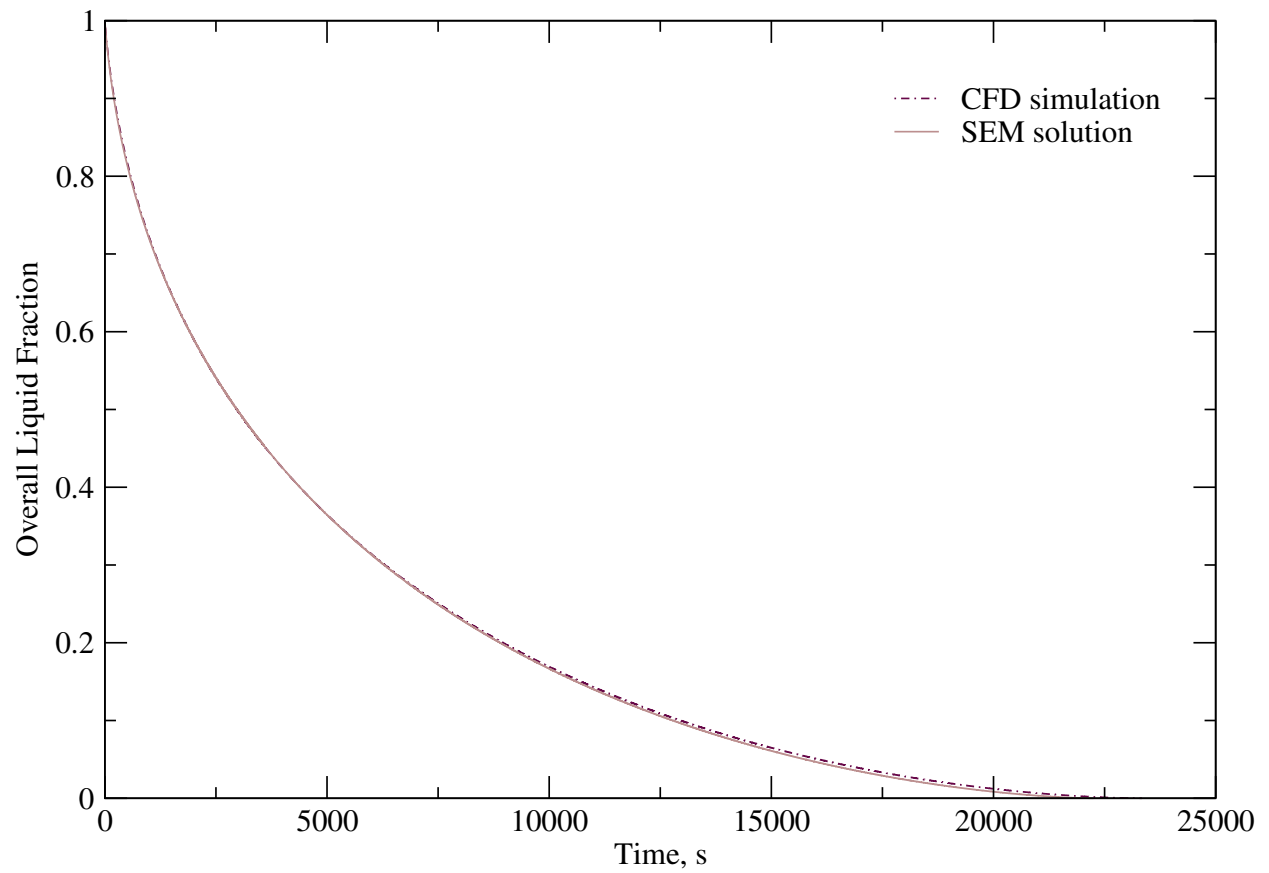


Figure 3.9: Comparison of liquid fraction for solidification with empirical and CFD results

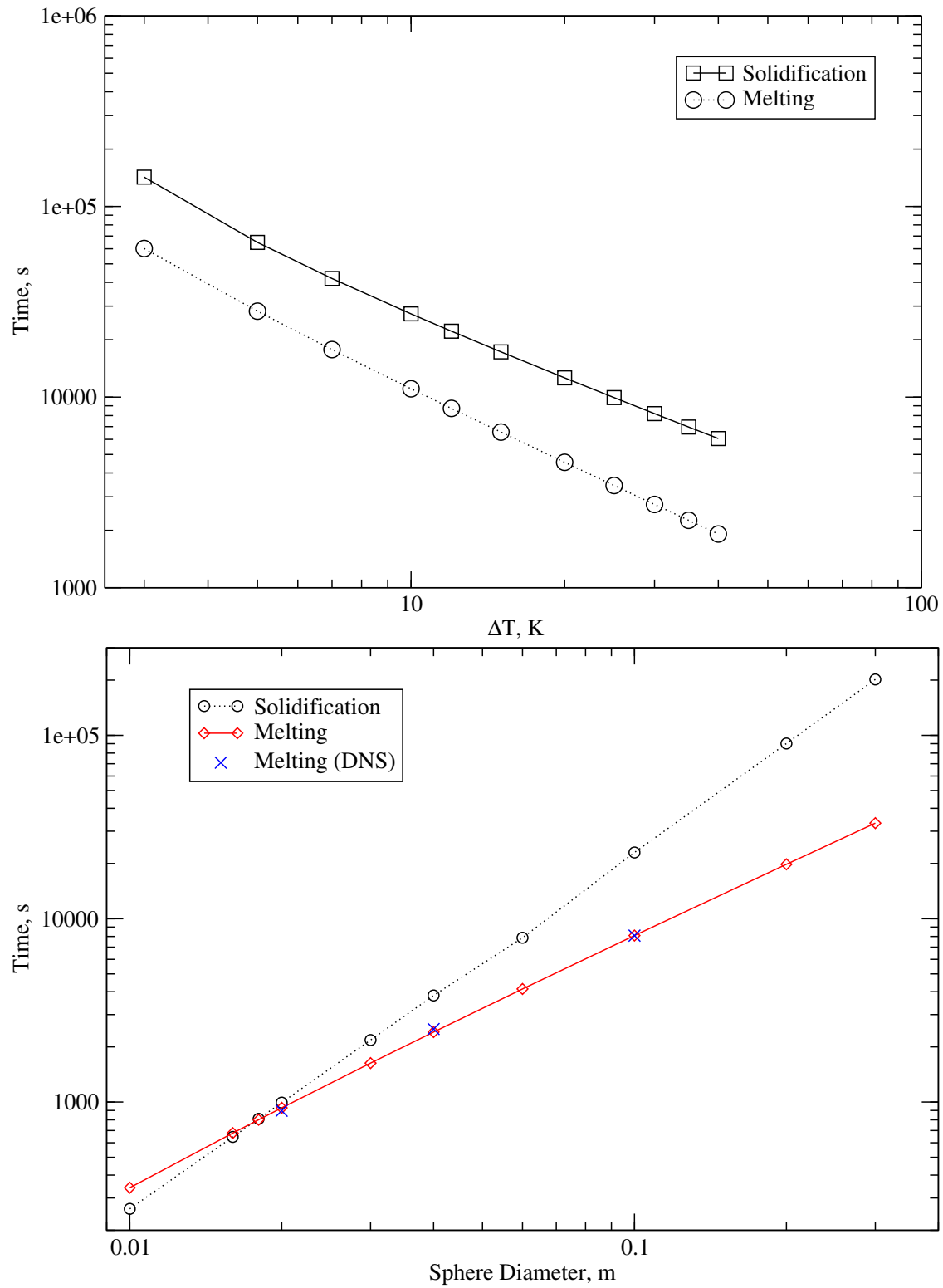


Figure 3.10: Change of solidification and melting time due to different ΔT at $d=0.1$ m and different d for $\Delta T=10$ K

Chapter 4

Numerical Studies of Fixed-bed Thermal Energy Storage System Using Encapsulated Phase Change Material

4.1 Introduction

Population growth and economic development are constantly driving the global energy consumption up. To cope with fossil fuel depletion and environmental impacts of carbon dioxide release, renewable energy is growing rapidly driven by the demand to supplement tradition energy sources. With the widespread arrival of renewable energy applications, energy storage is not only a promising solution, but almost certainly the necessary solution for the intermittency anticipated from renewable sources. Thermal energy storage (TES) is an important part of energy storage, as thermal energy is one of the largest demand for mankind[89]. Thermal energy can be harnessed not only from solar power, but also from waste energy generated in various industrial processes. TES systems can be used in many applications including industrial manufacturing and chemical reactions, but the most important application will be the heating and cooling of buildings, which use more than half the total energy consumption by buildings[90]. TES can be classified as sensible heat storage, latent heat storage, and thermochemical heat storage. Most thermochemical processes degrade over several charging and discharging cycles, making them impractical for long-term maintenance free applications[91].

Sensible heat storage is the most widely used application in high temperature concentrated solar power plants[90]. The most common TES technology in concentrated solar power plants are molten salt storage. Molten salt, mostly commonly nitrates, has high volumetric heat capacity. However, the technology of molten salt requires high operating temperature, as nitrate salts typically melt over 300 °C. Molten salts are stored in tanks to prevent heat loss. Efficiency is better when the system is upscaled through the minimization of heat loss. Another limitation is its corrosive effect on construction material[92]. The use of molten salt is also an expensive solution, as it requires a large amount of nitrates for each system, acting as both heat transfer fluid(HTF) and heat storage material.

Because of the drawbacks of the high temperature sensible heat applications, low temperature heat storage systems have garnered growing interest. One of the alternatives is to fixed bed heat storage system where the solid heat storage material are packed in a bed and a heat transfer medium is used to convey heat from the source to the solid heat storage material through direct contact. The fixed bed TES system allows for much lower operating temperature by separating the HTF and the heat storage material. The lower temperature means better efficiency, lower cost, and wider applications. However, since the HTF and heat storage medium are separate, there is additional resistance and delay between the source and the storage, limiting the power of heat storage to the rate of heat transfer. Heat exchanger is a possible solution where

the HTF does not directly contact the particles. Despite shown in experiments to have excellent overall heat transfer coefficients [93], heat exchangers do not have enough surface area compared to a fixed bed. Therefore a significant temperature difference is still needed in heat exchanger. The heat exchanger is more suitable for applications of sensible heat storage [94], or a sensible-latent hybrid system where sensible heat is the principal heat storage mechanism.

The advantage of using fixed beds where HTF directly contact heat storage medium is its large surface area. The surface area allow good heat rate despite operating with low temperature potential. Good heat rate enables us to design practical systems where the concentration of solar power is far less demanding with the use of latent heat storage technologies. Latent heat storage uses phase change of material to store heat. Although currently still in a prototypical stage of development, the latent heat storage technologies are attractive because they offer superior energy density and constant temperature of operation when storing or giving off heat[94]. The thermostatic behavior of latent heat storage system makes it ideal for applications in buildings for heating and cooling purposes. The fixed bed latent heat storage unit is a fixed bed consisting of many encapsulated phase change material(PCM) used for heat storage. Encapsulation of PCM is used to increase heat transfer and lifespan of the PCM[95]. PCM capsules in a packed bed are widely used for its simple design, durability. Low heat transfer rate is still the main drawback for using PCM as a strategy for cooling and heating applications[96]. However the drawbacks of encapsulated PCM particles include high manufacturing cost and high response time and low space efficiency.

Since encapsulation is an expensive process, there have been many attempts to develop microencapsulated PCM. Stark[97] investigated the encapsulation of PCM in polymer film. Royon et al.[98] developed a network of polymer that can be used without support or coating. However, these solutions were or too costly to be feasible. Rady[99] conducted experiments on highly porous granules for heat storage with the pores in granular material filled with PCM. Granular PCM reduce particles size in the fixed bed to increase heat transfer. Granules require an envelope to entrap the melted PCM which negatively affected the heat transfer rate. Still, the granules are too delicate to be used with direct contact with the HTF.

Another area of interest is to improve the conductivity of PCM through material science. In recent years, there have been numerous attempts at increasing the effective thermal conductivity of the PCMs. One of the most promising solutions is to add in nanoparticles with high conductivity[100]. Heat will be conducted much more quickly through the nanoparticles. Phase change and convection can be improved through the usage of nanoparticles. The nanoparticles are effective, but they lose their effectiveness over phase change cycles due to segregation and agglomeration.

In this chapter, a new design is proposed to combat these issues. The new design of fixed bed contains not only encapsulated PCM, but also metal particles mixed in them. The advantage of metal particles is that they conduct and absorb heat quickly, which help the overall heat transfer rate and response time. The metal selected is aluminum, which is a great conductor, a relatively good heat capacitor, corrosion resistant, lightweight, and reasonably cheap. Water is used as the medium that carries thermal energy from the heat source to the PCM. Water has high specific heat capacity and high thermal conductivity.

The amount of metal particles in the system was to be determined by cross comparison of cases under the same condition best efficiency. The simulations were conducted for two sets of comparisons. One compares the performance of heat storage units with different volume fractions of aluminum particles, but identical apparent size, while the other compares the performance of heat storage units with different volume fractions of aluminum particles but identical number of encapsulated PCM particles. The common operating conditions of the simulations is shown in Tab. 4.1.

There are many models available for heat transfer in the fixed bed heat storage. The Schumann model is a one-dimensional two-phase model originally developed by Schumann[101]. The original Schumann model uses a few assumptions:

1. Homogeneous temperature inside the solids
2. Flow in homogeneous porous medium
3. Temperature and velocity variable in 1D
4. Adiabatic storage with insulated walls

Parameter	Symbol	Value	Unit
Melting point	T_m	303	K
HTF(Water) inlet temperature	T_{in}	323	K
Density of Water	ρ_f	772	kg/m ³
Dynamic viscosity of water	μ	$0.798 * 10^{-3}$	Pa s
Diameter of fixed bed	D_b	0.2	m
Volumetric flowrate	\dot{V}	10^{-4}	m ³ /s
Radius of PCM particle	r_{pcm}	2	cm
Radius of Al particle	r_{Al}	1	cm
Density of PCM	ρ	772	kg/m ³
Latent heat of fusion	L_m^f	243500	J/kg
Specific heat capacity of PCM	c_p	2330	J/kg K
Thermal conductivity of PCM liquid	k_{pcm}	0.1505	J/m·K
Kinematic viscosity of PCM liquid	ν	10^{-5}	m ² /s
Thermal expansion coefficient	β	0.00091	
Thermal conductivity of PCM solid	k_s	0.1505	J/m·K

Table 4.1: List of operating parameters using in simulations

5. Negligible conduction or radiation compared to convection

More advanced models, such as perturbation model, two-dimensional three-phase model, intraparticle conduction model are all developed in reference from the Schumann model by eliminating assumptions. In the published literature for sensible heat storage, the intraparticle model assumes concentric temperature profile inside solids[102]. With PCM capsules, the intraparticle heat transfer is not simple conduction during melting, as seen in the chapter prior to this. To account for the free convection of PCM in the capsule, effective conductivity is often used[103, 104]. It should be noted that the internal free convection is not so important the capsule size is small or the external forced convection is weak. In literature, many researchers claim that free convection is unimportant for heat transfer during charging[105, 106] for systems with low Reynolds number. However, there must be two conditions satisfied for this statement to be true. Firstly, the solid must be in contact with the capsule wall. Secondly, the HTF temperature must not be significantly changed due to heat loss in the fixed bed. If the solid PCM is fixed in position by matrix in the capsule, free convection will play a larger role between the phase-changing boundary and the HTF. If free convection is an important determining factor for the heat transfer rate, the effective conductivity is not a sufficiently accurate method to model free convection. Therefore the semi-empirical intraparticle convective correlation developed will be used in this chapter to model the heat storage and release of the fixed bed.

4.2 Numerical Model Formulation

Three thermal resistances determine the rate of heat transfer in fixed bed heat storage unit. The first is the thermal resistance between heat transfer medium and the particle surface. The second is the thermal resistance between particle surface and phase-changing interface. The third is the thermal resistance between particles.

The heat transfer between heat transfer medium and the particle surface follows of a convective correlation for heat transfer in a fixed bed. The Reynolds number of the fixed bed is based on the following equation.

$$Re = \frac{\rho_f U_s D}{\mu} \quad (4.1)$$

where D is the diameter of the particles, and U_s is the superficial velocity.

Because there are two sizes of particles, the Reynolds numbers for PCM and Al particles are different.

$$Re_{Al} = \frac{2r_{Al}\rho_f U_s}{\mu(1 - \varepsilon)} \quad (4.2)$$

$$Re_{PCM} = \frac{2r_{PCM}\rho_f U_s}{\mu(1-\varepsilon)} \quad (4.3)$$

Gunn correlation is used to calculate heat transfer coefficient.

$$Nu = (7 - 10\varepsilon + 5\varepsilon^2)(1 + 0.7Re^{0.2}Pr^{1/3}) + (1.33 - 2.4\varepsilon + 1.2\varepsilon^2) \times Re^{0.2}Pr^{1/3}; \quad (4.4)$$

In order to simplify the equations, a few assumptions have been made.

- The thermal capacitance in the particle shell of a PCM particle is neglected.
- The temperature is uniform within an aluminum particle.
- Fixed bed wall is insulated.

The first assumption is validated because the heat stored in the stainless steel shell is only 0.1% of the total thermal storage in the PCM particles. The second assumption is validated by Biot number of the particles using Eq. 4.5. $Bi = 0.01$.

$$Bi_{Al} = \frac{hL_c}{k} = \frac{hr_{Al}}{3k} \quad (4.5)$$

4.2.1 Heat Balance for the charging cycle

The temperature calculations are based on the heat balance at the melting interface. Because of the non-linearity of the interfacial equation, it is difficult to solve conduction problems. The interface moves slowly and the temperature profile at each instant is close to that of a steady state. We use quasi-steady approximation for temperature profile in the solid. Quasi-steady approximation is justified by the Stefan number.

$$Ste = \frac{c_p(T_m - T_{in})}{L_m^f} \quad (4.6)$$

The Stefan number is about 0.1 for the current analysis. Because the Stefan number is small, quasi-steady heat transfer profile is used. The heat balance at the melting interface is

$$q_m = q_l - q_s \quad (4.7)$$

Because the initial temperature of the solid is close to the melting point of the PCM, the heat from the solid side is negligible. The heat from the liquid side is calculated from total convective heat transfer, subtracting the amount of sensible heat stored in the liquid.

$$q_l = 4\pi r_i^2 \bar{h}(T_s - T_m) \quad (4.8)$$

$$q_m = m_p \Delta h_m \frac{d\phi_l}{dt} \quad (4.9)$$

The energy storage in the PCM particle has two parts, sensible heat and latent heat. Due to the presence of convection, the temperature profile of the liquid phase is of irregular shape. Therefore, a simple approximation is used to calculate the average temperature of the liquid phase.

$$T_p = T_s \phi_l + T_m(1 - \phi_l) \quad (4.10)$$

As for the convective coefficient of melted PCM, recall the submodel from the previous chapter,

$$\bar{h} = \left(\frac{1}{1 - r_i/r_o} + (1.2 - r_i/r_o) \frac{0.589Ra^{1/4}}{(1 + (0.469/Pr)^{9/16})^{4/9}} \right) \frac{k}{2r_i} \quad (4.11)$$

where $Ra = 8 \frac{g\beta}{\nu\alpha} (T_s - T_m) r_i^3$
Also since $r_i = (1 - \phi_l)^{1/3} r_o$

Expressed in terms of liquid fraction ϕ_l :

$$\bar{h} = \frac{k}{(1 - \phi_l)^{1/3} r_o} \cdot \left(\frac{2}{1 - (1 - \phi_l)^{1/3}} + (1.2 - (1 - \phi_l)^{1/3}) \frac{0.589(8 \frac{g\beta}{\nu\alpha} (T_s - T_m))^{1/4} ((1 - \phi_l)^{1/4} r_o^{3/4})}{(1 + (0.469/Pr)^{9/16})^{4/9}} \right) \quad (4.12)$$

The heat transfer rate is :

$$q_l = 4\pi k (T_s - T_m) r_o (1 - \phi_l)^{1/3} \cdot \left[\left(\frac{1}{1 - (1 - \phi_l)^{1/3}} + (1.2 - (1 - \phi_l)^{1/3}) \frac{0.589(8 \frac{g\beta}{\nu\alpha} T (T_s - T_m))^{1/4} ((1 - \phi_l)^{1/4} r_o^{3/4})}{(1 + (0.469/Pr)^{9/16})^{4/9}} \right)^{-1} + R_{wall} \right]^{-1} \quad (4.13)$$

Equating right sides of equations 4.9 and 4.13, we obtain the equation used to solve for the liquid fraction

$$m_p \Delta h_m \frac{d(1 - \phi_l)}{dt} = 4\pi k (T_s - T_m) r_o (1 - \phi_l)^{1/3} \cdot \left[\left(\frac{1}{1 - (1 - \phi_l)^{1/3}} + (1.2 - (1 - \phi_l)^{1/3}) \frac{0.589(8 \frac{g\beta}{\nu\alpha} T (T_s - T_m))^{1/4} ((1 - \phi_l)^{1/4} r_o^{3/4})}{(1 + (0.469/Pr)^{9/16})^{4/9}} \right)^{-1} + R_{wall} \right]^{-1} \quad (4.14)$$

The surface temperature of the particle T_s is also unknown. The heat balance at the outer surface of the PCM particle is used to solve.

$$q_l + m_p c_p \phi_l \frac{dT_p^{pcm}}{dt} = \sum_{i=1}^n \frac{(T_{nbi} - T_s^{pcm})}{R_{th}} + \left(\frac{1}{h_{pg} \cdot A_p} + R_{wall} \right) (T_w - T_s^{pcm}) \quad (4.15)$$

Substituting Eq. 4.10 into Eq. 4.15,

$$q_l + m_p c_p \phi_l^2 \frac{dT_s^{pcm}}{dt} = \sum_{i=1}^n \frac{(T_{nbi} - T_s^{pcm})}{R_{th}} + \left(\frac{1}{h_{pg} \cdot A_p} + R_{wall} \right) (T_w - T_s^{pcm}) \quad (4.16)$$

Water temperature is one-dimensional variable discretized along the direction of the flow.

$$(T_{w,n+1} - T_{w,n}) \cdot C_w \dot{m} + \sum_{i=1}^n h A_p (T_w - T_s) + m C_w \frac{dT_w}{dt} = 0 \quad (4.17)$$

The Alu particle has high conductivity and small radius. Lumped capacitance method is used, $T_p^{al} = T_s^{al}$:

$$m_p c_p \frac{dT_p^{al}}{dt} = \sum_{i=1}^n \frac{(T_{nbi} - T_p^{al})}{R_{th}} + h_{pg} \cdot A_p (T_w - T_p^{al}) \quad (4.18)$$

To solve the system of ODEs, implicit Euler method is used to approximated derivatives. We can see the equations 4.15, 4.17 and 4.18 are all linear ordinary differential equations if the variables T_s and ϕ_l are treated independently. Therefore these equations can be directly solved in a matrix with ε treated as a constant. Then the solution is used to solve for a new ϕ_l . The process is repeated until a converged solution is found, which is to be used in the next timestep. This process is looped until the relative error is reduced to 10^{-5} . This solution method is fastest looping method with both good stability and robustness.

4.2.2 Heat Balance for the discharging cycle

The discharging equation for the particle is same as the charging cycle from the external side. Therefore the water temperature equation remains identical. Water temperature:

$$(T_{w,n+1} - T_{w,n}) \cdot C_w \dot{m} + \sum_{i=1}^n h A_p (T_w - T_s) + m C_w \frac{dT_w}{dt} = 0 \quad (4.19)$$

The Al particle has high conductivity and small radius. Lumped Capacitance method is used, $T_{p,al} = T_{s,al}$:

$$m_p c_p \frac{dT_p^{al}}{dt} = \sum_{i=1}^n \frac{(T_{nbi} - T_p^{al})}{R_{th}} + h_{pg} \cdot A_p (T_w - T_p^{al}) \quad (4.20)$$

The equations are different for PCM particles since there is no longer an internal convective heat transfer that changes with the internal radius. The internal thermal resistance of the PCM particle is now a simple expression.

$$R_{cond} = \frac{r_o - r_i}{4\pi k r_o r_i} \quad (4.21)$$

The heat balance equation at the solidifying interface still applies,

$$q_m = q_l - q_s \quad (4.22)$$

Similarly, q_l is negligible because the initial temperature is close to the melting point of PCM. And the heat transfer rate from the solid side is

$$q_s = \frac{T_w - T_m}{R_{cond} + R_{conv} + R_{wall}} = \frac{T_s - T_m}{R_{cond}} \quad (4.23)$$

As CFD simulation shows, the temperature in the liquid portion of the solidifying PCM quickly drops to and remains at the melting point. Therefore the sensible heat in the liquid can be neglected. Only the heat of the Instead the sensible thermal energy in the system is calculated from the quasi-steady state temperature profile in the solid. First we find the inner surface temperature of the spherical shell of PCM particles.

$$T_s = T_m + \frac{T_w - T_m}{\frac{r_o - r_i}{4\pi k r_o r_i} + \frac{1}{4\pi r_{sh} h_{PCM}} + \frac{r_{sh} - r_o}{4\pi k r_o r_{sh}}} \left(\frac{r_o - r_i}{4\pi k r_o r_i} \right) \quad (4.24)$$

The steady approximation of temperature profile in the solid is:

$$T = \frac{(r - r_i)r_o(T_s - T_m)}{r(r_o - r_i)} + T_m \quad (4.25)$$

The temperature difference using melting point as the reference temperature is:

$$\Delta T = \frac{(r - r_i)r_o(T_s - T_m)}{r(r_o - r_i)} \quad (4.26)$$

The sensible energy in the solid is

$$\Delta E_{sen} = 2\pi \rho c_p \frac{(T_s - T_m)(2r_o^3 - r_i r_o^2 - r_i^2 r_o)}{3} \quad (4.27)$$

The average temperature of the solid is

$$T_p = \frac{\Delta E_{sen}}{\rho V c_p} + T_m = \frac{(T_s - T_m)(2r_o^3 - r_i r_o^2 - r_i^2 r_o)}{2(r_o^3 - r_i^3)} + T_m \quad (4.28)$$

Because the solidification results in a spherical solid-liquid interface, the inner radius is directly related to the liquid volume fraction,

$$r_i = \phi_l^{1/3} r_o \quad (4.29)$$

Expressed in terms of liquid fraction ϕ_l .

$$\Delta E_{sen} = 2\pi\rho c_p \frac{(T_s - T_m)(2r_o^3 - \phi_l^{1/3}r_o^3 - \phi_l^{2/3}r_o^3)}{3} \quad (4.30)$$

The sensible heat rate of the solid is

$$Q_{sen} = 2\pi\rho c_p \frac{(T_s - T_m)(-\phi_l^{-2/3}r_o^3 - 2\phi_l^{-1/3}r_o^3)}{9} \frac{d\phi_l}{dt} \quad (4.31)$$

The latent heat rate is

$$Q_{lat} = m_p \Delta h_m \frac{d\phi_l}{dt} = \rho \Delta h_m \frac{4\pi r_o^3}{3} \frac{d\phi_l}{dt} \quad (4.32)$$

The overall heat balance equation is

$$Q_{sen} + Q_{lat} = Q_{in} \quad (4.33)$$

Expressed in terms of ϕ_l ,

$$2\pi\rho c_p \frac{(T_s - T_m)(-\phi_l^{-2/3}r_o^3 - 2\phi_l^{-1/3}r_o^3)}{9} \frac{d\phi_l}{dt} + \rho \Delta h_m \frac{4\pi r_o^3}{3} \frac{d\phi_l}{dt} = \frac{4\pi k r_o \phi_l^{1/3} (T_s - T_m)}{1 - \phi_l^{1/3}} \quad (4.34)$$

$$\frac{4}{3}\pi\rho r_o^3 \left(\frac{(T_s - T_m)(-\phi_l^{-2/3} - 2\phi_l^{-1/3})c_p}{6} + \Delta h_m \right) \frac{d\phi_l}{dt} = \frac{4\pi k r_o \phi_l^{1/3} (T_s - T_m)}{1 - \phi_l^{1/3}} \quad (4.35)$$

$$\frac{d\phi_l}{dt} = \frac{3k(T_s - T_m)}{r_o^2\rho} \left(\frac{6\phi_l^{1/3}}{(1 - \phi_l^{1/3})((T_s - T_m)(-\phi_l^{-2/3} - 2\phi_l^{-1/3})c_p + 6\Delta h_m)} \right) \quad (4.36)$$

Discretization using Implicit Euler method

$$\frac{\phi_{l,i} - \phi_{l,i-1}}{\Delta t} = \frac{3k(T_s - T_m)}{r_o^2\rho} \left(\frac{6\phi_{l,i}^{1/3}}{(1 - \phi_{l,i}^{1/3})((T_s - T_m)(-\phi_{l,i}^{-2/3} - 2\phi_{l,i}^{-1/3})c_p + 6\Delta h_m)} \right) \quad (4.37)$$

Solve using Newton's method

$$f(\phi_{l,i}) = \frac{\phi_{l,i} - \phi_{l,i-1}}{\Delta t} - \frac{3k(T_s - T_m)}{r_o^2\rho} \frac{6\phi_{l,i}^{1/3}}{(1 - \phi_{l,i}^{1/3})((T_s - T_m)(-\phi_{l,i}^{-2/3} - 2\phi_{l,i}^{-1/3})c_p + 6\Delta h_m)} \quad (4.38)$$

$$f'(\phi_{l,i}) = \frac{1}{\Delta t} + \frac{6k(T_s - T_m)}{r_o^2\rho} \frac{(-6\Delta h_m - 2(T_s - T_m)c_p)\phi_{l,i}^{2/3} + 2(T_s - T_m)c_p\phi_{l,i}^{1/3} + 3(T_s - T_m)c_p}{(1 - \phi_{l,i}^{1/3})^2((1 + 2\phi_{l,i}^{1/3})(T_s - T_m)c_p + 6\phi_{l,i}^{2/3}\Delta h_m)^2} \quad (4.39)$$

4.2.3 Computational Methods

The overall computational process is summarized in the Fig. 4.1. The heat balance equation in discrete form for heat storage are a linear system of equations, if the convection heat transfer coefficient is treated as a constant. The system of equations can be directly solved. The matrix consists of as many variables as the number of particles. Gaussian elimination is used in MATLAB to solve the matrix. The computation time with gaussian elimination grows quadratically with the number of particles in the system. For the current analysis, the number of particles is below 10000. The computation time is within acceptable range. If a larger-scale system is simulated with hundreds of thousands of particles, Iterative solvers are recommended over direct solvers. Iterative solvers such as Gauss-Seidel method will work well because

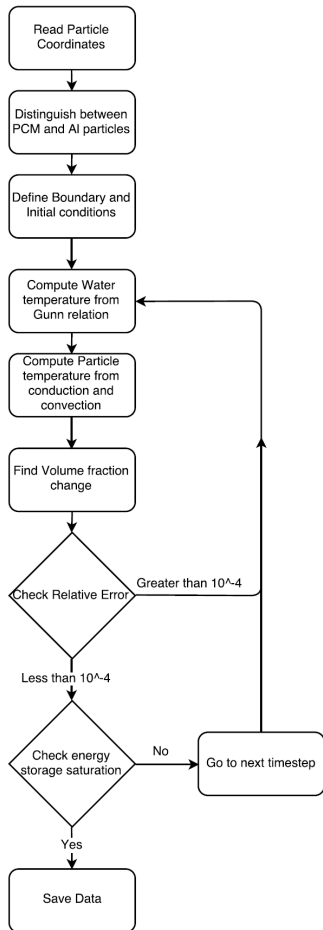


Figure 4.1: Heat Storage in Fixed Bed Computation Scheme Flowchart

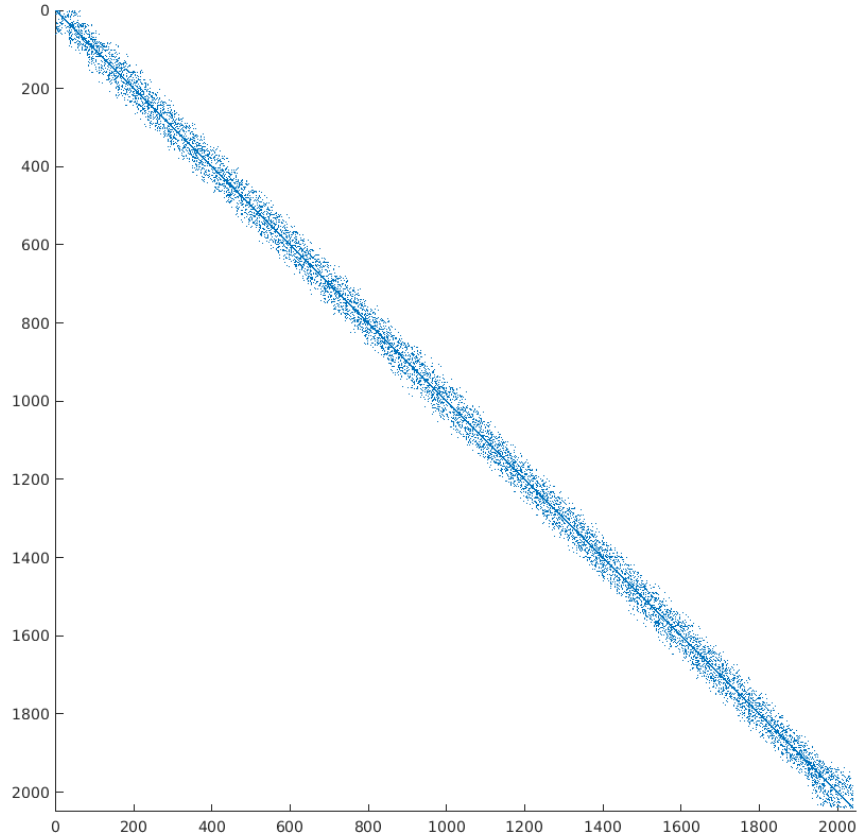


Figure 4.2: Matrix distribution for $\varepsilon_{Al} = 0.27$ with nonzero terms shown as dots

1. the matrix is diagonally dominant.
2. the matrix is sparse.
3. the matrix is nearly diagonal.

For illustration, the nonzero term distribution for the matrix is plotted in Fig. 4.2. As seen in the plot, the nonzero terms are very close to the diagonal. These features of the matrix make it easy to solve in numerical analysis.

4.3 Simulation Setup

To store thermal energy from the water, the water temperature must be higher than the melting point of the PCM. Conversely, to release energy from the PCM, the melting point of the PCM must be higher than the water temperature. Therefore in theory, the maximum thermal energy recoverable from the water depends on the temperature difference between the water and the melting point of the material.

$$\dot{E}_{max} = \dot{m}c_p(T_{w_i} - T_m) \quad (4.40)$$

The actual heat transfer rate is the

$$\dot{E}_{st} = \dot{m}c_p(T_{w_i} - T_{w_o}) \quad (4.41)$$

Height of cylinder, m	# of PCM capsules	# of Al particles	Al percentage
1	745	1	0.1
1	456	762	17.3
1	413	1270	27.7
1	331	2043	43.5
1	255	2581	55.8
1	1	4574	99.8

Table 4.2: Simulation setup for charging and discharging cycles of fixed-bed heat storage unit, Set 1

Nominal % Al	Height of cylinder, m	# of PCM capsules	# of Al particles	% Al
0	0.800	415	0	0
9	0.875	415	422	11.3
20	0.936	415	833	20.1
27	1.020	415	1248	27.3
33	1.099	415	1639	33.1
43	1.270	415	2454	42.5
50	1.458	415	3298	49.8
33	2.163	415	6463	66.1
80	3.000	415	10118	75.3

Table 4.3: Simulation setup for charging and discharging cycles of fixed-bed heat storage unit, Set 2

Obviously it is not possible to harvest all of the available energy from water unless the water is at thermal equilibrium with the PCM at the outlet of the fixed bed. The effectiveness of thermal energy storage can be defined as the ratio of heat transfer rate over the maximum available energy.

For all simulations, the paraffin used in the previous chapter is chosen to be the PCM. The properties of the PCM used in this simulation are same as that used for CFD simulation used before. For free cooling applications, a melting temperature between 20 and 22 °C is the ideal in a continental climate [61]. For a system where heating is the major function, the paraffin with a melting temperature at 28 °C, as used in the last chapter, is most suitable. Instead of using a glass shell, a steel shell was used for steel's better thermal conductivity and toughness. The steel's thermal conductivity was 54 W/mK and its heat capacity was neglected. For the charging cycle, the inlet water temperature was set to be 20 °C higher than the melting point of the paraffin. For the discharging cycle, the inlet water temperature was set to be 20 °C lower than the melting point of the paraffin.

The simulation for the both the charging cycle and the discharging was carried out for two sets of configurations. The first set of simulations compared the heat storage devices with identical dimensions. but filled with different proportions of PCM capsules and Al particles. The second set of simulation compared the temperature and energy changes over time for heat storage devices with different proportions of PCM capsules and Al particles and different heights, but the identical number of PCM particles. For all of the simulations, the particles were contained in a cylinder with a radius of 0.1m. Water is used as heat transfer medium flowing from the bottom of the bed to the top of the bed. The first set of simulations has its parameters listed in Tab. 4.2. The second set of simulations has its parameters listed in Tab. 4.3.

4.4 Results

The particle-averaged temperature of the fixed bed were visualized in Fig. 4.3-4.8. The Al particles were heated up or cooled down to temperature within 10 min. When there was not any aluminum particle in the fixed bed like Fig. 4.5, the temperature difference between the top and bottom of the fixed bed was around 10°C during the charging cycle. The addition of Al particles reduced the temperature gradient in the fixed bed. The overall time until completion shortens by 5% to 20%.

In the first set of simulations, the total energy storage was plotted in 4.10. The total energy storage

in the system included latent and sensible energy for the PCM particles, Al particles and residual water. Because the heat storage unit contains less PCM as Al particles occupy space, the total heat capacitance of the unit has decreased. However, the total energy stored in the heat storage unit was seen to increase in the first 10 min if more Al particles were added in the system. Aluminum has high conductivity and high volumetric heat capacity. After the 10-min mark, the sensible heat storage has saturated and the systems with less aluminum overtake the systems with more aluminum in total heat storage.

The average temperature of the PCM capsules and Al particles were plotted in Fig. 4.17 and 4.21 respectively. The PCM capsules were seen to rise in temperature much quicker with more Al particles in the mix. However, the increased heat transfer had more to do with heat exhaustion in the HTF than it is with low convection.

In Fig. 4.9, the water temperature profile in the heat storage unit is shown. The heat loss from water is equal to the heat absorbed by the heat storage unit.

$$\dot{E}_{st} = \dot{m}c_p\Delta T \quad (4.42)$$

When the system is saturated, the inlet and outlet temperatures will be equal. The effectiveness of the TES is defined as:

$$\epsilon = \frac{\dot{E}_{st}}{\dot{E}_{max}} \quad (4.43)$$

Overall, the storage effectiveness is fairly high for the current analysis, with ΔT being around 5K, meaning about 25% of the total thermal energy from the water is recovered. However, this effectiveness is based on a relatively low flow rate compared other studies in literature [105, 106]. Despite the low flowrate, the unit's heat capacity is exhausted after about 1 hour.

- Allow more residual time of HTF in the heat storage unit
- Increase size of the heat storage unit to allow for more surface area

The first option sacrifices overall heat rate in favour of effectiveness. If the flowrate of HTF is reduced, residual time is increased in the fixed bed. This method is useful when the amount of energy available is limited. When the heat is abundant, the water flow rate should be set higher to maximize heat transfer rate. When heat is scarce, the water should be allowed more residual time to achieve better storage effectiveness. In reality, the amount of solar heat available changes with time and weather conditions. For realistic transient inlet temperature, the dynamic control of the flowrate in response to temperature changes are important for optimizing heat storage in a TES [107]. Therefore the system should have real-time adjustability of the flow rate of water to adapt to heat availability.

The second option is spatially demanding. Since most designs have to be incorporated in a facility where space is a limiting factor, the size of the heat storage unit is often a predicament. A larger fixed bed also requires more pumping power since the pressure drop is going to be higher, increasing the energy consumption and possibly lowering overall efficiency.

The first set of simulations shows that the small aluminum particles can improve heat transfer and heat storage at the beginning of the process. However, shown in Fig. 4.10, the improvement is marginal in terms of the total energy absorption. The heat storage rate is only better for systems with aluminum particles for the initial part when $Fo \cdot Ste \ll 2$. Ultimately, the design of the heat storage unit must depend on the system requirement. If the goal is to achieve maximum heat storage in a short period of time, adding aluminum particles is a useful solution. However, if the design is a spatially compact unit that needs large capacity, adding aluminum will not improve the performance of the heat storage unit.

However, if the aluminum particles are small enough, they can occupy gaps between PCM particles without sacrificing the space for PCM particles. In theory, the number of aluminum particles that can fit in the gaps between PCM particles is based on gaps between PCM particles in close packing. The type of interstitial vacancies, the numbers per PCM particle, their sizes, and volume fraction are listed in Tab.4.4. There are two major type of interstitial vacancies in a close packed system, the octahedral vacancies and tetrahedral vacancies. For each PCM particle, there is 1 octahedral site and 2 tetrahedral sites. In real

Coordination	N_{Al}/N_{PCM}	r_{Al}/r_{PCM}	V_{Al}/V_{PCM}
Octahedral	1	0.414	0.071
Tetrahedral	2	0.225	0.023
Total	3	N/A	0.094

Table 4.4: Vacancy sites in closed packing with ratios of sites, radii, and volumes

gravity-condensed packing, the gaps are slightly larger and more disordered. However, it still requires extensive and elaborate mixing for the aluminum particles to reach such vacancies. To validate the theory, a separate set of simulation has been conducted using the mix of PCM and aluminum particles proportioned based on interstitial vacancies.

In the second set of simulations, the same number of PCM particles was used for all cases under investigation. Different amount of aluminum particles was mixed in the PCM particles. The results were plotted in similar styles. The total energy storage is plotted in 4.13. The latent energy storage is plotted in 4.14. The latent energy instead of total energy is especially important since it can be stored at the melting temperature of the PCM, giving off a sustained heat output for a long time with minimal unwanted heat loss. The latent heat storage rate increases due to the introduction of aluminum particles in the system. Aluminum particles increase the surface area to increase heat transfer rate when the heat transfer is convection-limited. However, if too many Al particles are added, the heat required to heat up the aluminum particles will outweigh the additional heat transferred to the PCM particles, and the latent heat storage is reduced instead. Overall, the quickest case to reach saturation of latent heat capacity is when $\varepsilon_{Al} = 0.27$. The saturation time is plotted in Fig. 4.15. The results show there is no benefit adding more aluminum particles over the volume fraction of 0.27. Adding 0.27 volume fraction aluminum gives 10% quicker charging, but results in 20% less heat capacity per volume. Although 0.27 is the quickest volume fraction for the current system to reach saturation, it may not be the optimal volume fraction for the system if saturation of capacity is not desired, i.e. if charging is stopped before the PCM is completed melted. The premature termination of charging is expected in operation of the heat storage unit, attributed to the following reasons.

1. The unpredictable availability of sunshine due to weather conditions
2. The duration of daylight due to seasonal changes
3. The change to the discharging cycles due to demand

Therefore a system designed for one set of conditions will not be the ideal setup for operation in a different scenario.

The same simulations were conducted for the discharging cycle of the fixed bed. Results from the previous chapter showed that the time for solidification is longer than melting for the same temperature difference for PCM capsules greater than 1mm in radius. Since the PCM capsules had radii of 2mm, the discharging cycle took longer to complete as expected. The average PCM particle temperature are plotted in Fig. 4.17 for the charging cycle and in Fig. 4.20 for the discharging cycle. The average Al particle temperature are plotted in Fig. 4.21. The resultant temperature plots shown in Fig. 4.11 are near symmetrically opposite of each other. The effect of adding aluminum in the fixed bed has the safe effect during discharging as during charging. Heat transfer rate is slightly increased at the expense of heat capacity.

All in all, simulations show that the aluminum particles inside the heat storage unit can improve heat transfer. The heat transfer rate is increased by additional heat transfer from fluid to particle shell. However, the improvement is most significant at the beginning of the melting/solidification, because the heat transfer rate is only dominated by the external resistance at the beginning. However, as the PCM melts or solidifies, the distance grows between the melting interface and the heat transfer medium, and the internal resistance increases proportionately. The simulations in the current study uses a flowrate that is relatively low. If the flowrate is increased any higher, the external resistance is even less significant than it is for the current analysis. Therefore aluminum particles are more suitable for systems with low flowrate and long residual time. We find that the system benefits the addition from aluminum particles before the 10 min mark. For

the current flow rate, the total charging/discharging time can be reduced by 11% using an aluminum volume fraction of 0.27.

In conclusion, mixing aluminum particles between PCM particles in a heat storage unit is a viable method of improving performance. Heat transfer can be increased given the particles are small enough. For PCM particles of $r_{PCM} = 2\text{cm}$ or under, the heat rate is at least affected by the convection rate of external flow for the majority of time. Aluminum particles work by increasing the surface area for convection. The other benefit of the aluminum particles is its sensible heat storage, which reduces response time of the system for the fluctuations of temperature. However, there is a limit for which the addition of aluminum particles no longer helps heat transfer. The time till saturation is the exact amount of aluminum particles to be added depends on the optimization goal of the system. If the goal is to optimize heat storage rate, the heat storage unit should have $\varepsilon_{Al} = 0.27$, since it gives the best overall heat transfer rate from water to PCM. However, if the heat storage design is limited by its size, the addition of aluminum particles cannot increase the heat storage capacity or improve the heat transfer rate over the entire melting process. In fact, for cases with controlled volume heat transfer rate is only slightly improved. The improvement is also concentrated during the initial part when $Fo \cdot Ste > 2$. Therefore if the size of the heat storage unit is the limiting factor, adding large amount of aluminum is inadvisable because the space occupied by aluminum particles results in reduction in heat capacity, The cost in heat capacity outweighs gains in heat rate.

4.5 Figures

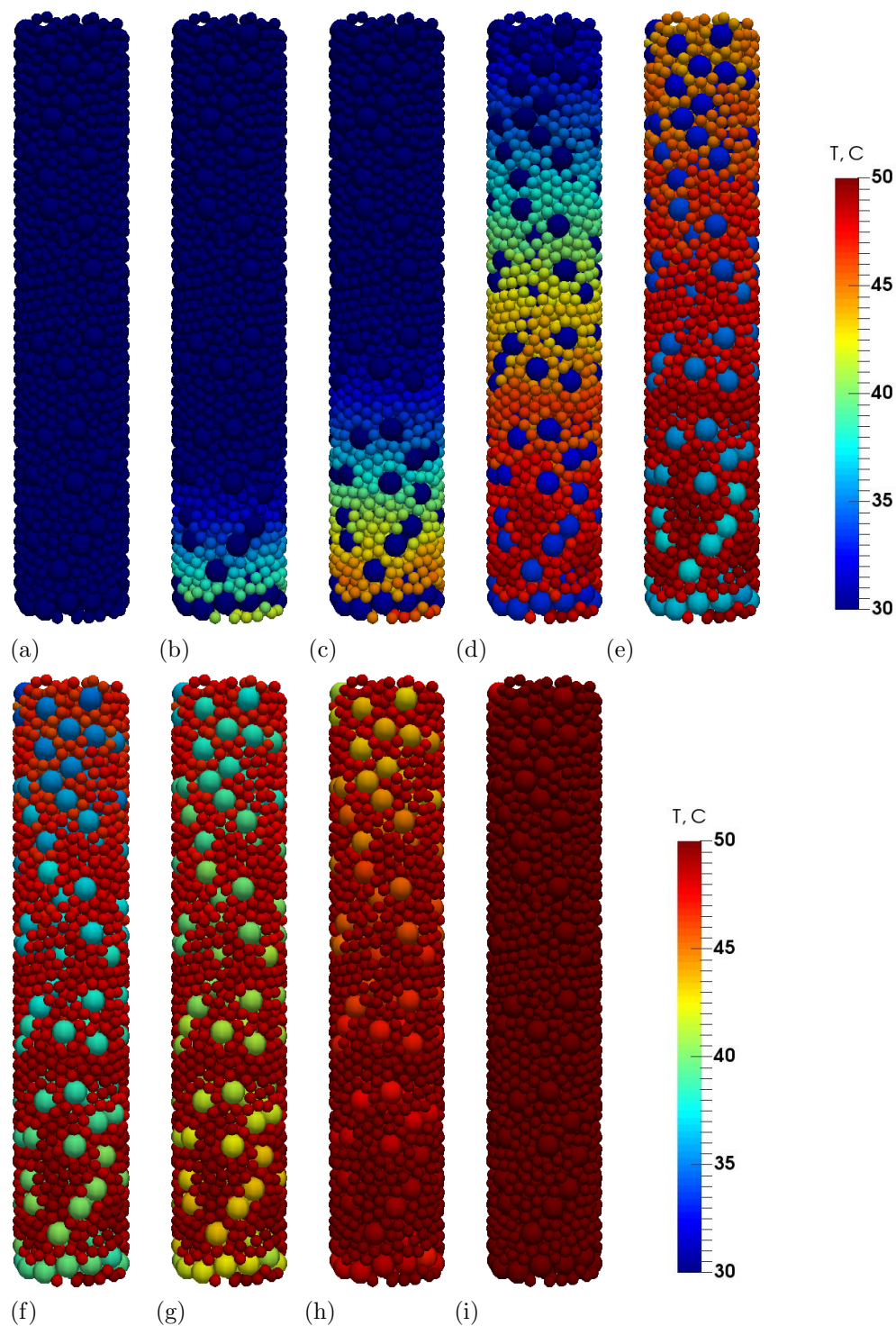


Figure 4.3: 3D visualization of PCM with 60% Al particles by average temperature during the charging cycle at (a)0min, (b)1min, (c)2min, (d)5min, (e)10min, (f)15min, (g)20min, (h)30min, (i)40min

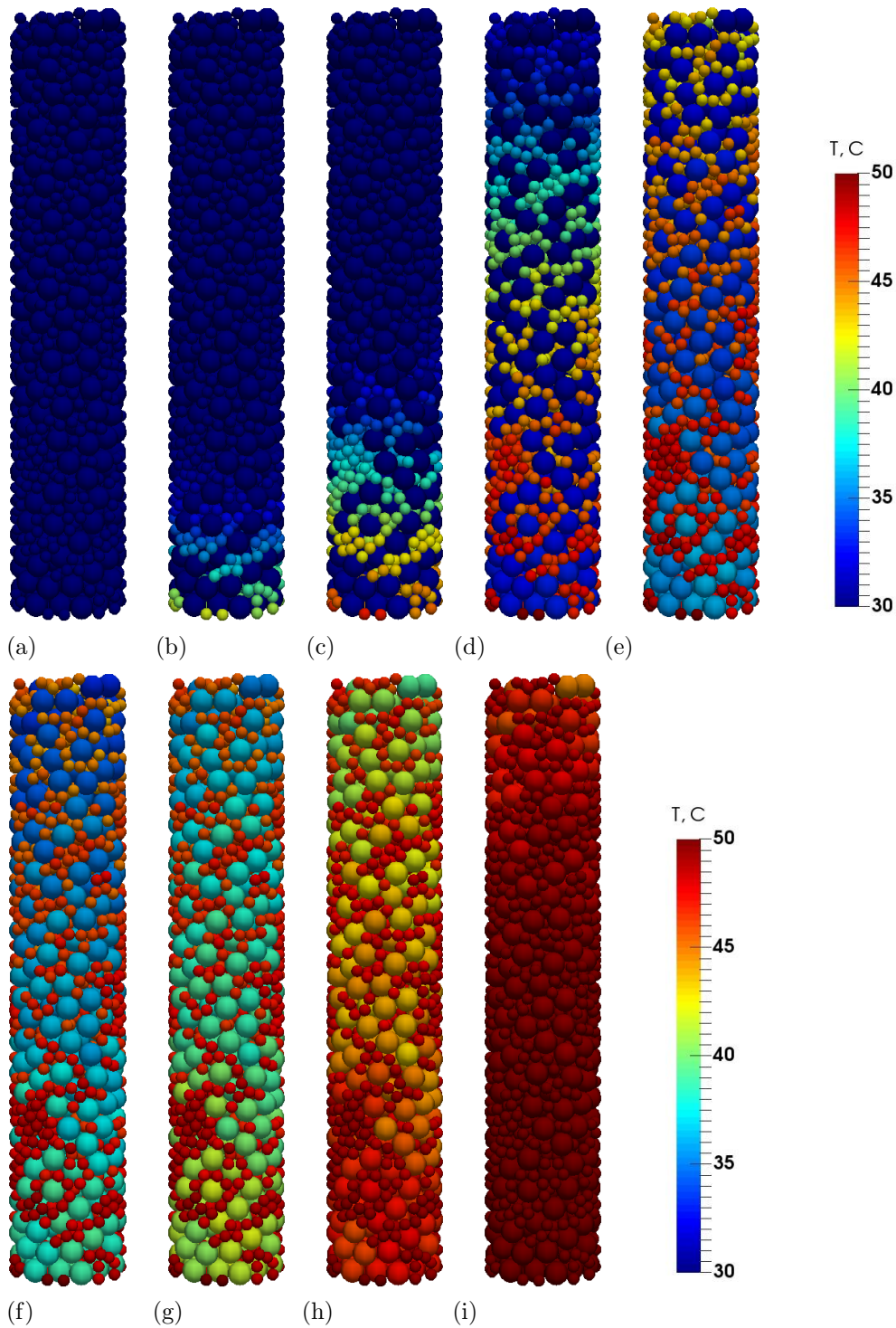


Figure 4.4: 3D visualization of PCM with 33% Al particles by average temperature during the charging cycle at (a)0min, (b)1min, (c)2min, (d)5min, (e)10min, (f)15min, (g)20min, (h)30min, (i)40min

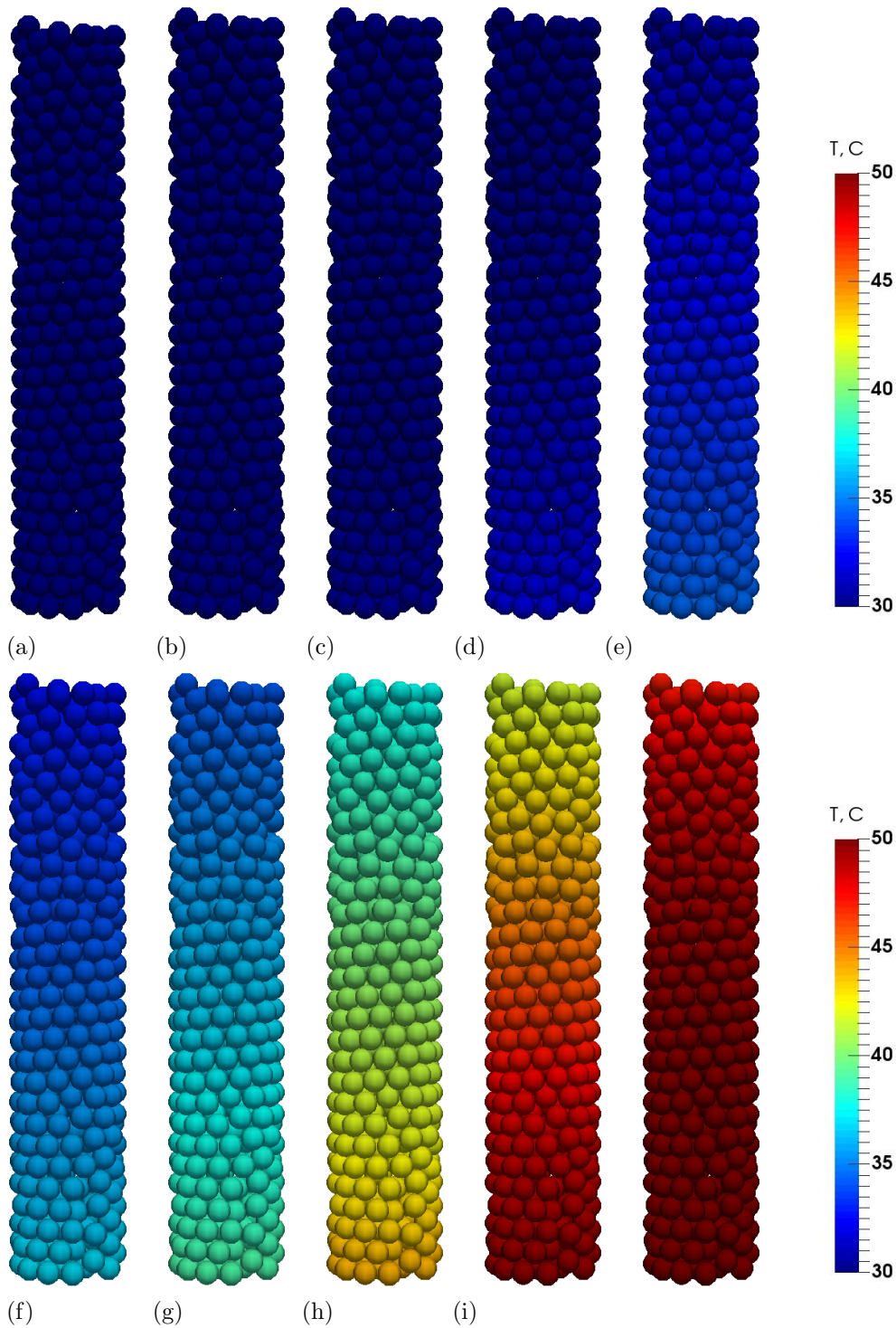


Figure 4.5: 3D visualization of PCM without Al particles by average temperature during the charging cycle at (a)0min, (b)1min, (c)2min, (d)5min, (e)10min, (f)15min, (g)20min, (h)30min, (i)40min, (j)50min

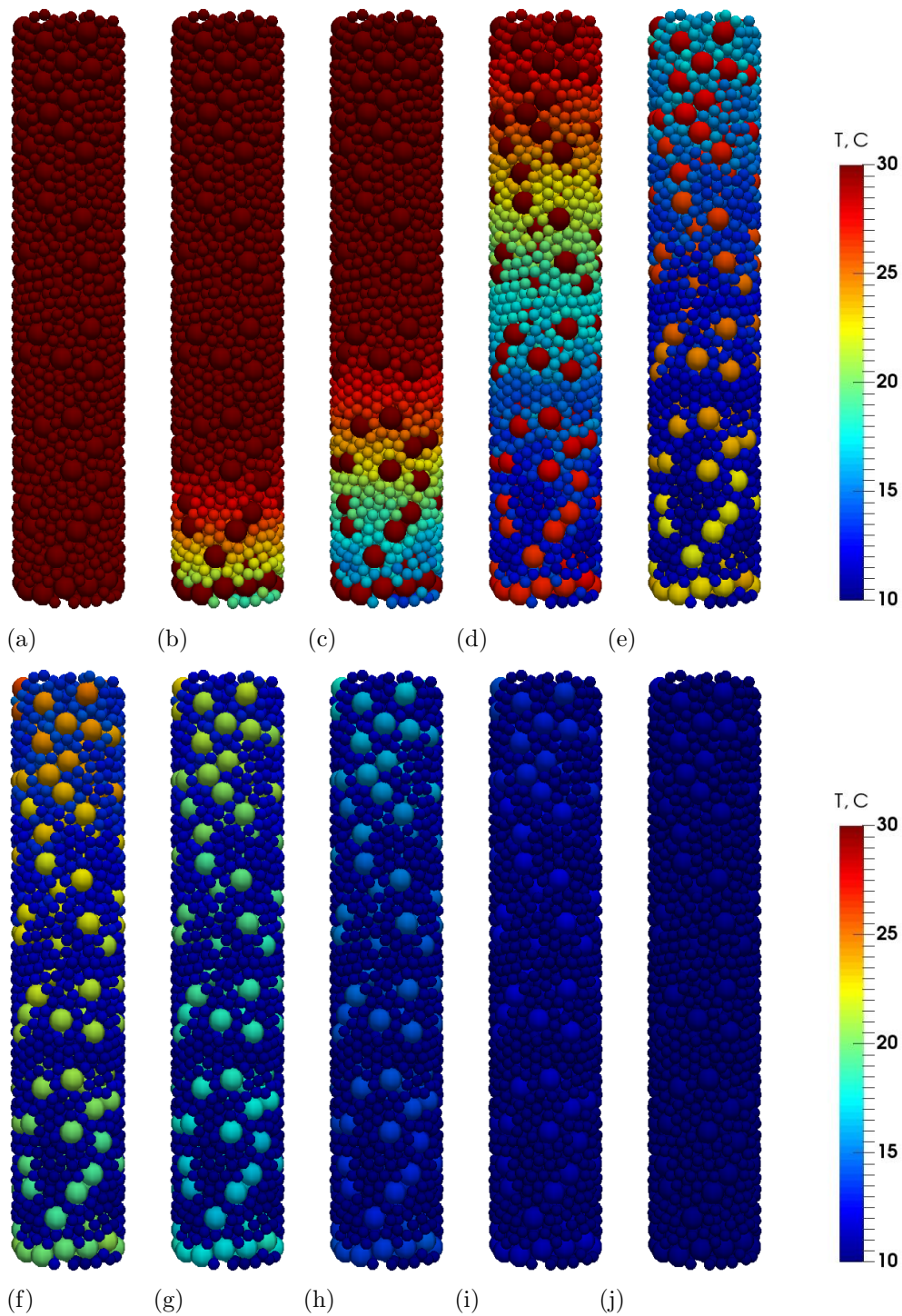


Figure 4.6: 3D visualization of PCM with 60% Al particles by average temperature during the discharging cycle at (a)0min, (b)1min, (c)2min, (d)5min, (e)10min, (f)15min, (g)20min, (h)30min, (i)40min, (j)50min

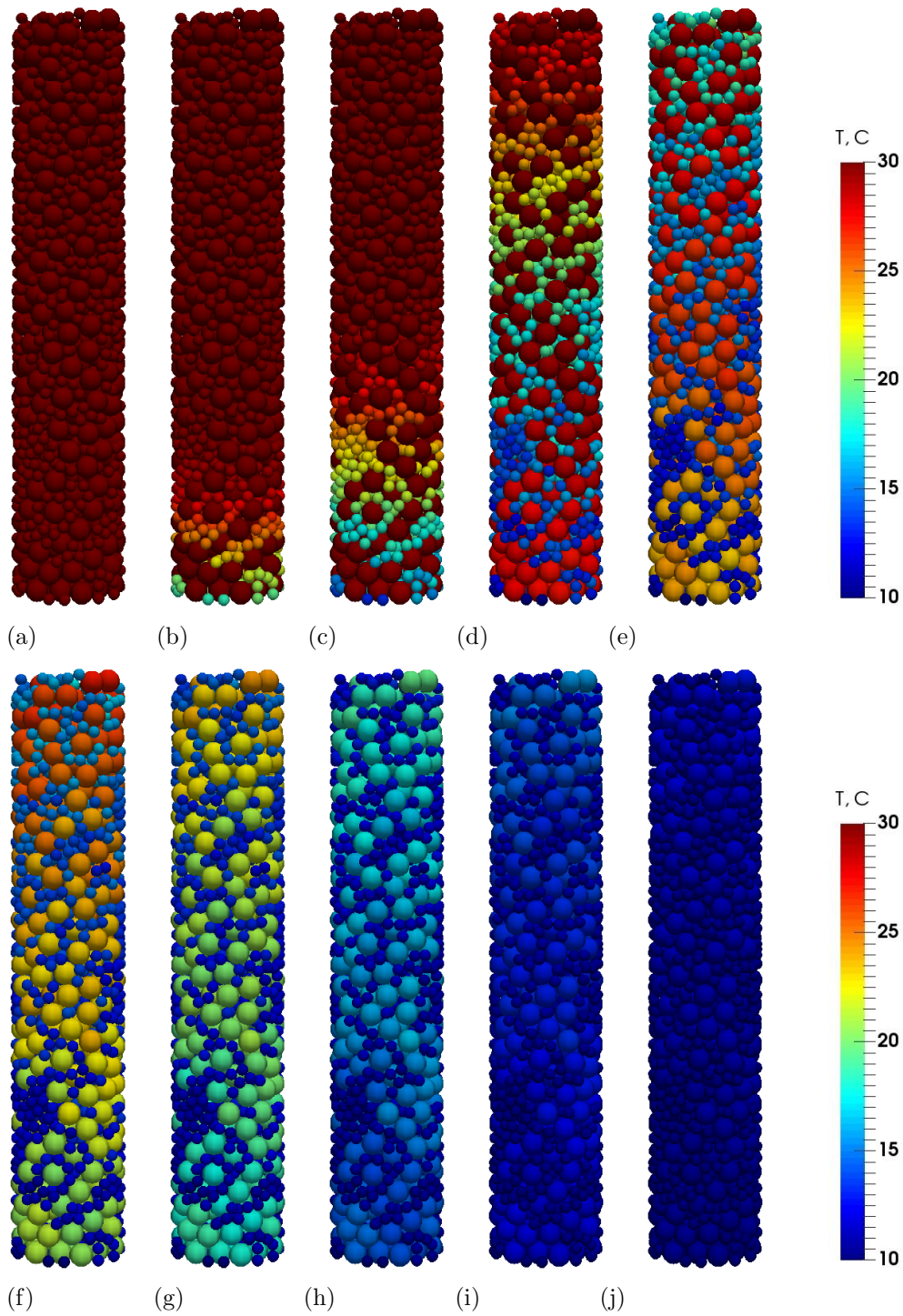


Figure 4.7: 3D visualization of PCM with 33% Al particles by average temperature during the discharging cycle at (a)0min, (b)1min, (c)2min, (d)5min, (e)10min, (f)15min, (g)20min, (h)30min, (i)40min, (j)50min

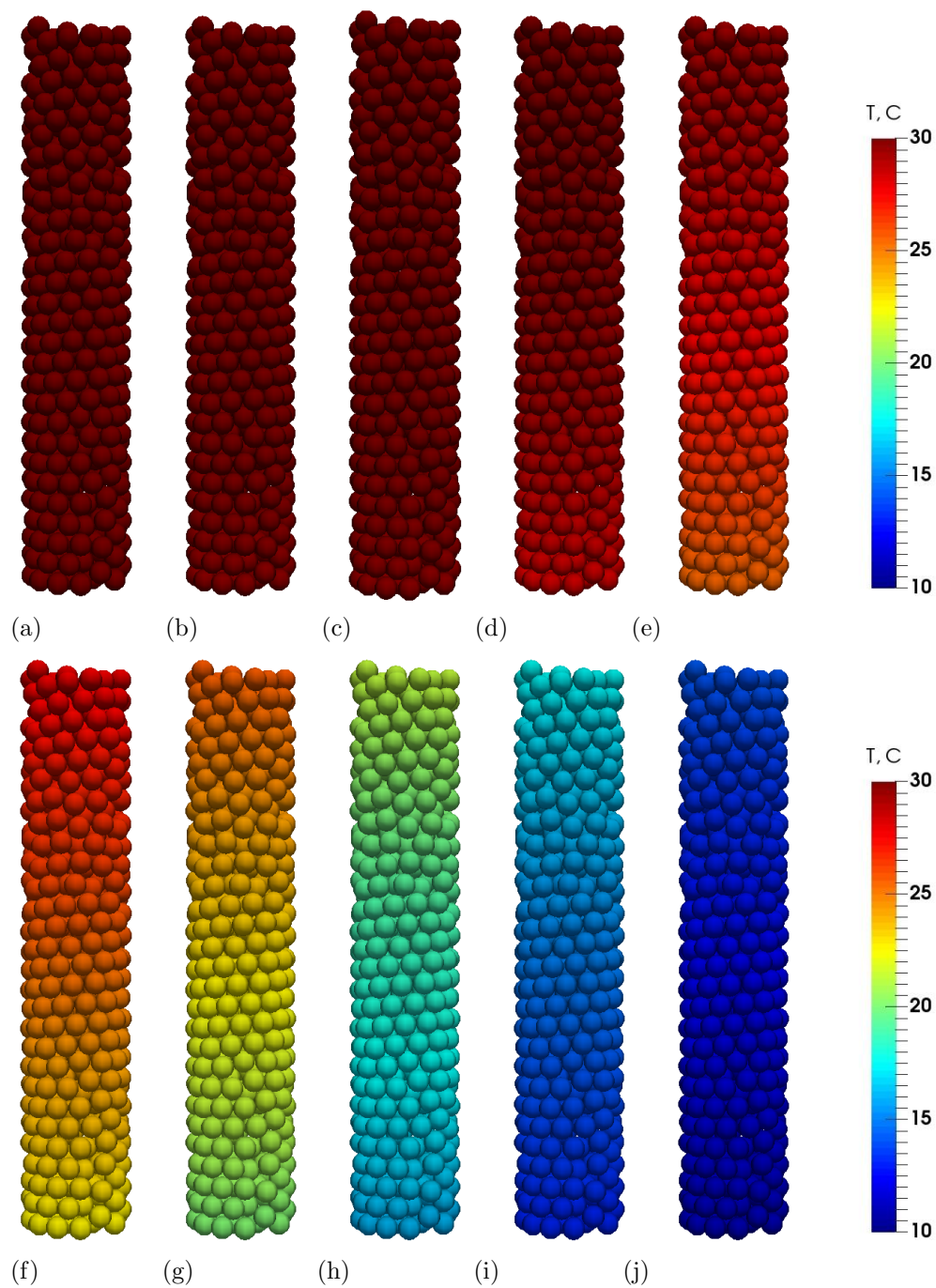


Figure 4.8: 3D visualization of PCM without Al particles by average temperature during the discharging cycle at (a)0min, (b)1min, (c)2min, (d)5min, (e)10min, (f)15min, (g)20min, (h)30min, (i)40min, (j)50min

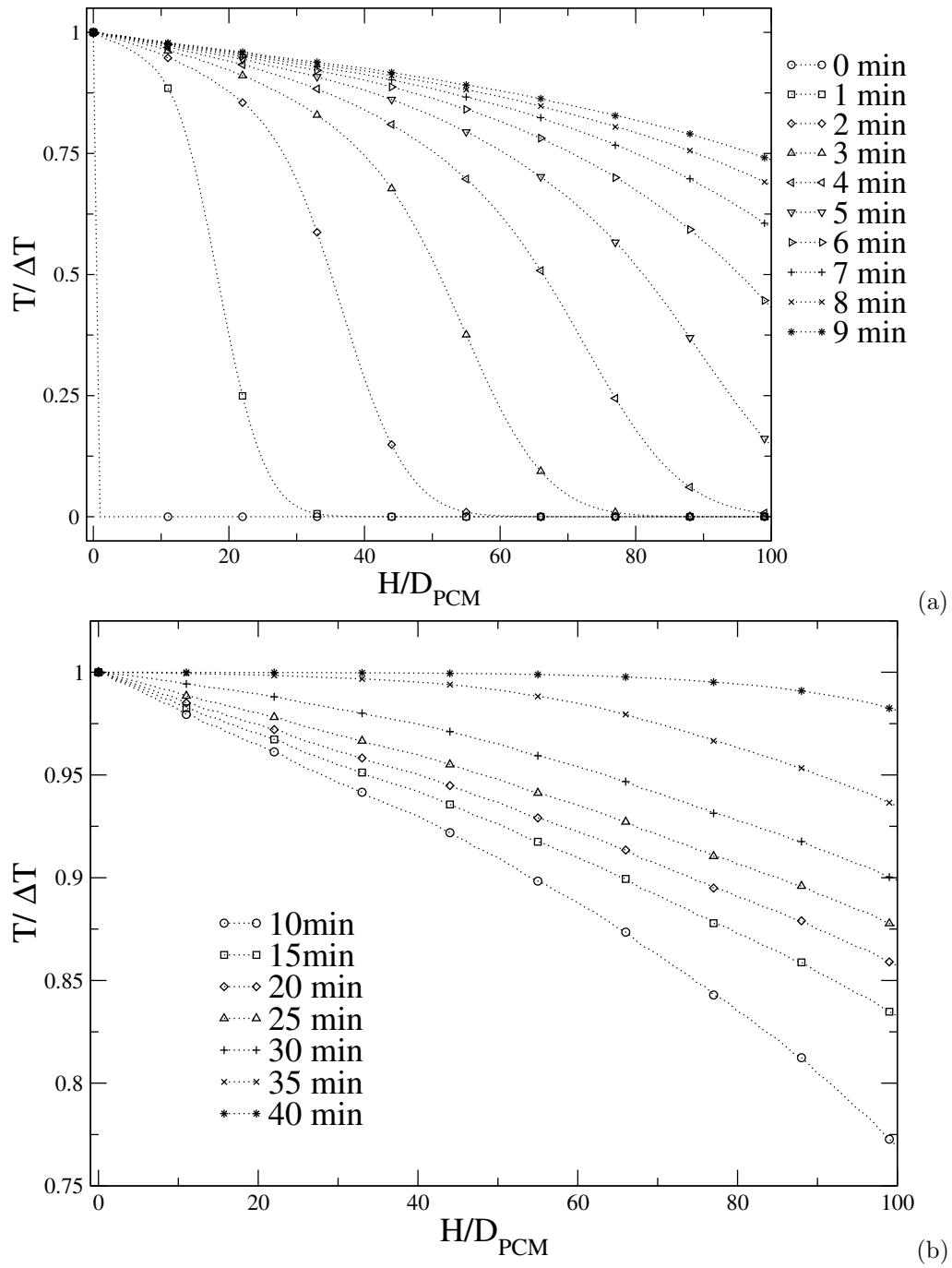


Figure 4.9: Water Temperature Profile for the charging cycle (a)0-10 min, (b)10-40min

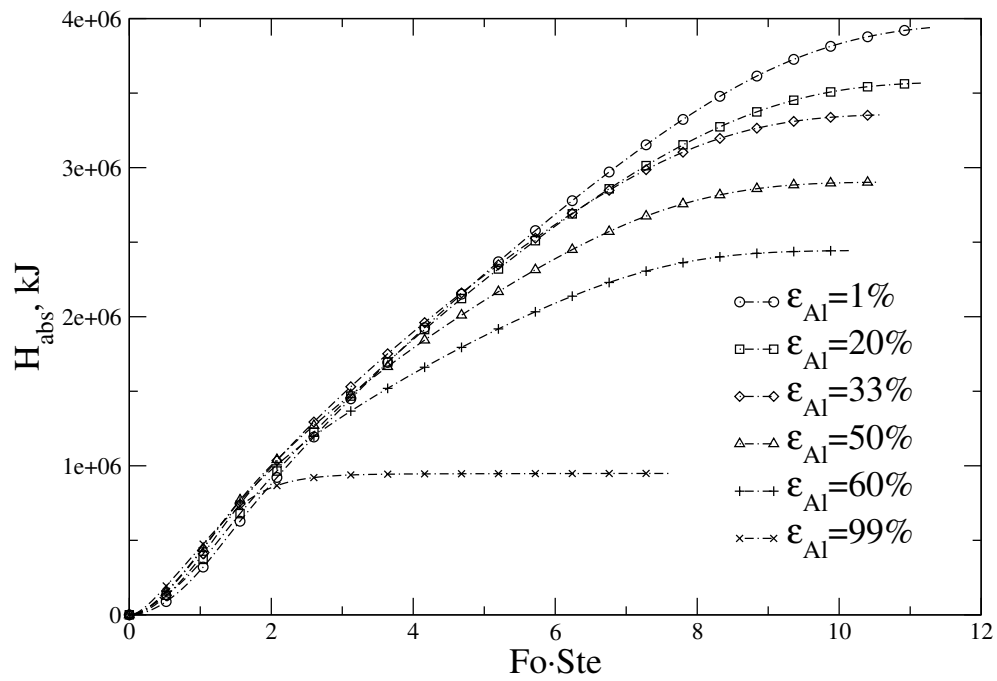


Figure 4.10: Total energy absorption over time during the charging cycle

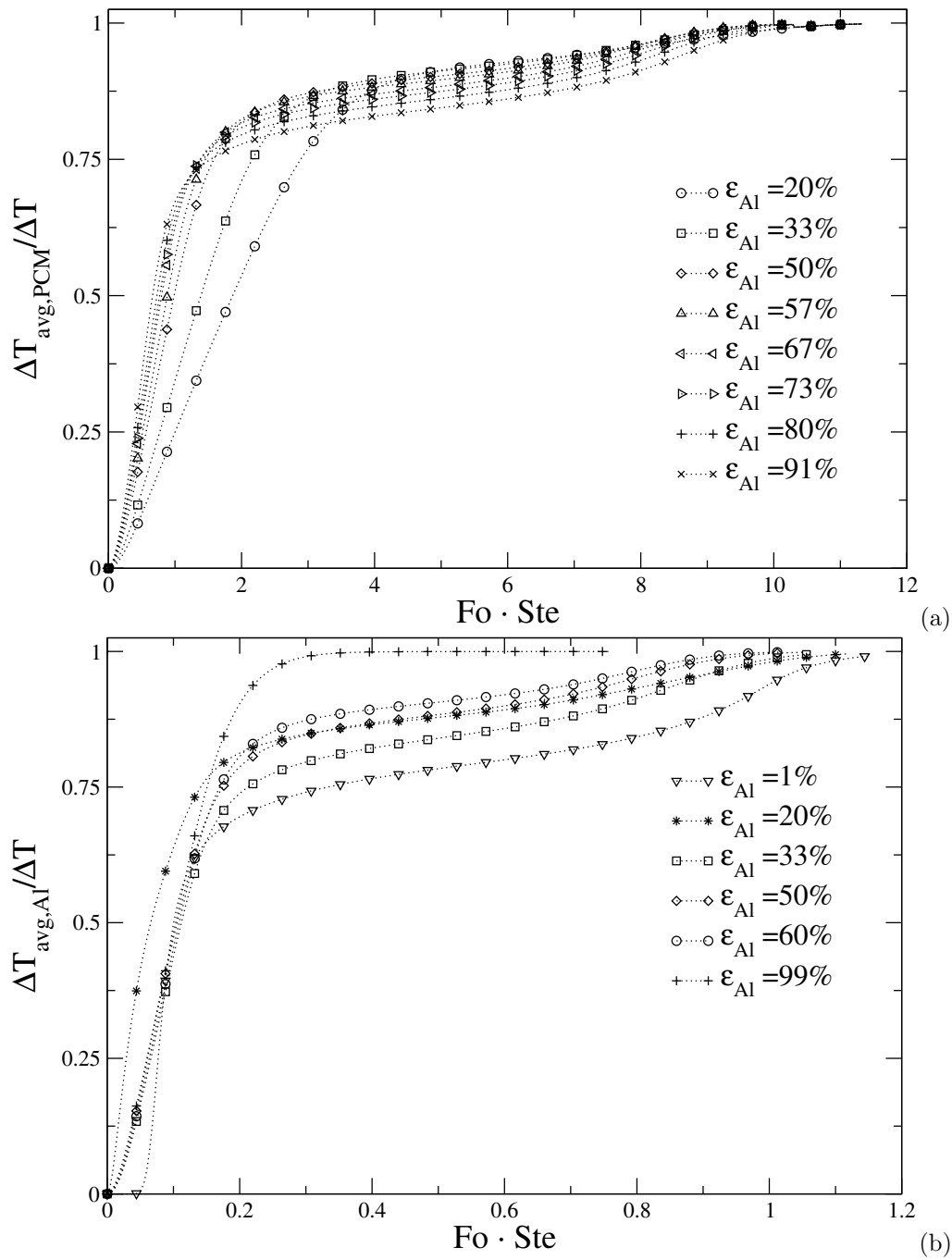


Figure 4.11: Average (a) PCM particle and (b) Al particle temperature over time during the charging cycle for equal size of heat storage unit

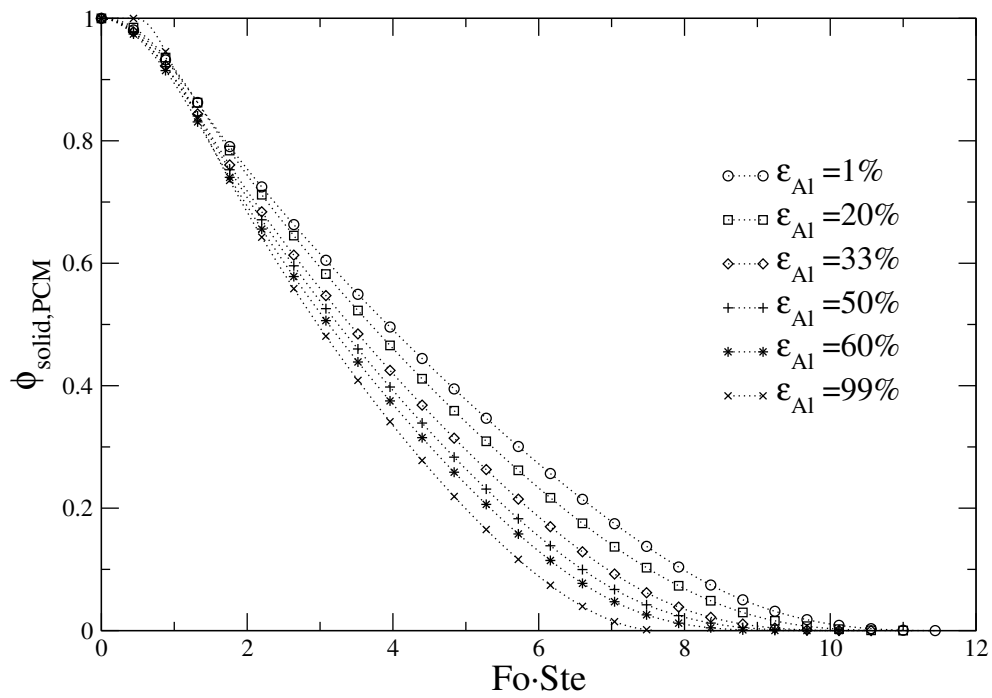


Figure 4.12: Average solid volume fraction for equal size of heat storage unit

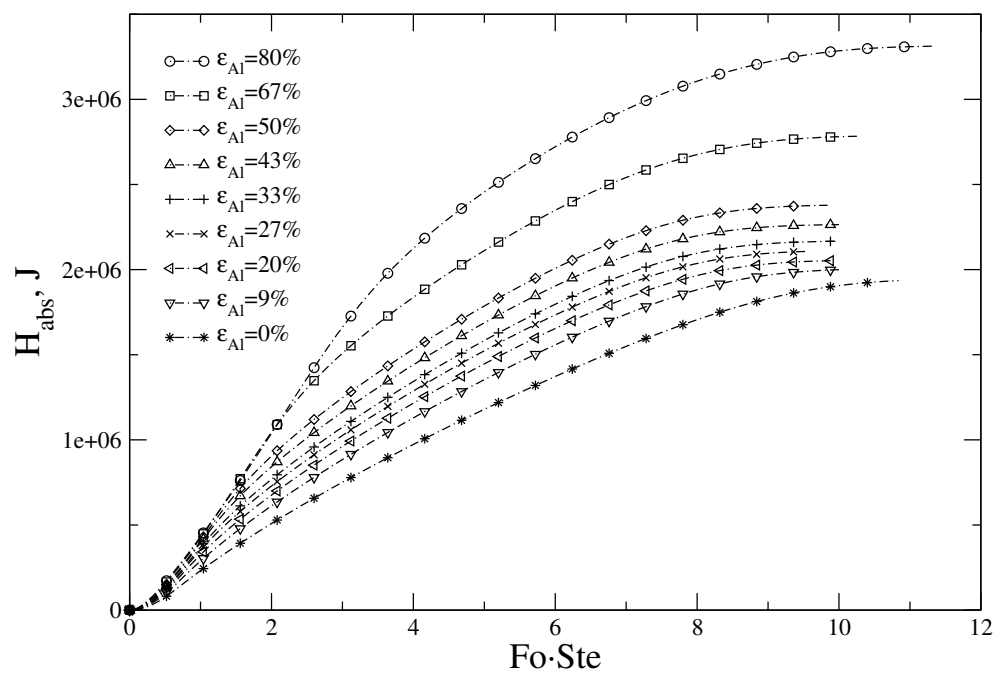


Figure 4.13: Latent and sensible heat stored comparison for equal amount of PCM particles and different volume fractions of Al particles

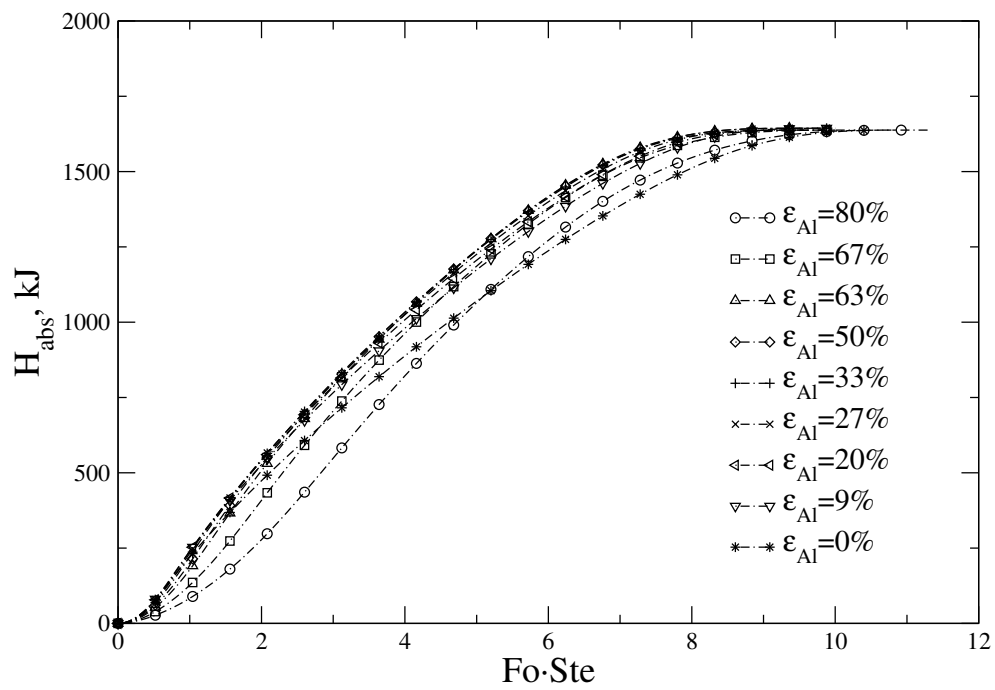


Figure 4.14: Latent heat stored comparison for equal amount of PCM particles and different volume fractions of Al particles

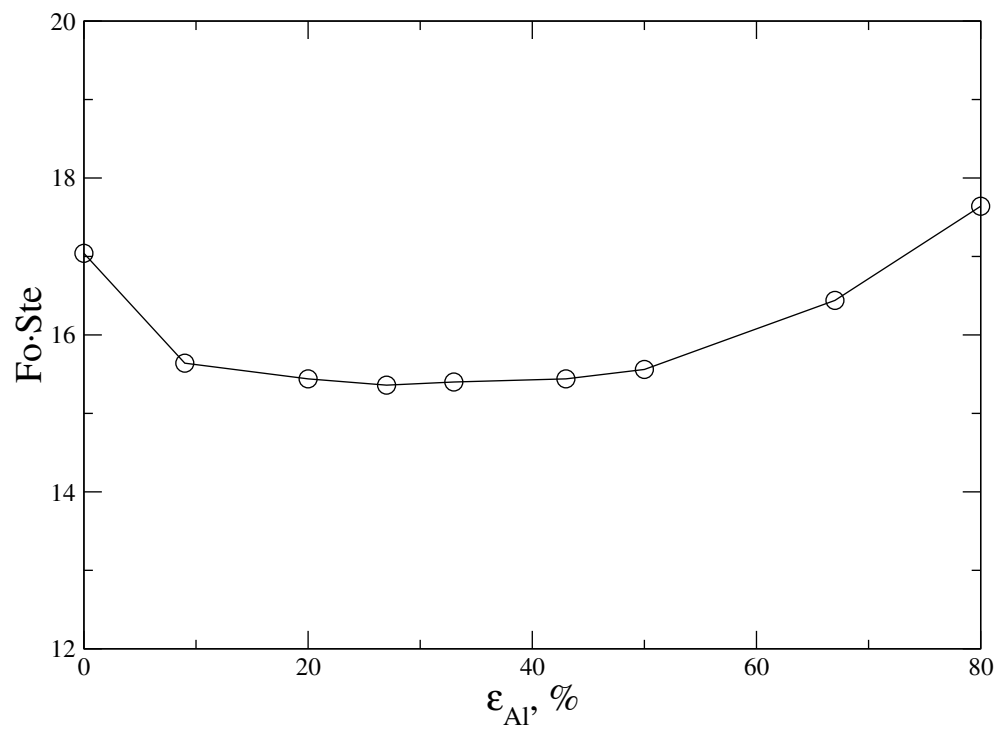


Figure 4.15: Time required for latent heat storage to reach saturation

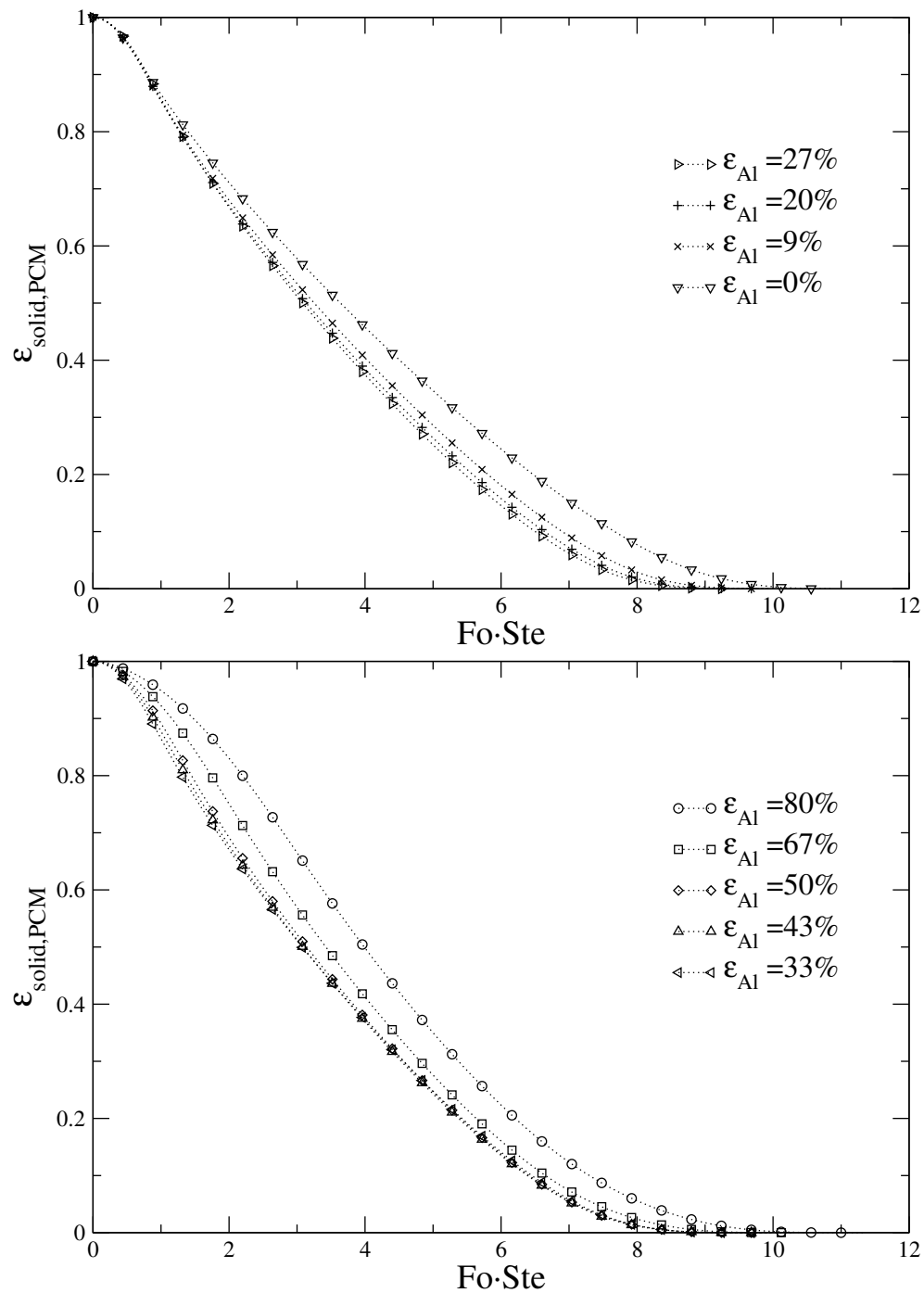


Figure 4.16: Average solid volume fraction during charge for equal number of PCM and different volume fractions of Al particles

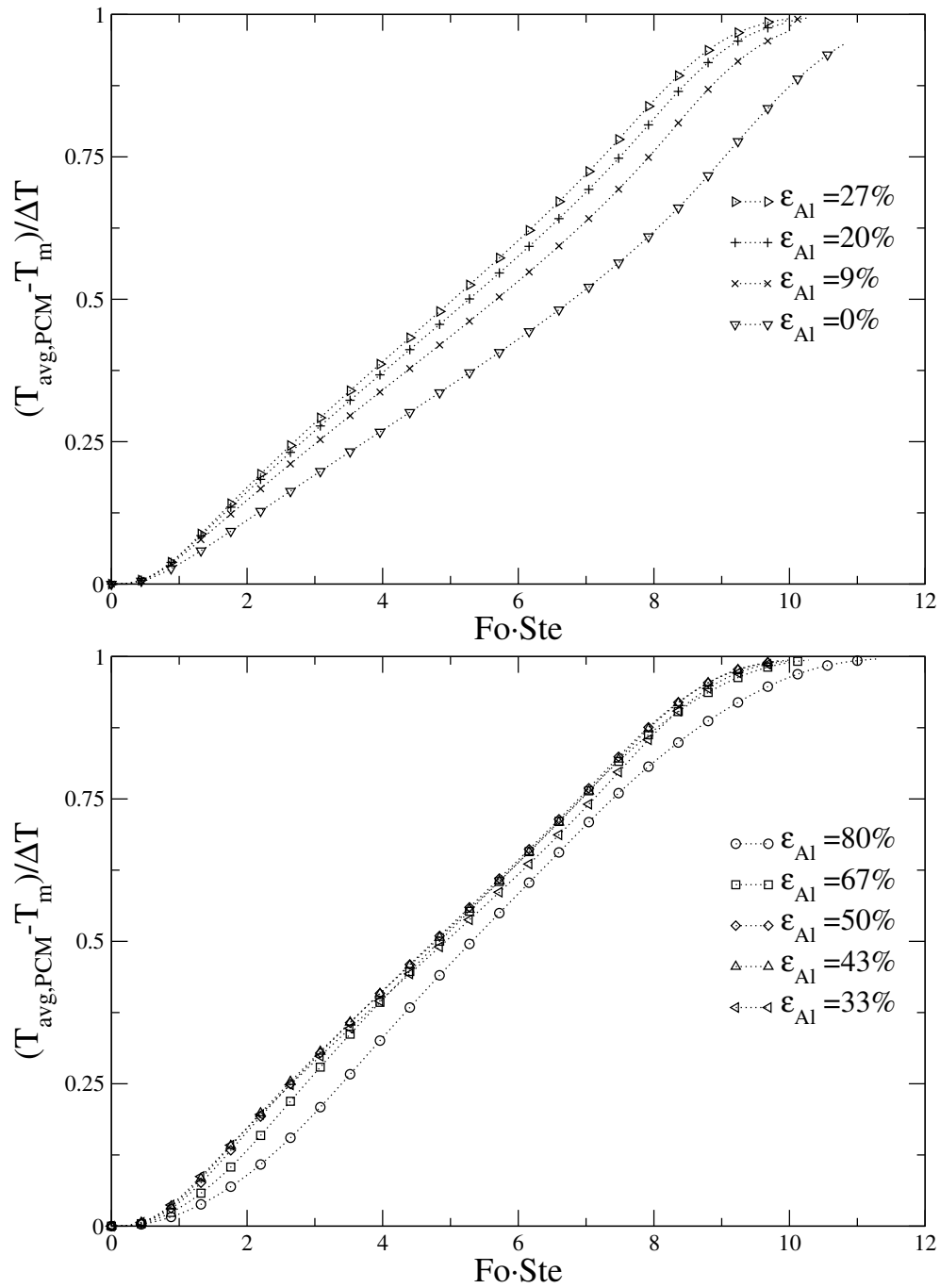


Figure 4.17: Average PCM particle temperature during charge for equal number of PCM particles and different volume fractions of Al particles

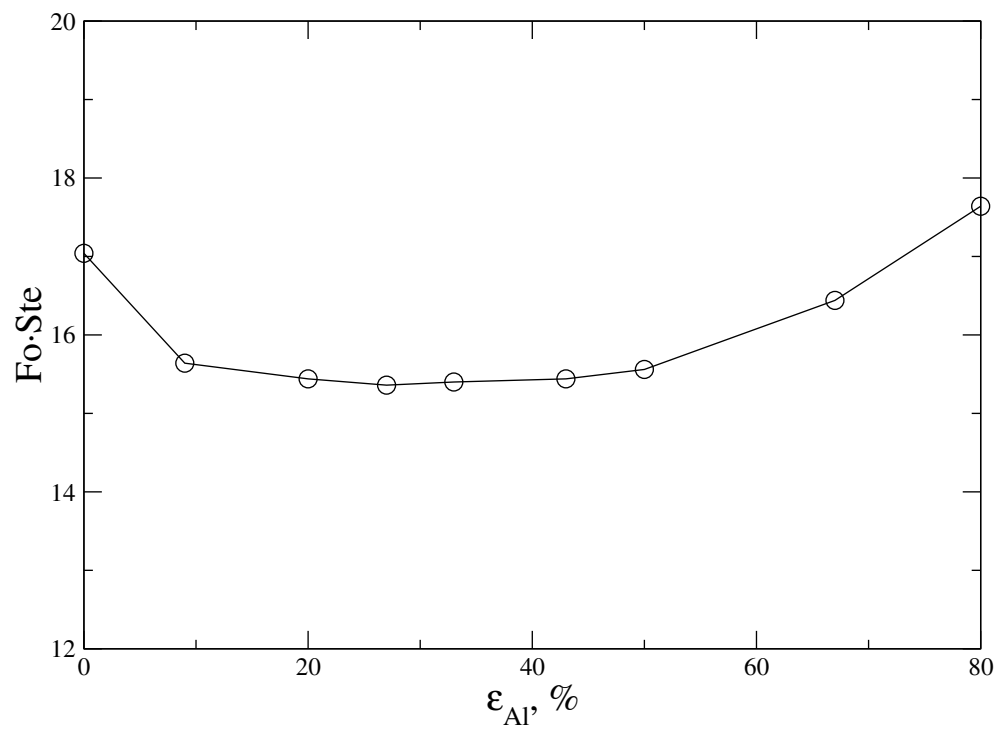


Figure 4.18: Time required for latent heat storage to reach saturation

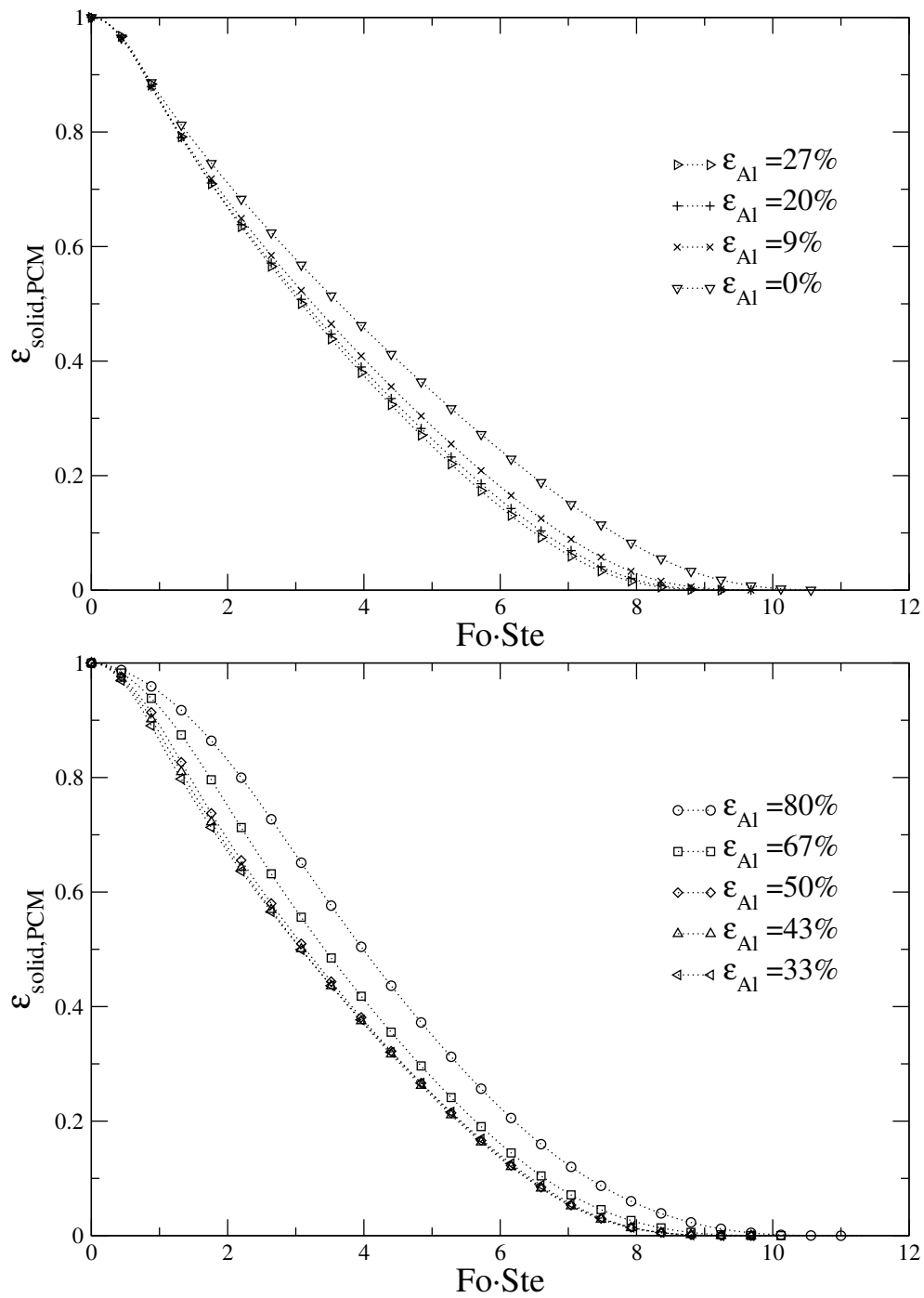


Figure 4.19: Average solid volume fraction during discharge for equal number of PCM and different volume fractions of Al particles

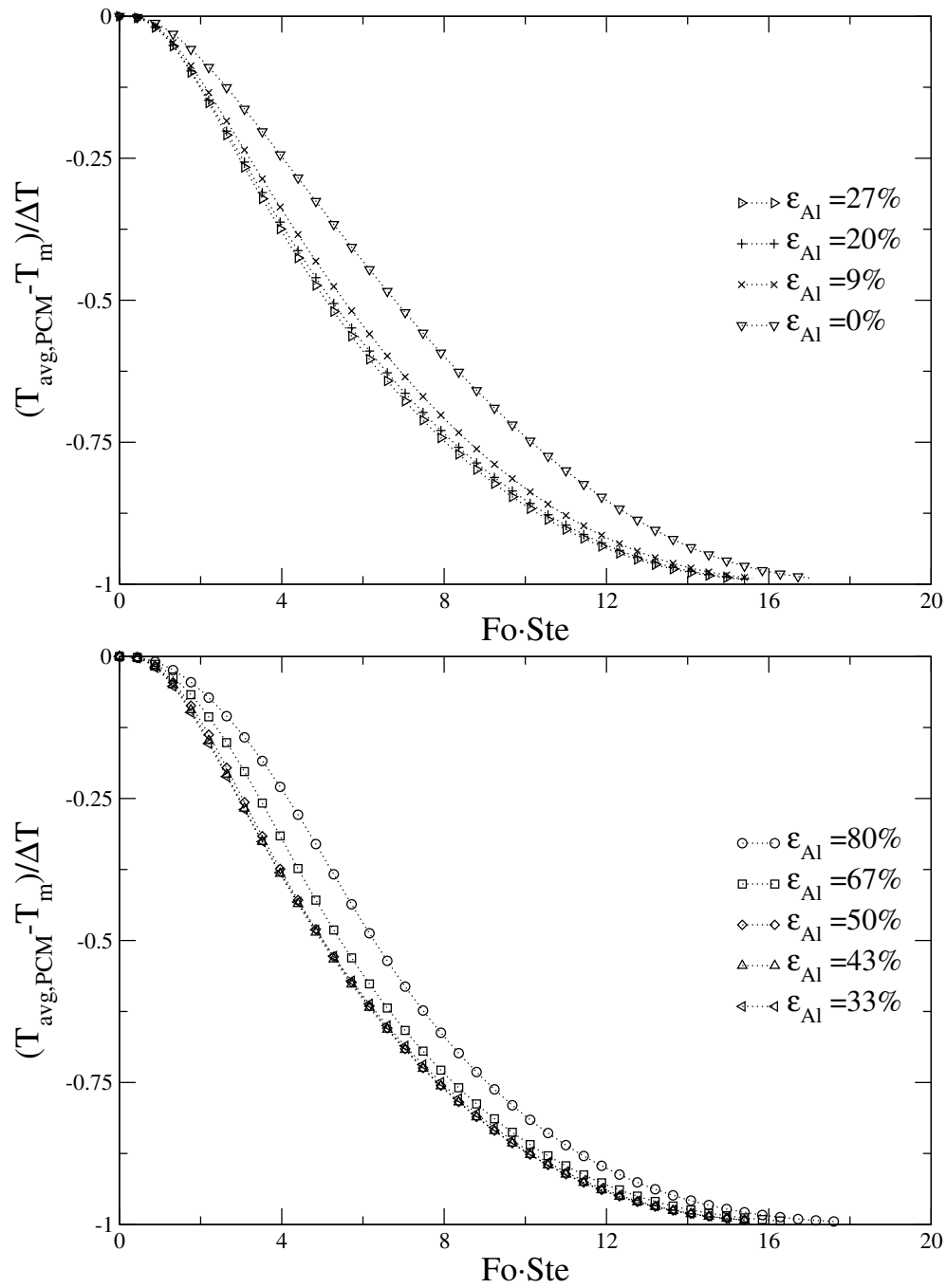


Figure 4.20: Average PCM particle temperature during discharge for equal number of PCM particles and different volume fractions of Al particles

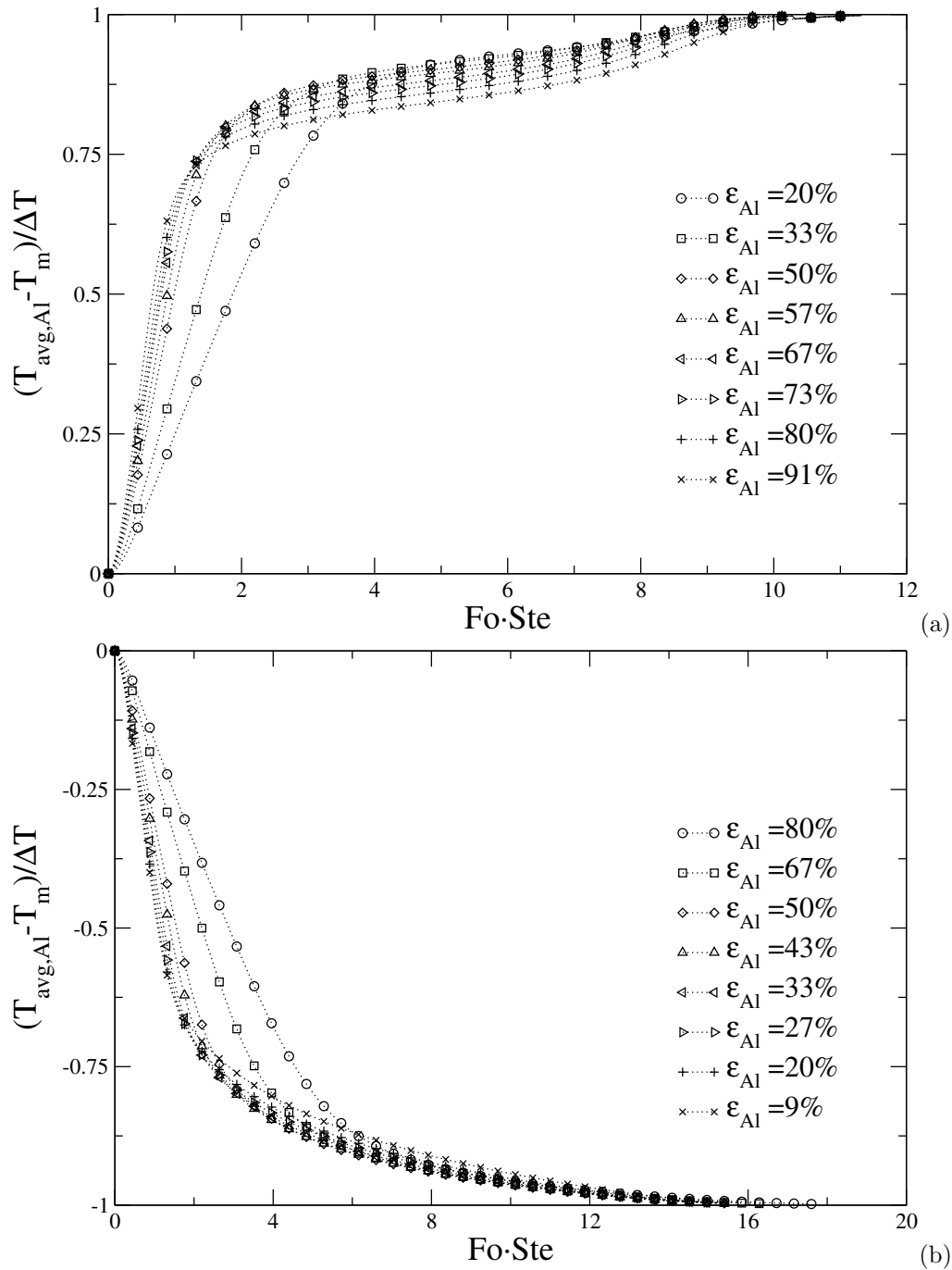


Figure 4.21: Average Al particle temperature during (a) charge and (b) discharge for equal number of PCM particles and different volume fractions of Al particles

Chapter 5

Conclusion

Discrete-element method (DEM) model is used to study fixed beds for electrical-to-chemical (E2C) energy storage and thermal energy storage (TES) applications in this work. For each application, submodels are developed and validated for individual particles in the fixed bed. The DEM model is useful for beds where interparticle interactions are significant, being whether momentum or energy.

For the E2C fixed-bed reactor, Joule heating was studied with gas flowing through an fixed-bed reactor for steam-methane reforming (SMR). The concept was designed in an attempt to address traditional SMR's thermal imbalance in the cross-section due to heat being supplied through radiant tubes. SMR reactors could incorporate more thermally advantageous designs if relatively uniform Joule heating could be supplied in the catalysts. 2D axisymmetric finite-volume-methods (FVM) simulations were conducted to find electrical and thermal resistance of particles. The results showed that the resistance between particles depended on the contact area, which were determined by contact mechanics. Simulations were conducted using a 3D DEM heat conduction model coupled with a 1D FVM convection model to study the thermal behaviour of the E2C reactor under non-reacting scenarios. The heating power of the reactor was limited by maximum temperature of the heating particles, which occurred at the contact spot between particles. In the FVM simulation, it was shown that the temperature difference between the contact spot and the centre of the particle was proportional to the amperage of the current passing through it. Therefore the maximum temperature of an operating reactor was calculated using this proportionality to validate the reactor. Not only were there conductive particles that provide Joule heating, but also were there non-conductive catalyst particles in the fixed bed to improve reaction rate. The more catalysts particles the fixed bed contained, the fewer current paths there were in the fixed bed. For catalyst particles that are 0.4 diameter of the conductive particles, the maximum valid volume fraction of catalyst is 0.30.

The TES concept used encapsulated phase change material(PCM) to storage excess heat from sunlight and other sources. The 1D submodel for intraparticle heat transfer with phase change was developed for the capsule and validated from published experimental results and CFD simulation. It was found that during melting free convection played an important role for heat transfer in the encapsulated phase-change material, but heat transfer during solidification is almost entirely dominated by conduction. A new idea was proposed to mix small metal particles in the fixed bed among PCM capsules to improve heat transfer and response time. The numerical verification using 3D interparticle DEM, 1D intraparticle FVM and 1D convection models showed that with aluminum particles in the fixed bed, the time needed for the melting/solidification to reach completion was seen to be decreased by up to 10% giving the same conditions. However, the aluminum particles also occupied additional space up to 20% so that the overall heat storage density for the TES is reduced.

5.1 Future Work

Based on results obtained in the studies, the following recommendations were made for the future work

- Implementation of SMR reaction kinetics into the model developed for E2C enables us to estimate the

maximum permissible current will be decided by reaction rates. As the endothermic reaction consumes thermal energy which changes the thermal profile in the fixed bed reactor. The maximum permissible current for which temperature remains under range will be decided by the reaction rate.

- The wall channeling effect on the heat transfer between particles and fluid close to the wall is to be taken in account, as it changes the flow pattern and heat transfer coefficient.
- The effect of the higher temperature at the contact points between conducting particles on particle-gas heat transfer needs to be validated.
- Intraparticle model may be implemented for E2C simulation for diffusion and temperature changes.
- Validate the heat transfer model developed for the heat storage fixed bed against experimental data published in the literature (large scale).

Bibliography

- [1] G. Mueller, "Radial void fraction distributions in randomly packed tied beds of uniformly sized spheres in cylindrical containers," *Powder Technology*, vol. 72, pp. 269–275, 1992.
- [2] F. Tan, "Constrained and unconstrained melting inside a sphere," *International Communications in Heat and Mass Transfer*, vol. 35, no. 4, pp. 466 – 475, 2008.
- [3] F. Tan, S. Hosseinizadeh, J. Khodadadi, and L. Fan, "Experimental and computational study of constrained melting of phase change materials (pcm) inside a spherical capsule," *International Journal of Heat and Mass Transfer*, vol. 52, no. 15–16, pp. 3464 – 3472, 2009.
- [4] W. J. Martin, R. J. and Ng, *The Thermal Regeneration of Exhausted Activated Carbon: The Balance Between Weight Loss and Regeneration Efficiency*, pp. 427–438. Boston, MA: Springer US, 1991.
- [5] A. Godula-Jopek, *Hydrogen production*. Weinheim: Wiley-VCH, 2015.
- [6] L. Yang and X. Ge, "Chapter three - biogas and syngas upgrading," 2016. ID: 315554.
- [7] S. D. Angeli, F. G. Pilitsis, and A. A. Lemonidou, "Methane steam reforming at low temperature: Effect of light alkanes' presence on coke formation," 2015. ID: 271364.
- [8] H. Storch and P. Golden, "Note on the preparation of pure methane from natural gas," *Journal of the American Chemical Society*, vol. 54, no. 12, pp. 4662–4663, 1932.
- [9] M. H. Halabi, M. H. J. M. de Croon, J. van der Schaaf, P. D. Cobden, and J. C. Schouten, "Low temperature catalytic methane steam reforming over ceria–zirconia supported rhodium," 2010. ID: 271346.
- [10] J. R. Hufton, S. Mayorga, and S. Sircar, "Sorptions-enhanced reaction process for hydrogen production," *American Institute of Chemical Engineers. AIChE Journal*, vol. 45, pp. 248–256, Feb 1, 1999.
- [11] S. Z. Abbas, V. Dupont, and T. Mahmud, "Modelling of h2 production in a packed bed reactor via sorption enhanced steam methane reforming process," 2017. ID: 271472.
- [12] C.-H. Li and B. Finlayson, "Heat transfer in packed beds—a reevaluation," *Chemical Engineering Science*, vol. 32, no. 9, pp. 1055–1066, 1977.
- [13] D. Vortmeyer and E. Haidegger, "Discrimination of three approaches to evaluate heat fluxes for wall-cooled fixed bed chemical reactors," *Chemical engineering science*, vol. 46, no. 10, pp. 2651–2660, 1991.
- [14] K. KAMIUTO, M. IWAMOTO, and Y. NAGUMO, "Combined conduction and correlated-radiation heat transfer in packedbeds," *Journal of Thermophysics and Heat Transfer*, vol. 7, no. 3, pp. 496–501, 1993.
- [15] C. K. Chan and C. L. Tien, "Conductance of packed spheres in vacuum," *Journal of Heat Transfer*, vol. 95, no. 3, p. 302, 1973.
- [16] S. Masamune and J. M. Smith, "Thermal conductivity of beds of spherical particles," *Industrial and Engineering Chemistry Fundamentals*, vol. 2, pp. 136–143, May 1, 1963.
- [17] M. Bahrami, M. M. Yovanovich, and J. R. Culham, "Effective thermal conductivity of rough spherical packed beds," *International Journal of Heat and Mass Transfer*, vol. 49, no. 19, pp. 3691–3701, 2006.
- [18] F. Benyahia and K. E. O'Neill, "Enhanced voidage correlations for packed beds of various particle shapes and sizes," *Particulate Science and Technology*, vol. 23, pp. 169–177, Apr 1, 2005.

- [19] K. Liu, *Hydrogen and syngas production and purification technologies*. Hoboken, NJ: Wiley, 2010.
- [20] O. Martinez, S. P. Duarte, and N. Lemcoff, "Modeling of fixed bed catalytic reactors," *Computers and Chemical Engineering*, vol. 9, no. 5, pp. 535 – 545, 1985. Papers from the 25th CONICET International Conference.
- [21] N. Mariani, O. Martínez, and G. Barreto, "Evaluation of heat transfer parameters in packed beds with cocurrent downflow of liquid and gas," *Chemical Engineering Science*, vol. 56, no. 21-22, pp. 5995–6001, 2001. cited By 21.
- [22] M. Taulamet, N. Mariani, O. Martínez, and G. Barreto, "Prediction of effective reaction rates in catalytic systems of multiple reactions using one-dimensional models," *Chemical Engineering Journal*, vol. 335, pp. 876–886, 2018. cited By 0.
- [23] Y. Kutsovsky, L. Scriven, H. Davis, and B. Hammer, "NMR imaging of velocity profiles and velocity distributions in bead packs," *Physics of Fluids*, vol. 8, pp. 863–871, 1996.
- [24] T. Eppinger, K. Seidler, and M. Kraume, "Dem-cfd simulations of fixed bed reactors with small tube to particle diameter ratios," *Chemical Engineering Journal*, vol. 166, no. 1, pp. 324 – 331, 2011.
- [25] A. I. Anastasov, "A study of the influence of the operating parameters on the temperature of the hot spot in a fixed bed reactor," *Chemical Engineering Journal*, vol. 86, no. 3, pp. 287 – 297, 2002.
- [26] S. A. Logtenberg and A. G. Dixon, "Computational fluid dynamics studies of fixed bed heat transfer," *Chemical Engineering and Processing: Process Intensification*, vol. 37, no. 1, pp. 7–21, 1998.
- [27] S. A. Logtenberg and A. G. Dixon, "Computational fluid dynamics studies of the effects of temperature-dependent physical properties on fixed-bed heat transfer," *Industrial & engineering chemistry research*, vol. 37, no. 3, pp. 739–747, 1998.
- [28] S. Logtenberg, M. Nijemeisland, and A. Dixon, "Computational fluid dynamics simulations of fluid flow and heat transfer at the wall–particle contact points in a fixed-bed reactor," *Chemical Engineering Science*, vol. 54, no. 13, pp. 2433–2439, 1999.
- [29] A. G. Dixon, M. E. Taskin, E. H. Stitt, and M. Nijemeisland, "3d cfd simulations of steam reforming with resolved intraparticle reaction and gradients," *Chemical Engineering Science*, vol. 62, no. 18, pp. 4963 – 4966, 2007. 19th International Symposium on Chemical Reaction Engineering - From Science to Innovative Engineering.
- [30] M. E. Taskin, A. G. Dixon, and E. H. Stitt, "CFD study of fluid flow and heat transfer in a fixed bed of cylinders," *Numerical Heat Transfer, Part A: Applications*, vol. 52, no. 3, pp. 203–218, 2007.
- [31] A. G. Dixon, M. E. Taskin, M. Nijemeisland, and E. H. Stitt, "Wall-to-particle heat transfer in steam reformer tubes: Cfd comparison of catalyst particles," *Chemical Engineering Science*, vol. 63, no. 8, pp. 2219 – 2224, 2008.
- [32] A. G. Dixon, M. E. Taskin, M. Nijemeisland, and E. H. Stitt, "Systematic mesh development for 3d cfd simulation of fixed beds: Single sphere study," *Computers & Chemical Engineering*, vol. 35, no. 7, pp. 1171 – 1185, 2011.
- [33] M. Behnam, A. G. Dixon, P. M. Wright, M. Nijemeisland, and E. H. Stitt, "Comparison of cfd simulations to experiment under methane steam reforming reacting conditions," *Chemical Engineering Journal*, vol. 207-208, pp. 690 – 700, 2012. 22nd International Symposium on Chemical Reaction Engineering (ISCRE 22).
- [34] Z. Mansoori, M. Saffar-Avval, H. B. Tabrizi, B. Dabir, and G. Ahmadi, "Inter-particle heat transfer in a riser of gas–solid turbulent flows," *Powder Technology*, vol. 159, no. 1, pp. 35 – 45, 2005.
- [35] A. G. Dixon, "Local transport and reaction rates in a fixed bed reactor tube: Endothermic steam methane reforming," *Chemical Engineering Science*, vol. 168, pp. 156 – 177, 2017.
- [36] S. Hermansson and H. Thunman, "Cfd modelling of bed shrinkage and channelling in fixed-bed combustion," 2011. ID: 271463.
- [37] M. Zhang, H. Dong, and Z. Geng, "Computational study of flow and heat transfer in fixed beds with cylindrical particles for low tube to particle diameter ratios," 2018. ID: 276837.
- [38] H. Zhu, Z. Zhou, R. Yang, and A. Yu, "Discrete particle simulation of particulate systems: Theoretical developments," *Chemical Engineering Science*, vol. 62, no. 13, pp. 3378 – 3396, 2007. Frontier of Chemical Engineering - Multi-scale Bridge between Reductionism and Holism.

- [39] H. Zhu, Z. Zhou, R. Yang, and A. Yu, "Discrete particle simulation of particulate systems: A review of major applications and findings," *Chemical Engineering Science*, vol. 63, no. 23, pp. 5728 – 5770, 2008.
- [40] J. Theuerkauf, P. Witt, and D. Schwesig, "Analysis of particle porosity distribution in fixed beds using the discrete element method," *Powder Technology*, vol. 165, no. 2, pp. 92 – 99, 2006.
- [41] R. Caulkin, W. Tian, M. Pasha, A. Hassanpour, and X. Jia, "Impact of shape representation schemes used in discrete element modelling of particle packing," *Computers & Chemical Engineering*, vol. 76, pp. 160 – 169, 2015.
- [42] H. Tangri, Y. Guo, and J. S. Curtis, "Packing of cylindrical particles: Dem simulations and experimental measurements," *Powder Technology*, vol. 317, pp. 72 – 82, 2017.
- [43] N. Jurtz, M. Kraume, and G. Wehinger, "Advances in fixed-bed reactor modeling using particle-resolved computational fluid dynamics (CFD)," *Reviews in Chemical Engineering*, p. in press, 2018.
- [44] H.-S. Roh, D. K. Lee, K. Y. Koo, U. H. Jung, and W. L. Yoon, "Natural gas steam reforming for hydrogen production over metal monolith catalyst with efficient heat-transfer," *International Journal of Hydrogen Energy*, vol. 35, no. 4, pp. 1613 – 1619, 2010.
- [45] H.-S. Roh, K. Y. Koo, U. H. Jung, and W. L. Yoon, "Hydrogen production from natural gas steam reforming over ni catalysts supported on metal substrates," *Current Applied Physics*, vol. 10, no. 2, pp. S37 – S39, 2010.
- [46] J.-H. Ryu, K.-Y. Lee, H. La, H.-J. Kim, J.-I. Yang, and H. Jung, "Ni catalyst wash-coated on metal monolith with enhanced heat-transfer capability for steam reforming," *Journal of Power Sources*, vol. 171, no. 2, pp. 499 – 505, 2007.
- [47] S. Khajeh, Z. A. Aboosadi, and B. Honarvar, "A comparative study between operability of fluidized-bed and fixed-bed reactors to produce synthesis gas through tri-reforming," *Journal of Natural Gas Science and Engineering*, vol. 19, pp. 152 – 160, 2014.
- [48] M. B. Glaser and G. Thodos, "Heat and momentum transfer in the flow of gases through packed beds," *AIChE Journal*, vol. 4, no. 1, pp. 63–68, 1958.
- [49] S. Schulze, P. A. Nikrityuk, and B. Meyer, "Porosity Distribution in Monodisperse and Polydisperse Fixed beds and Its Impact on the Fluid Flow," *Particulate Science and Technology*, 2014.
- [50] F. V. D. J. KOZICKI, "Yade-open DEM: an open-source software using a discrete element method to simulate granular material," *Engineering Computations*, vol. 26, no. 7, pp. 786–805, 2009.
- [51] J. A. Greenwood, "Constriction resistance and the real area of contact," *British Journal of Applied Physics*, vol. 17, no. 12, p. 1621, 1966.
- [52] P. G. Slade, *Electrical Contacts: Principles and Applications*. CRC Press, 1999.
- [53] N. Ray, B. Kempf, T. Mützel, L. Froyen, K. Vanmeensel, and J. Vleugels, "Effect of {wc} particle size and ag volume fraction on electrical contact resistance and thermal conductivity of agâwc contact materials," *Materials & Design*, vol. 85, pp. 412 – 422, 2015.
- [54] A. E. Barrington, "The fusing of wires with heavy surge currents," *British Journal of Applied Physics*, vol. 7, no. 11, p. 408, 1956.
- [55] D. J. Gunn, "Transfer of Heat or Mass to Particles in Fixed and Fluidized Beds," *International Journal of Heat and Mass Transfer*, vol. 21, no. 467–476, 1978.
- [56] I. ANSYS, "ANSYS-FLUENT™ V16.2 – Commercially available CFD software package based on the Finite Volume method. Southpointe, 275 Technology Drive, Canonsburg, PA 15317, U.S.A., www.ansys.com," 2016.
- [57] Václav Smilauer., "Yade - Open Source Discrete Element Method." <https://yade-dem.org/doc/>, 2009.
- [58] T. Eppinger, G. Wehinger, and M. Kraume, "Parameter optimization for the oxidative coupling of methane in a fixed bed reactor by combination of response surface methodology and computational fluid dynamics," *Chem. Eng. Res. Des.*, vol. 92, pp. 1693–1703, 2014.
- [59] O. Ajuwon, "Experimental and numerical study of particles heating using DC discharge," Master's thesis, University of Alberta, Edmonton, AB, Canada, 2015.

- [60] V. A. A. Raj and R. Velraj, "Review on free cooling of buildings using phase change materials," 2010. ID: 271969.
- [61] C. Arkar and S. Medved, "Free cooling of a building using pcm heat storage integrated into the ventilation system," 2007. ID: 271459.
- [62] M. A. Izquierdo-Barrientos, C. Sobrino, and J. A. Almendros-Ibáñez, "Energy storage with pcm in fluidized beds: Modeling and experiments," 2015. ID: 271942.
- [63] H. Peng, H. Dong, and X. Ling, "Thermal investigation of pcm-based high temperature thermal energy storage in packed bed," 2014. ID: 271098.
- [64] S. Bellan, T. E. Alam, J. González-Aguilar, M. Romero, M. M. Rahman, D. Y. Goswami, and E. K. Stefanakos, "Numerical and experimental studies on heat transfer characteristics of thermal energy storage system packed with molten salt pcm capsules," 2015. ID: 271641.
- [65] Q. Yu, A. Romagnoli, B. Al-Duri, D. Xie, Y. Ding, and Y. Li, "Heat storage performance analysis and parameter design for encapsulated phase change materials," 2018. ID: 271098.
- [66] J. J. Blaney, S. Neti, W. Z. Misiolek, and A. Oztekin, "Containment capsule stresses for encapsulated phase change materials," 2013. ID: 271641.
- [67] J. M. Mahdi and E. C. Nsofor, "Solidification enhancement of pcm in a triplex-tube thermal energy storage system with nanoparticles and fins," 2018. ID: 271429.
- [68] A. A. R. Darzi, M. Jourabian, and M. Farhadi, "Melting and solidification of pcm enhanced by radial conductive fins and nanoparticles in cylindrical annulus," 2016. ID: 271098.
- [69] S. Takeda, K. Nagano, T. Mochida, and K. Shimakura, "Development of a ventilation system utilizing thermal energy storage for granules containing phase change material," 2004. ID: 271459.
- [70] S. Ergun, "Fluid flow through packed columns," *Fluid Flow Through Packed Columns*, pp. 89–94, 1952. Cited By :11.
- [71] N. Standish and J. B. Drinkwater, "The effect of particle shape on flooding rates in packed columns," 1970. ID: 271348.
- [72] P. Chandra and D. H. Willits, "Pressure drop and heat transfer characteristics of air-rockbed thermal storage systems," 1981. ID: 271459.
- [73] H. Singh, R. P. Saini, and J. S. Saini, "Performance of a packed bed solar energy storage system having large sized elements with low void fraction," 2013. ID: 271459.
- [74] R. L. Webb, *Toward a common understanding of the performance and selection of roughness for forced convection*, pp. 257–272. Washington, Hemisphere Publishing Corp.; New York, McGraw-Hill Book Co., 1979.
- [75] P. B. Grimado and B. A. Boley, "A numerical solution for the symmetric melting of spheres," *International Journal for Numerical Methods in Engineering*, vol. 2, no. 2, pp. 175–188, 1970.
- [76] S. Paterson, "On certain types of solution of the equation of heat conduction," *Proceedings of the Glasgow Mathematical Association*, vol. 1, pp. 48–52, 001 1952.
- [77] K. A. R. Ismail and J. R. Henriquez, "Solidification of pcm inside a spherical capsule," 2000. ID: 271098.
- [78] K. A. R. Ismail and J. R. Henriquez, "Numerical and experimental study of spherical capsules packed bed latent heat storage system," 2002. ID: 271641.
- [79] N. L. Narasimhan, V. Veeraraghavan, G. Ramanathan, B. S. Bharadwaj, and M. Thamilmani, "Studies on the inward spherical solidification of a phase change material dispersed with macro particles," 2018. ID: 308665.
- [80] N. L. Narasimhan, R. Bharath, S. A. Ramji, M. Tarun, and A. S. Arumugam, "Numerical studies on the performance enhancement of an encapsulated thermal storage unit," 2014. ID: 272088.
- [81] J. Yang and C. Y. Zhao, "Solidification analysis of a single particle with encapsulated phase change materials," 2013. ID: 271641.

- [82] S. Bellan, J. Gonzalez-Aguilar, M. Romero, M. M. Rahman, D. Y. Goswami, and E. K. Stefanakos, “Numerical investigation of pcm-based thermal energy storage system,” 2015. ID: 277910.
- [83] F. E. Moore and Y. Bayazitoglu, “Melting within a spherical enclosure,” *Journal of Heat Transfer*, vol. 104, no. 1, pp. 19–23, 1982. Cited By :81.
- [84] J. Khodadadi and Y. Zhang, “Effects of buoyancy-driven convection on melting within spherical containers,” *International Journal of Heat and Mass Transfer*, vol. 44, no. 8, pp. 1605 – 1618, 2001.
- [85] M. Rizan, F. Tan, and C. Tso, “An experimental study of n-octadecane melting inside a sphere subjected to constant heat rate at surface,” *International Communications in Heat and Mass Transfer*, vol. 39, no. 10, pp. 1624 – 1630, 2012.
- [86] S. Hosseinizadeh, A. R. Darzi, F. Tan, and J. Khodadadi, “Unconstrained melting inside a sphere,” *International Journal of Thermal Sciences*, vol. 63, pp. 55 – 64, 2013.
- [87] F. Inc., *Fluent Manual*, 2001.
- [88] H. Bansal, S. Ghaemi, and P. Nikrityuk, “A scale-bridging model for ice particles melting in air,” 2017. ID: 271348.
- [89] D. O. Akinyele and R. K. Rayudu, “Review of energy storage technologies for sustainable power networks,” 2014. ID: 282793.
- [90] T. Esence, A. Bruch, S. Molina, B. Stutz, and J.-F. Fourmigué, “A review on experience feedback and numerical modeling of packed-bed thermal energy storage systems,” 2017. ID: 271459.
- [91] K. S. Reddy, V. Mudgal, and T. K. Mallick, “Review of latent heat thermal energy storage for improved material stability and effective load management,” 2018. ID: 308665.
- [92] A. Abhat, “Low temperature latent heat thermal energy storage: Heat storage materials,” 1983. ID: 271459.
- [93] M. A. Izquierdo-Barrientos, M. Fernández-Torrijos, J. A. Almendros-Ibáñez, and C. Sobrino, “Experimental study of fixed and fluidized beds of pcm with an internal heat exchanger,” 2016. ID: 271641.
- [94] B. Xu, P. Li, and C. Chan, “Application of phase change materials for thermal energy storage in concentrated solar thermal power plants: A review to recent developments,” 2015. ID: 271429.
- [95] M. M. Farid, A. M. Khudhair, S. A. K. Razack, and S. Al-Hallaj, “A review on phase change energy storage: materials and applications,” 2004. ID: 271098.
- [96] S. Álvarez, L. F. Cabeza, A. Ruiz-Pardo, A. Castell, and J. A. Tenorio, “Building integration of pcm for natural cooling of buildings,” 2013. ID: 271429.
- [97] P. Stark, “Pcm-impregnated polymer microcomposites for thermal energy storage,” 1990. JO:; JF:.
- [98] L. Royon, G. Guiffant, and P. Flaud, “Investigation of heat transfer in a polymeric phase change material for low level heat storage,” 1997. ID: 271098.
- [99] M. Rady, “Granular phase change materials for thermal energy storage: Experiments and numerical simulations,” 2009. ID: 271641.
- [100] S. Bazri, I. A. Badruddin, M. S. Naghavi, and M. Bahiraei, “A review of numerical studies on solar collectors integrated with latent heat storage systems employing fins or nanoparticles,” 2018. ID: 271431.
- [101] T. Schumann, “Heat transfer: A liquid flowing through a porous prism,” *Journal of the Franklin Institute*, vol. 208, no. 3, pp. 405–416, 1929.
- [102] D. Handley and P. J. Heggs, “The effect of thermal conductivity of the packing material on transient heat transfer in a fixed bed,” 1969. ID: 271451.
- [103] T. Hu, A. H. Hassabou, M. Spinnler, and W. Polifke, “Performance analysis and optimization of direct contact condensation in a pcm fixed bed regenerator,” 2011. ID: 271370.
- [104] E. Oró, J. Chiu, V. Martin, and L. F. Cabeza, “Comparative study of different numerical models of packed bed thermal energy storage systems,” 2013. ID: 271641.

- [105] S. Karthikeyan, G. R. Solomon, V. Kumaresan, and R. Velraj, "Parametric studies on packed bed storage unit filled with pcm encapsulated spherical containers for low temperature solar air heating applications," 2014. ID: 271098.
- [106] S. Wu, G. Fang, and X. Liu, "Dynamic discharging characteristics simulation on solar heat storage system with spherical capsules using paraffin as heat storage material," 2011. ID: 271431.
- [107] A. E. Saez and B. J. McCoy, "Dynamic response of a packed bed thermal storage system—a model for solar air heating," 1982. ID: 271459.